

Overflow metabolism originates from growth optimization and cell heterogeneity

Xin Wang^{1*}

¹School of Physics, Sun Yat-sen University, Guangzhou 510275, China

*For correspondence: wangxin36@mail.sysu.edu.cn

Abstract

A classic problem in metabolism is that fast-proliferating cells use seemingly wasteful fermentation to generate energy in the presence of sufficient oxygen. This counterintuitive phenomenon, known as overflow metabolism, or the Warburg effect in cancer, is universal across various organisms. Despite extensive research, its origin and function remain unclear. Here, we take *Escherichia coli* as a typical example and show that overflow metabolism can be understood through growth optimization combined with cell heterogeneity. A model of optimal protein allocation, coupled with heterogeneity in enzyme catalytic rates among cells, quantitatively explains why and how cells make the choice between respiration and fermentation under different nutrient conditions. Our model quantitatively illustrates the growth rate dependence of fermentation flux and enzyme allocation under various perturbations, which is fully validated by experimental results. Our work solves the long-standing puzzle of overflow metabolism and can be broadly used to address heterogeneity-related challenges in metabolism.

Introduction

A prominent feature of cancer metabolism is that tumor cells excrete large quantities of fermentation products in the presence of sufficient oxygen (Hanahan and Weinberg, 2011; Liberti and Locasale, 2016; Vander Heiden et al., 2009). This process, discovered by Otto Warburg in the 1920s (Warburg et al., 1924) and known as the Warburg effect, aerobic glycolysis or overflow metabolism (Basan et al., 2015; Hanahan and Weinberg, 2011; Liberti and Locasale, 2016; Vander Heiden et al., 2009), is ubiquitous for fast-proliferating cells across a broad spectrum of organisms (Vander Heiden et al., 2009), ranging from bacteria (Basan et al., 2015; Holms, 1996; Meyer et al., 1984; Nanchen et al., 2006; Neidhardt et al., 1990) and fungi (De Deken, 1966) to mammalian cells (Hanahan and Weinberg, 2011; Liberti and Locasale, 2016; Vander Heiden et al., 2009). For microbes, cells use standard respiration when nutrients are scarce, while they use the counterintuitive aerobic glycolysis when nutrients are adequate, just analogous to normal tissues and cancer cells, respectively (Vander Heiden et al., 2009). Over the past century, especially with extensive studies in the last two decades (Liberti and Locasale, 2016), various rationales for overflow metabolism have been proposed (Basan et al., 2015; Chen and Nielsen, 2019; Majewski and Domach, 1990; Molenaar et al., 2009; Niebel et al., 2019; Pfeiffer et al., 2001; Shlomi et al., 2011; Vander Heiden et al., 2009; Varma and Palsson, 1994; Vazquez et al., 2010; Vazquez and Oltvai, 2016). In particular, Basan *et al.* (Basan et al., 2015) provided a systematic characterization of this process, including various types of perturbations in experiments. However, the origin and function of overflow metabolism still remain unclear (DeBerardinis and Chandel, 2020; Hanahan and Weinberg, 2011; Liberti and Locasale, 2016; Vander Heiden et al., 2009).

Why have microbes and cancer cells evolved to possess the seemingly wasteful aerobic glycolysis strategy? For unicellular organisms, there is evolutionary pressure (Vander Heiden et al., 2009) to optimize cellular resources for rapid growth (Dekel and Alon, 2005; Edwards et al., 2001; Hui et al., 2015; Li et al., 2018; Scott et al., 2010; Towbin et al., 2017; Wang et al., 2019; You et al., 2013). In particular, it has been shown that cells allocate protein resources for optimal growth (Hui et al., 2015; Scott et al., 2010; Wang et al., 2019; You et al., 2013), and the most efficient protein allocation corresponds to elementary flux mode (Müller et al., 2014; Wortel et al., 2014). In this study, we extend these approaches in a heterogeneous framework to address the puzzle of aerobic glycolysis. We use *Escherichia coli* as a typical example and show that overflow metabolism can be understood from optimal protein allocation combined with the heterogeneity in enzyme catalytic rates. The optimal growth strategy varies between respiration and fermentation depending on the concentration and type of the nutrient, and the combination with cell heterogeneity results in the standard picture (Basan et al., 2015; Holms, 1996; Meyer et al., 1984; Nanchen et al., 2006) of overflow metabolism. Our model quantitatively illustrates the growth rate dependence of fermentation/respiration flux and enzyme allocation under various types of perturbations, and can be used to explain the Warburg effect in tumor cells.

Results

Coarse-grained model

Based on the topology of the metabolic network (Neidhardt et al., 1990; Nelson et al., 2008) (Fig. 1A), we classify the carbon sources that enter from the upper part of glycolysis into Group A (Wang et al., 2019), and the precursors of biomass components (such as amino acids) into five pools (see Appendix 1.2 for details): a1 (entry point: G6P/F6P), a2 (entry point: GA3P/3PG/PEP), b (entry point: pyruvate/acetyl-CoA), c (entry point: α -ketoglutarate), and d (entry point: oxaloacetate). Pools a1 and a2 are also combined as Pool a due to joint synthesis of precursors. Then, the metabolic network for Group A carbon source utilization (Fig. 1A) is coarse-grained into a model shown in Fig. 1B (see Appendix 2.1 for details), where node A represents an arbitrary carbon source of Group A. Evidently, Fig. 1B is topologically identical to Fig. 1A. Each coarse-grained arrow in Fig. 1B carries a stoichiometric flux J_i , which delivers carbon flux and may consume or produce energy (e.g., J_1 , J_{a1} , see Figs. 1A-B and Appendix-fig. 1A).

In fact, the stoichiometric flux J_i scales with the cell population. For comparison with experiments, we define the normalized flux $J_i^{(N)} \equiv J_i \cdot m_0 / M_{\text{carbon}}$, which can be regarded as the flux per unit of biomass (the superscript “(N)” stands for normalized; see Appendix 1.3-1.4 for details). Here, M_{carbon} represents the carbon mass of the cell population, and m_0 is the weighted average carbon mass of metabolite molecules at the entrance of precursor pools (see Eq. S17).

Then, the cell growth rate λ can be represented by $\lambda = \sum_i^{a1,a2,b,c,d} J_i^{(N)}$ (see Appendix 1.4), and the normalized fluxes of respiration and fermentation are $J_r^{(N)} \equiv J_4^{(N)}$ and $J_f^{(N)} \equiv J_6^{(N)}$, respectively. In practice, each $J_i^{(N)}$ is characterized by two quantities: the proteomic mass fraction ϕ_i of the enzyme dedicated to carrying the flux and the substrate quality κ_i , such that $J_i^{(N)} = \phi_i \cdot \kappa_i$. We take the Michaelis-Menten form for the enzyme kinetics, and then $\kappa_i \equiv k_i \cdot \frac{[S_i]}{[S_i] + K_i}$ (see Eq. S12 and Appendix 1.4 for details), where $[S_i]$ is the concentration of substrate S_i . For each intermediate node and reaction along the pathway (e.g., node M_1 in J_{a1}), the substrate quality κ_i can be approximated as a constant (see Appendix 1.5): $\kappa_i \equiv k_i \cdot \frac{[S_i]}{[S_i] + K_i} \approx k_i$, where $[S_i] \geq K_i$ generally holds true in bacteria (Bennett et al., 2009; Park et al., 2016). However, κ_A is a variable that depends on the concentration and nutrient type of a Group A carbon source (see Eq. S27).

Generally, there are three distinct destinies of a Group A carbon source in the metabolic network (Appendix-fig. 1C-E): fermentation, respiration, and biomass generation. Each draws a proteome fraction of ϕ_f , ϕ_r and ϕ_{BM} . The net effect of the first two destinies is energy production, while the last one generates precursors of biomass accompanied by energy production. By applying the

proteomic constraint (Scott et al., 2010) that there is a maximum fraction ϕ_{\max} for proteome allocation ($\phi_{\max} \approx 0.48$ (Scott et al., 2010)), we have:

$$\phi_f + \phi_r + \phi_{\text{BM}} = \phi_{\max}. \quad (1)$$

In fact, Eq. 1 is equivalent to $\phi_R + \phi_A + \sum_{j=1}^6 \phi_j + \sum_i^{a1,a2,b,c,d} \phi_i = \phi_{\max}$ (see Appendix 2.1), where ϕ_R stands for the mass fraction of the active ribosome-affiliated proteins. In cell proliferation, ribosomes constitute the majority of enzymes for protein synthesis (Neidhardt et al., 1990; Nelson et al., 2008), while other biomass components such as RNA are optimally produced (Kostinski and Reuveni, 2020) following the growth rate set by protein synthesis. Thus, $\lambda = \phi_R \cdot \kappa_t$, where κ_t is a parameter determined by the translation rate (Scott et al., 2010) (see Appendix 1.1 for details), which can be approximated as a constant in the growth rate range of concern (Dai et al., 2016).

For balanced cell growth, the energy demand is generally proportional to the biomass production rate. Thus, the normalized energy production rate $J_E^{(N)}$ is proportional to the growth rate λ (see Appendix 2.1 for details):

$$J_E^{(N)} = \eta_E \cdot \lambda, \quad (2)$$

where η_E is the energy coefficient. By converting all the energy currencies into ATPs, the normalized energy fluxes of respiration and fermentation are $J_r^{(E)} = \beta_r^{(A)} \cdot J_r^{(N)} / 2$ and $J_f^{(E)} = \beta_f^{(A)} \cdot J_f^{(N)} / 2$, where $\beta_r^{(A)}$ and $\beta_f^{(A)}$ are the stoichiometric coefficients of ATP production per glucose in each pathway (see Appendix-fig. 1C-E and Appendix 2.1 for details). The denominator coefficient (“2”) is derived from the stoichiometry of the coarse-grained reaction $M_1 \rightarrow 2M_2$ (see Fig. 1A-B). Using flux balance analysis at each intermediate node ($M_i, i = 1, \dots, 5$) and precursor pool (Pool $i, i = a1, a2, b, c, d$), combined with the constraints of proteome allocation (Eq. 1) and energy demand (Eq. 2), we obtain the relations between energy fluxes and growth rate for a given nutrient condition with fixed κ_A (see Appendix 2.1 for details):

$$\begin{cases} J_r^{(E)} + J_f^{(E)} = \varphi \cdot \lambda, \\ \frac{J_r^{(E)}}{\varepsilon_r} + \frac{J_f^{(E)}}{\varepsilon_f} = \phi_{\max} - \psi \cdot \lambda, \end{cases} \quad (3)$$

where φ is a constant coefficient mainly determined by η_E (see Eq. S33), and $\varphi \cdot \lambda$ represents the normalized energy demand other than the biomass pathway. The coefficients ψ , ε_r and ε_f are all functions of κ_A . ψ^{-1} is the proteome efficiency of the biomass pathway (see Eq. S32), with

$\psi^{-1} \equiv \lambda / \phi_{\text{BM}} \cdot \varepsilon_r$ and ε_f are the proteome energy efficiencies of the respiration and fermentation pathways, with $\varepsilon_r \equiv J_r^{(\text{E})} / \phi_r$ and $\varepsilon_f \equiv J_f^{(\text{E})} / \phi_f$:

$$\begin{cases} \varepsilon_r = \frac{\beta_r^{(A)}}{1/\kappa_A + 1/\kappa_r^{(A)}}, \\ \varepsilon_f = \frac{\beta_f^{(A)}}{1/\kappa_A + 1/\kappa_f^{(A)}}, \end{cases} \quad (4)$$

where both $\kappa_r^{(A)}$ and $\kappa_f^{(A)}$ are constants, with $1/\kappa_r^{(A)} \equiv 1/\kappa_1 + 2/\kappa_2 + 2/\kappa_3 + 2/\kappa_4$ and $1/\kappa_f^{(A)} \equiv 1/\kappa_1 + 2/\kappa_2 + 2/\kappa_6$ (see Appendix 2.1 for details).

Origin of overflow metabolism

The standard picture of overflow metabolism (Basan et al., 2015; Holms, 1996; Meyer et al., 1984; Nanchen et al., 2006) is exemplified by the experimental data (Basan et al., 2015) shown in Fig. 1C: the fermentation flux exhibits a threshold-analog dependence on the growth rate λ . It is well known that respiration is far more efficient than fermentation in terms of energy production per unit carbon (i.e., $\beta_r^{(A)} > \beta_f^{(A)}$) (Nelson et al., 2008; Vander Heiden et al., 2009). Then, why do cells bother to use the seemingly wasteful fermentation pathway? We proceed to resolve these issues using the optimal protein allocation hypothesis (Scott et al., 2010; You et al., 2013).

For cell proliferation in a given nutrient with fixed κ_A , the values of ε_r , ε_f and ψ are determined (Eqs. 4 and S32). However, the growth rate λ can be influenced by protein allocation between ϕ_r and ϕ_f with the governing equation Eq. 3. If $\varepsilon_f < \varepsilon_r$, then $\lambda = \frac{\phi_{\text{max}} - J_f^{(\text{E})} (1/\varepsilon_f - 1/\varepsilon_r)}{\psi + \phi/\varepsilon_r} \leq \frac{\phi_{\text{max}}}{\psi + \phi/\varepsilon_r}$. The optimal solution is $\phi_f = J_f^{(\text{E})} = 0$, which means that

the cell only uses respiration. Conversely, if $\varepsilon_f > \varepsilon_r$, $\phi_r = J_r^{(\text{E})} = 0$ is optimal, and the cell only uses fermentation. In either case, the optimal choice between respiration and fermentation is determined by weighing the proteome energy efficiencies.

In practice, both ε_r and ε_f are functions of κ_A (Eq. 4), and therefore the optimal choice may vary depending on the nutrient conditions. In nutrient-poor conditions where $\kappa_A \ll \kappa_r^{(A)}$ and $\kappa_A \ll \kappa_f^{(A)}$, the proteome energy efficiencies are reduced to $\varepsilon_r \approx \beta_r^{(A)} \cdot \kappa_A$ and $\varepsilon_f \approx \beta_f^{(A)} \cdot \kappa_A$ (see Eq. 4), where $\varepsilon_r(\kappa_A) > \varepsilon_f(\kappa_A)$. In rich media, however, using the parameters of κ_i derived from in vivo/in vitro experimental data of *Escherichia coli* (Appendix-table 1, see also Appendix 6.1-6.2 and Appendix-table 2), we confirm that $\varepsilon_r(\kappa_{\text{glucose}}^{(\text{ST})}) < \varepsilon_f(\kappa_{\text{glucose}}^{(\text{ST})})$ with Eq. 4 (see also Eqs. S39-

S40), where $\kappa_{\text{glucose}}^{(\text{ST})}$ represents the substrate quality of glucose at saturated concentration (abbreviated as “ST” in the superscript). Indeed, recent experimental studies have validated that $\varepsilon_r(\kappa_{\text{lactose}}^{(\text{ST})}) < \varepsilon_f(\kappa_{\text{lactose}}^{(\text{ST})})$ for lactose (Basan et al., 2015). In Fig. 1E, we present the growth rate dependence of proteome energy efficiencies ε_r and ε_f in a three-dimensional (3D) form using the data from Appendix-table 1, where ε_r , ε_f and the growth rate λ all vary as functions of κ_A . Therefore, the ratio $\varepsilon_f/\varepsilon_r$ (defined as $\Delta(\kappa_A)$) is a monotonically increasing function of κ_A , and there exists a critical value of κ_A (denoted as $\kappa_A^{(\text{C})}$, see Appendix 2.2 for details) satisfying $\Delta(\kappa_A^{(\text{C})}) = 1$. Below $\kappa_A^{(\text{C})}$, the cell grows slowly and the optimal choice is respiration (with $\varepsilon_f < \varepsilon_r$, $\lambda = \phi_{\text{max}} \cdot (\psi + \phi/\varepsilon_r)^{-1}$), while above $\kappa_A^{(\text{C})}$, the cell grows faster and the optimal growth strategy is fermentation (with $\varepsilon_f > \varepsilon_r$, $\lambda = \phi_{\text{max}} \cdot (\psi + \phi/\varepsilon_f)^{-1}$). The above analysis qualitatively explains the phenomenon of aerobic glycolysis.

For a quantitative understanding of overflow metabolism, let us first consider the homogeneous case, where all cells share identical biochemical parameters. For optimal protein allocation, the relation between fermentation flux and growth rate is $J_f^{(\text{E})} = \varphi \cdot \lambda \cdot \theta(\lambda - \lambda_{\text{C}})$, where “ θ ” represents the Heaviside step function, and λ_{C} is the critical growth rate for $\kappa_A^{(\text{C})}$ (i.e., $\lambda_{\text{C}} \equiv \lambda(\kappa_A^{(\text{C})})$). Similarly, we can determine the growth rate dependence of respiration flux, which is $J_r^{(\text{E})} = \varphi \cdot \lambda \cdot [1 - \theta(\lambda - \lambda_{\text{C}})]$. These digital response outcomes are consistent with the numerical simulation findings of Molenaar *et al.* (Molenaar et al., 2009). However, they are clearly incompatible with the threshold-analog response in the standard picture of overflow metabolism (Basan et al., 2015; Holms, 1996; Meyer et al., 1984; Nanchen et al., 2006).

To address this issue, we take into account cell heterogeneity, which is ubiquitous in both microbes (Ackermann, 2015; Bagamery et al., 2020; Balaban et al., 2004; Nikolic et al., 2013; Solopova et al., 2014; Wallden et al., 2016) and tumor cells (Duraj et al., 2021; Hanahan and Weinberg, 2011; Hensley et al., 2016). For the Warburg effect or overflow metabolism of our concern, experimental studies have reported significant metabolic heterogeneity in the choice between respiration and fermentation within a cell population (Bagamery et al., 2020; Duraj et al., 2021; Hensley et al., 2016; Nikolic et al., 2013). Motivated by the fact that the turnover number (k_{cat} value) of a catalytic enzyme varies considerably between in vitro and in vivo measurements (Davidi et al., 2016; García - Contreras et al., 2012), we note that the concentrations of potassium and phosphate, which vary from cell to cell, have a significant impact on the k_{cat} values of the metabolic enzymes (García - Contreras et al., 2012). Therefore, in a cell population, there is a distribution of values for k_{cat} , which is commonly referred to as extrinsic noise (Elowitz et al., 2002). For simplicity, we assume that each k_{cat} value follows a Gaussian distribution. This gives

the distributions of single-cell growth rate in various types of carbon sources (see Eqs. S155-S157, S163-S165), which are fully verified by recent experiments using isogenic *Escherichia coli* with single-cell resolution (Wallden et al., 2016) (Appendix-fig. 2B). Then, the critical growth rate λ_c should follow a Gaussian distribution $\mathcal{N}(\mu_{\lambda_c}, \sigma_{\lambda_c}^2)$ in the cell population (see Appendix 7 for details), where μ_{λ_c} is approximated by the deterministic result of λ_c (Eq. S43). We assume that the coefficient of variation (CV) is $\sigma_{\lambda_c}/\mu_{\lambda_c} = 12\%$, or equivalently, the CV for the catalytic rate of each metabolic enzyme is 25%. Thus, we have the growth rate dependence of fermentation and respiration fluxes (see Appendix 2.3 for details):

$$\begin{cases} J_f^{(N)}(\lambda) = \frac{\varphi \cdot \lambda}{\beta_f^{(A)}} \cdot \left[\operatorname{erf}\left(\frac{\lambda - \mu_{\lambda_c}}{\sqrt{2}\sigma_{\lambda_c}}\right) + 1 \right], \\ J_r^{(N)}(\lambda) = \frac{\varphi \cdot \lambda}{\beta_r^{(A)}} \cdot \left[1 - \operatorname{erf}\left(\frac{\lambda - \mu_{\lambda_c}}{\sqrt{2}\sigma_{\lambda_c}}\right) \right], \end{cases} \quad (5)$$

where “erf” represents the error function. The fermentation flux exhibits a threshold-analog relation with the growth rate (the red curves in Figs. 1C-D, 2B-C and 3B, D, F), while the respiration flux (the blue curve in Fig. 1D) decreases with an increase in fermentation flux. In Fig. 1C-D, we see that the model results (see Eq. 5 and Appendix 8; parameters are set by the experimental data shown in Appendix-table S1) agree quantitatively with the experimental data of *Escherichia coli* (Basan et al., 2015; Holms, 1996). The fermentation flux was determined by the acetate secretion rate $J_{\text{actate}}^{(M)} = 2J_f^{(N)}$, and the respiration flux was deduced from the carbon dioxide flux $J_{\text{CO}_2, r}^{(M)} = 6J_r^{(N)}$ (the superscript “(M)” represents the measurable flux in the unit of mM/OD600/h; see Appendix 8.1 for details). Therefore, with the integration of cell heterogeneity, our model of optimal protein allocation quantitatively explains overflow metabolism.

Testing the model through perturbations

To further test our model, we systematically investigate model predictions under various types of perturbations and compare them with the experimental data from existing studies (Basan et al., 2015; Holms, 1996) (see Appendices 3 and 4.1 for details).

First, we consider the proteomic perturbation by overexpression of useless proteins encoded by the LacZ gene (i.e., ϕ_Z perturbation) in *Escherichia coli*. The net effect of the ϕ_Z perturbation is that the maximum fraction of proteome available for resource allocation changes from ϕ_{\max} to $\phi_{\max} - \phi_Z$ (Basan et al., 2015), where ϕ_Z is the mass fraction of useless proteins. In a cell population, the critical growth rate $\lambda_c(\phi_Z)$ still follows a Gaussian distribution $\mathcal{N}(\mu_{\lambda_c}(\phi_Z), \sigma_{\lambda_c}(\phi_Z)^2)$,

where the CV of $\lambda_c(\phi_Z)$ remains unchanged. Consequently, the growth rate dependence of fermentation flux changes into $J_f^{(N)} = \frac{\varphi \cdot \lambda}{\beta_f^{(A)}} \cdot \left[\text{erf} \left(\frac{\lambda - \mu_{\lambda_c}(\phi_Z)}{\sqrt{2}\sigma_{\lambda_c}(\phi_Z)} \right) + 1 \right]$ (see Appendix 3 for model perturbation results of respiration flux), where both the growth rate $\lambda(\kappa_A, \phi_Z)$ and the normalized fermentation flux $J_f^{(N)}(\kappa_A, \phi_Z)$ are bivariate functions of κ_A and ϕ_Z (see Eqs. S49 and S56-S57). For each degree of LacZ expression (with fixed ϕ_Z), similar to the wild-type strains, the fermentation flux exhibits a threshold-analog response to growth rate as κ_A varies (Fig. 2C), which agrees quantitatively with experimental results (Basan et al., 2015). The shifts in the critical growth rate $\lambda_c(\phi_Z)$ are fully captured by $\mu_{\lambda_c}(\phi_Z) = \mu_{\lambda_c}(0)(1 - \phi_Z/\phi_{\max})$. In contrast, for nutrient conditions with each fixed κ_A , since the growth rate changes with ϕ_Z just like $\lambda_c(\phi_Z)$: $\lambda(\kappa_A, \phi_Z) = \lambda(\kappa_A, 0)(1 - \phi_Z/\phi_{\max})$, the fermentation flux is then proportional to the growth rate for the varying levels of LacZ expression: $J_f^{(N)} = \frac{\varphi}{\beta_f^{(A)}} \cdot \left[\text{erf} \left(\frac{\lambda(\kappa_A, 0) - \mu_{\lambda_c}(0)}{\sqrt{2}\sigma_{\lambda_c}(0)} \right) + 1 \right] \cdot \lambda$, where the slope is a monotonically increasing function of the substrate quality κ_A . These scaling relations are well validated by the experimental data (Basan et al., 2015) shown in Fig. 2B. Finally, in the case where both κ_A and ϕ_Z are free to vary, the growth rate dependence of fermentation flux presents a threshold-analog response surface in a 3D plot where ϕ_Z appears explicitly as the y-axis (Fig. 2A). Experimental data points (Basan et al., 2015) lie right on this surface (Fig. 2A), which are highly consistent with the model predictions.

Next, we study the influence of energy dissipation, which introduces an energy dissipation coefficient “ w ” in Eq. 2: $J_E^{(N)} = \eta_E \cdot \lambda + w$. Similarly, the critical growth rate $\lambda_c(w)$ follows a Gaussian distribution $\mathcal{N}(\mu_{\lambda_c}(w), \sigma_{\lambda_c}(w)^2)$ in a cell population. The relation between the growth rate and fermentation flux can be characterized by (see Appendix 3.2 for details): $J_f^{(N)} = \frac{\varphi \cdot \lambda + w}{\beta_f^{(A)}} \cdot \left[\text{erf} \left(\frac{\lambda - \mu_{\lambda_c}(w)}{\sqrt{2}\sigma_{\lambda_c}(w)} \right) + 1 \right]$. In Fig. 3A-B, we present a comparison between the model results and experimental data (Basan et al., 2015) in 3D and 2D plots, which demonstrate good agreement. A notable characteristic of energy dissipation, as distinguished from ϕ_Z perturbation, is that the fermentation flux increases despite a decrease in the growth rate when κ_A is fixed.

We proceed to analyze the impact of translation inhibition with different sub-lethal doses of chloramphenicol on *Escherichia coli*. This type of perturbation introduces an inhibition coefficient

“ ι ” in the translation rate, thus turning κ_i into $\kappa_i/(\iota+1)$. Still, the critical growth rate $\lambda_c(\iota)$ follows a Gaussian distribution $\mathcal{N}(\mu_{\lambda_c}(\iota), \sigma_{\lambda_c}(\iota)^2)$, and then, the growth rate dependence of fermentation flux is: $J_f^{(N)} = \frac{\varphi \cdot \lambda}{\beta_f^{(A)}} \cdot \left[\text{erf}\left(\frac{\lambda - \mu_{\lambda_c}(\iota)}{\sqrt{2}\sigma_{\lambda_c}(\iota)}\right) + 1 \right]$ (see Appendix 3.3 for details). In

Appendix-fig. 2D-E, we see that the model predictions are generally consistent with the experimental data (Basan et al., 2015). However, there is a noticeable systematic discrepancy when the translation rate is small. Therefore, we turn to maintenance energy, which is tiny and generally negligible for bacteria over the growth rate range of concern (Basan et al., 2015; Neidhardt, 1996). Encouragingly, by assigning a very small value to the maintenance energy coefficient “ w_0 ” ($w_0 = 2.5 \text{ (h}^{-1}\text{)}$), the model results for the growth rate-fermentation flux relation

$J_f^{(N)} = \frac{\varphi \cdot \lambda + w_0}{\beta_f^{(A)}} \cdot \left[\text{erf}\left(\frac{\lambda - \mu_{\lambda_c}(\iota)}{\sqrt{2}\sigma_{\lambda_c}(\iota)}\right) + 1 \right]$ agree quantitatively with experiments (Basan et al., 2015) (see Fig. 3C-D and Appendix 3.3 for details).

Finally, we consider the alteration of nutrient categories by switching to a non-Group A carbon source: pyruvate, which enters the metabolic network from the endpoint of glycolysis (Neidhardt et al., 1990; Nelson et al., 2008). The coarse-grained model for pyruvate utilization is shown in Fig. 3E (see also Fig. 1A), which shares identical precursor pools as those for Group A carbon sources (Fig. 1B), yet with several differences in the coarse-grained reactions. The growth rate dependencies of both the proteome energy efficiencies (Appendix-fig. 2H) and energy fluxes are qualitatively similar to those of the Group A carbon source utilization, while there are quantitative differences in the coarse-grained parameters (see Appendices 4.1 and 8 for details). Most notably, the critical growth rate $\lambda_c^{(\text{py})}$ and the ATP production per glucose in the fermentation pathway $\beta_f^{(\text{py})}$ are noticeably smaller than λ_c and $\beta_f^{(A)}$ (for Group A sources), respectively. Consequently, the growth rate dependence of fermentation flux in pyruvate should present a quite different curve from that of Group A carbon sources (see Eqs. 5 and S105), which is fully validated by experimental results (Holms, 1996) (Fig. 3F).

Enzyme allocation under perturbations

As mentioned above, our coarse-grained model is topologically identical to the central metabolic network (Fig. 1A), and thus it can predict enzyme allocation for each gene in glycolysis and the TCA cycle (see Appendix-fig. 1B and Appendix-table 1) under various types of perturbations. In Fig. 1B, the intermediate nodes M_1 , M_2 , M_3 , M_4 , and M_5 represent G6P, PEP, acetyl-CoA, α -ketoglutarate, and oxaloacetate, respectively. Then, ϕ_1 and ϕ_2 correspond to enzymes of glycolysis (or at the junction of glycolysis and the TCA cycle), while ϕ_3 and ϕ_4 correspond to enzymes in the TCA cycle.

We first consider enzyme allocation under carbon limitation by varying the nutrient type and concentration of a Group A carbon source (i.e., κ_A perturbation). In fact, this has been extensively studied in more simplified models (Hui et al., 2015; You et al., 2013), where the growth rate dependence of enzyme allocation under κ_A perturbation was generally considered to be a C-line response (Hui et al., 2015; You et al., 2013), i.e., the genes responsible for digesting carbon compounds show a linear increase in gene expression as the growth rate decreases (Hui et al., 2015; You et al., 2013). However, when it comes to enzymes catalyzing reactions between intermediate nodes, we collected experimental data from existing studies (Hui et al., 2015) and found that the enzymes in glycolysis exhibit a completely different response pattern compared to those in the TCA cycle (Appendix-fig. 3A-B). This discrepancy cannot be explained by the C-line response. To address this issue, we apply the coarse-grained model described above (Fig. 1B) to calculate the growth rate dependence of enzyme allocation for each ϕ_i ($i = 1, 2, 3, 4$) using the model settings for wild-type strains, where no fitting parameters are involved in determining the shape (see Eqs. S118-S119 and Appendix 8). In Fig. 4A-B and Appendix-fig. 3C-D, we see that the model predictions overall match with the experimental data (Hui et al., 2015) for representative genes from either glycolysis or the TCA cycle, and maintenance energy (with $w_0 = 2.5 \text{ (h}^{-1}\text{)})$ has a negligible effect on this process. Still, there are minor discrepancies that arise from the basal expression of metabolic genes, which may be attributed to the fact that our model deals with relatively stable growth conditions while microbes need to be prepared for fluctuating environments (Basan et al., 2020; Kussell and Leibler, 2005; Mori et al., 2017).

We proceed to analyze the influence of ϕ_Z perturbation and energy dissipation. In both cases, our model predicts a linear response to the growth rate reduction for all genes in either glycolysis or the TCA cycle (see Appendix 5.2-5.3 for details). For ϕ_Z perturbation, all predicted slopes are positive, and there are no fitting parameters involved (Eqs. S120-S121). In Fig. 4C-D and Appendix-fig. 3E-J, we show that our model quantitatively illustrates the experimental data (Basan et al., 2015) for representative genes in the central metabolic network, and there is a better agreement with experiments (Basan et al., 2015) by incorporating the maintenance energy (with $w_0 = 2.5 \text{ (h}^{-1}\text{)})$. For energy dissipation, however, the predicted slopes of the enzymes corresponding to ϕ_4 are surely negative, and there is a constraint that the slope signs of the enzymes corresponding to the same ϕ_i ($i = 1, 2, 3$) should be the same. In Appendix-fig. 3K-N, we see that the model results (Eqs. S127 and S123) are consistent with experiments (Basan et al., 2015).

Discussion

The phenomenon of overflow metabolism, or the Warburg effect, has been a long-standing puzzle in cell metabolism. Although many rationales have been proposed (Basan et al., 2015; Chen and Nielsen, 2019; Majewski and Domach, 1990; Molenaar et al., 2009; Nebel et al., 2019; Pfeiffer et al., 2001; Shlomi et al., 2011; Vander Heiden et al., 2009; Varma and Palsson, 1994; Vazquez et al., 2010; Vazquez and Oltvai, 2016) over the past century, the origin and function of this

phenomenon remain unclear (DeBerardinis and Chandel, 2020; Hanahan and Weinberg, 2011; Liberti and Locasale, 2016; Vander Heiden et al., 2009). In this study, we use *Escherichia coli* as a typical example and demonstrate that overflow metabolism can be understood through optimal protein allocation combined with cell heterogeneity. In nutrient-poor conditions, the proteome energy efficiency of respiration is higher than that of fermentation (Fig. 1E), and thus the cell uses respiration to optimize growth. In rich media, however, the proteome energy efficiency of fermentation increases faster and is higher than that of respiration (Fig. 1E), leading the cell to use fermentation to accelerate growth. In further combination with cell heterogeneity in enzyme catalytic rates (Davidi et al., 2016; García - Contreras et al., 2012), our model quantitatively illustrates the threshold-analog response (Basan et al., 2015; Holms, 1996) in overflow metabolism (Fig. 1C).

Cell heterogeneity is crucial for the threshold-analog response in overflow metabolism. In the homogeneous case, the optimal solution is a digital response (Eq. S44) that corresponds to an elementary flux mode (Müller et al., 2014; Wortel et al., 2014) and agrees with the numerical study of Molenaar *et al.* (Molenaar et al., 2009). However, this digital response is incompatible with the standard picture of overflow metabolism (Basan et al., 2015; Holms, 1996; Meyer et al., 1984; Nanchen et al., 2006). By incorporating heterogeneity in enzyme catalytic rates (Davidi et al., 2016; García - Contreras et al., 2012), the critical growth rate (i.e., threshold) changes from a single value into a Gaussian distribution (Eq. 45, see Appendix 7 for details; see also Appendix-fig. 4) for a cell population, thus turning a digital response into the threshold-analog response in overflow metabolism (Fig. 1C). Our model results relying on cell heterogeneity are fully validated by the observed distributions of single-cell growth rate (Wallden et al., 2016) (Appendix-fig. 2B) and experiments with various types of perturbations (Basan et al., 2015; Holms, 1996; Hui et al., 2015), both for acetate secretion patterns and gene expression in the central metabolic network (Fig. 2-4, Appendix-figs. 2D-E and 3).

Finally, our model can be broadly used to address heterogeneity-related challenges in metabolism on a quantitative basis, including the Crabtree effect in yeast (Bagamery et al., 2020; De Deken, 1966), the Warburg effect in cancer (Duraj et al., 2021; Hanahan and Weinberg, 2011; Liberti and Locasale, 2016; Vander Heiden et al., 2009) (see Appendix 6.4 for an explanation of the Warburg effect), and the heterogeneous metabolic strategies of cells in various types of environments (Bagamery et al., 2020; Duraj et al., 2021; Escalante-Chong et al., 2015; Hensley et al., 2016; Liu et al., 2015; Solopova et al., 2014; Wang et al., 2019).

Author contributions

X.W. conceived and designed the project, developed the model, carried out the analytical/numerical calculations, and wrote the paper.

Competing Interest Statement:

The author declares no competing interests.

Data, Materials, and Software Availability.

All study data are included in the article and/or appendices.

Acknowledgements

The author thanks Chao Tang, Qi Ouyang, Yang-Yu Liu and Kang Xia for helpful discussions. This work was supported by National Natural Science Foundation of China (Grant No.12004443), Guangzhou Municipal Innovation Fund (Grant No.202102020284) and the Hundred Talents Program of Sun Yat-sen University.

References

- Ackermann, M. (2015). A functional perspective on phenotypic heterogeneity in microorganisms. *Nature Reviews Microbiology* 13, 497-508.
- Bagamery, L.E., Justman, Q.A., Garner, E.C., and Murray, A.W. (2020). A putative bet-hedging strategy buffers budding yeast against environmental instability. *Current Biology* 30, 4563-4578. e4564.
- Balaban, N.Q., Merrin, J., Chait, R., Kowalik, L., and Leibler, S. (2004). Bacterial persistence as a phenotypic switch. *Science* 305, 1622-1625.
- Basan, M., Honda, T., Christodoulou, D., Hörl, M., Chang, Y.-F., Leoncini, E., Mukherjee, A., Okano, H., Taylor, B.R., Silverman, J.M., et al. (2020). A universal trade-off between growth and lag in fluctuating environments. *Nature* 584, 470-474.
- Basan, M., Hui, S., Okano, H., Zhang, Z., Shen, Y., Williamson, J.R., and Hwa, T. (2015). Overflow metabolism in *Escherichia coli* results from efficient proteome allocation. *Nature* 528, 99-104.
- Bennett, B.D., Kimball, E.H., Gao, M., Osterhout, R., Van Dien, S.J., and Rabinowitz, J.D. (2009). Absolute metabolite concentrations and implied enzyme active site occupancy in *Escherichia coli*. *Nature Chemical Biology* 5, 593-599.
- Chen, Y., and Nielsen, J. (2019). Energy metabolism controls phenotypes by protein efficiency and allocation. *Proceedings of the National Academy of Sciences* 116, 17592-17597.
- Dai, X., Zhu, M., Warren, M., Balakrishnan, R., Patsalo, V., Okano, H., Williamson, J.R., Fredrick, K., Wang, Y.-P., and Hwa, T. (2016). Reduction of translating ribosomes enables *Escherichia coli* to maintain elongation rates during slow growth. *Nature Microbiology* 2, 1-9.
- Davidi, D., Noor, E., Liebermeister, W., Bar-Even, A., Flamholz, A., Tummli, K., Barenholz, U., Goldenfeld, M., Shlomi, T., and Milo, R. (2016). Global characterization of in vivo enzyme catalytic rates and their correspondence to in vitro kcat measurements. *Proceedings of the National Academy of Sciences* 113, 3401-3406.
- De Deken, R. (1966). The Crabtree effect: a regulatory system in yeast. *Microbiology* 44, 149-156.

DeBerardinis, R.J., and Chandel, N. (2020). We need to talk about the Warburg effect. *Nature Metabolism* 2, 127-129.

Dekel, E., and Alon, U. (2005). Optimality and evolutionary tuning of the expression level of a protein. *Nature* 436, 588-592.

Duraj, T., García-Romero, N., Carrión-Navarro, J., Madurga, R., Ortiz de Mendivil, A., Prat-Acin, R., Garcia-Cañamaque, L., and Ayuso-Sacido, A. (2021). Beyond the Warburg effect: Oxidative and glycolytic phenotypes coexist within the metabolic heterogeneity of glioblastoma. *Cells* 10, 202.

Edwards, J.S., Ibarra, R.U., and Palsson, B.O. (2001). In silico predictions of Escherichia coli metabolic capabilities are consistent with experimental data. *Nature biotechnology* 19, 125-130.

Elowitz, M.B., Levine, A.J., Siggia, E.D., and Swain, P.S. (2002). Stochastic gene expression in a single cell. *Science* 297, 1183-1186.

Escalante-Chong, R., Savir, Y., Carroll, S.M., Ingraham, J.B., Wang, J., Marx, C.J., and Springer, M. (2015). Galactose metabolic genes in yeast respond to a ratio of galactose and glucose. *Proceedings of the National Academy of Sciences* 112, 1636-1641.

García-Contreras, R., Vos, P., Westerhoff, H.V., and Boogerd, F.C. (2012). Why in vivo may not equal in vitro—new effectors revealed by measurement of enzymatic activities under the same in vivo-like assay conditions. *The FEBS Journal* 279, 4145-4159.

Hanahan, D., and Weinberg, R.A. (2011). Hallmarks of cancer: the next generation. *Cell* 144, 646-674.

Hensley, C.T., Faubert, B., Yuan, Q., Lev-Cohain, N., Jin, E., Kim, J., Jiang, L., Ko, B., Skelton, R., Loudat, L., et al. (2016). Metabolic heterogeneity in human lung tumors. *Cell* 164, 681-694.

Holms, H. (1996). Flux analysis and control of the central metabolic pathways in Escherichia coli. *FEMS Microbiology Reviews* 19, 85-116.

Hui, S., Silverman, J.M., Chen, S.S., Erickson, D.W., Basan, M., Wang, J., Hwa, T., and Williamson, J.R. (2015). Quantitative proteomic analysis reveals a simple strategy of global resource allocation in bacteria. *Molecular Systems Biology* 11, 784.

Kostinski, S., and Reuveni, S. (2020). Ribosome composition maximizes cellular growth rates in E. coli. *Physical Review Letters* 125, 028103.

Kussell, E., and Leibler, S. (2005). Phenotypic diversity, population growth, and information in fluctuating environments. *Science* 309, 2075-2078.

Li, S.H.-J., Li, Z., Park, J.O., King, C.G., Rabinowitz, J.D., Wingreen, N.S., and Gitai, Z. (2018). Escherichia coli translation strategies differ across carbon, nitrogen and phosphorus limitation conditions. *Nature Microbiology* 3, 939-947.

Liberti, M.V., and Locasale, J.W. (2016). The Warburg effect: how does it benefit cancer cells? *Trends in Biochemical Sciences* 41, 211-218.

Liu, X., Wang, X., Yang, X., Liu, S., Jiang, L., Qu, Y., Hu, L., Ouyang, Q., and Tang, C. (2015). Reliable cell cycle commitment in budding yeast is ensured by signal integration. *eLife* 4, e03977.

Majewski, R., and Domach, M. (1990). Simple constrained-optimization view of acetate overflow in E. coli. *Biotechnology Bioengineering* 35, 732-738.

Meyer, H.-P., Leist, C., and Fiechter, A. (1984). Acetate formation in continuous culture of *Escherichia coli* K12 D1 on defined and complex media. *Journal of Biotechnology* 1, 355-358.

Molenaar, D., Van Berlo, R., De Ridder, D., and Teusink, B. (2009). Shifts in growth strategies reflect tradeoffs in cellular economics. *Molecular Systems Biology* 5, 323.

Mori, M., Schink, S., Erickson, D.W., Gerland, U., and Hwa, T. (2017). Quantifying the benefit of a proteome reserve in fluctuating environments. *Nature Communications* 8, 1225.

Müller, S., Regensburger, G., and Steuer, R. (2014). Enzyme allocation problems in kinetic metabolic networks: Optimal solutions are elementary flux modes. *Journal of Theoretical Biology* 347, 182-190.

Nanchen, A., Schicker, A., and Sauer, U. (2006). Nonlinear dependency of intracellular fluxes on growth rate in miniaturized continuous cultures of *Escherichia coli*. *Applied Environmental Microbiology* 72, 1164-1172.

Neidhardt, F.C. (1996). *Escherichia coli* and *Salmonella*: cellular and molecular biology. (Washington, DC: ASM Press).

Neidhardt, F.C., Ingraham, J.L., and Schaechter, M. (1990). *Physiology of the bacterial cell*. (Sinauer associates).

Nelson, D.L., Lehninger, A.L., and Cox, M.M. (2008). *Lehninger principles of biochemistry*. (Macmillan).

Niebel, B., Leupold, S., and Heinemann, M. (2019). An upper limit on Gibbs energy dissipation governs cellular metabolism. *Nature Metabolism* 1, 125-132.

Nikolic, N., Barner, T., and Ackermann, M. (2013). Analysis of fluorescent reporters indicates heterogeneity in glucose uptake and utilization in clonal bacterial populations. *BMC Microbiology* 13, 1-13.

Park, J.O., Rubin, S.A., Xu, Y.-F., Amador-Noguez, D., Fan, J., Shlomi, T., and Rabinowitz, J.D. (2016). Metabolite concentrations, fluxes and free energies imply efficient enzyme usage. *Nature Chemical Biology* 12, 482-489.

Pfeiffer, T., Schuster, S., and Bonhoeffer, S. (2001). Cooperation and competition in the evolution of ATP-producing pathways. *Science* 292, 504-507.

Scott, M., Gunderson, C.W., Mateescu, E.M., Zhang, Z., and Hwa, T. (2010). Interdependence of cell growth and gene expression: origins and consequences. *Science* 330, 1099-1102.

Shlomi, T., Benyamini, T., Gottlieb, E., Sharan, R., and Ruppin, E. (2011). Genome-scale metabolic modeling elucidates the role of proliferative adaptation in causing the Warburg effect. *PLoS Computational Biology* 7, e1002018.

Solopova, A., Van Gestel, J., Weissing, F.J., Bachmann, H., Teusink, B., Kok, J., and Kuipers, O.P. (2014). Bet-hedging during bacterial diauxic shift. *Proceedings of the National Academy of Sciences* 111, 7427-7432.

Towbin, B.D., Korem, Y., Bren, A., Doron, S., Sorek, R., and Alon, U. (2017). Optimality and sub-optimality in a bacterial growth law. *Nature Communications* 8, 14123.

Vander Heiden, M.G., Cantley, L.C., and Thompson, C.B. (2009). Understanding the Warburg effect: the metabolic requirements of cell proliferation. *Science* 324, 1029-1033.

- Varma, A., and Palsson, B.O. (1994). Stoichiometric flux balance models quantitatively predict growth and metabolic by-product secretion in wild-type *Escherichia coli* W3110. *Applied Environmental Microbiology* *60*, 3724-3731.
- Vazquez, A., Liu, J., Zhou, Y., and Oltvai, Z.N. (2010). Catabolic efficiency of aerobic glycolysis: the Warburg effect revisited. *BMC Systems Biology* *4*, 1-9.
- Vazquez, A., and Oltvai, Z.N. (2016). Macromolecular crowding explains overflow metabolism in cells. *Scientific Reports* *6*, 31007.
- Wallden, M., Fange, D., Lundius, E.G., Baltekin, Ö., and Elf, J. (2016). The synchronization of replication and division cycles in individual *E. coli* cells. *Cell* *166*, 729-739.
- Wang, X., Xia, K., Yang, X., and Tang, C. (2019). Growth strategy of microbes on mixed carbon sources. *Nature Communications* *10*, 1279.
- Warburg, O., Posener, K., and Negelein, E. (1924). Über den Stoffwechsel der Carcinomzelle. *Biochemische Zeitschrift* *152*, 309-344.
- Wortel, M.T., Peters, H., Hulshof, J., Teusink, B., and Bruggeman, F.J. (2014). Metabolic states with maximal specific rate carry flux through an elementary flux mode. *The FEBS Journal* *281*, 1547-1555.
- You, C., Okano, H., Hui, S., Zhang, Z., Kim, M., Gunderson, C.W., Wang, Y.-P., Lenz, P., Yan, D., and Hwa, T. (2013). Coordination of bacterial proteome with metabolism by cyclic AMP signalling. *Nature* *500*, 301-306.

Figures

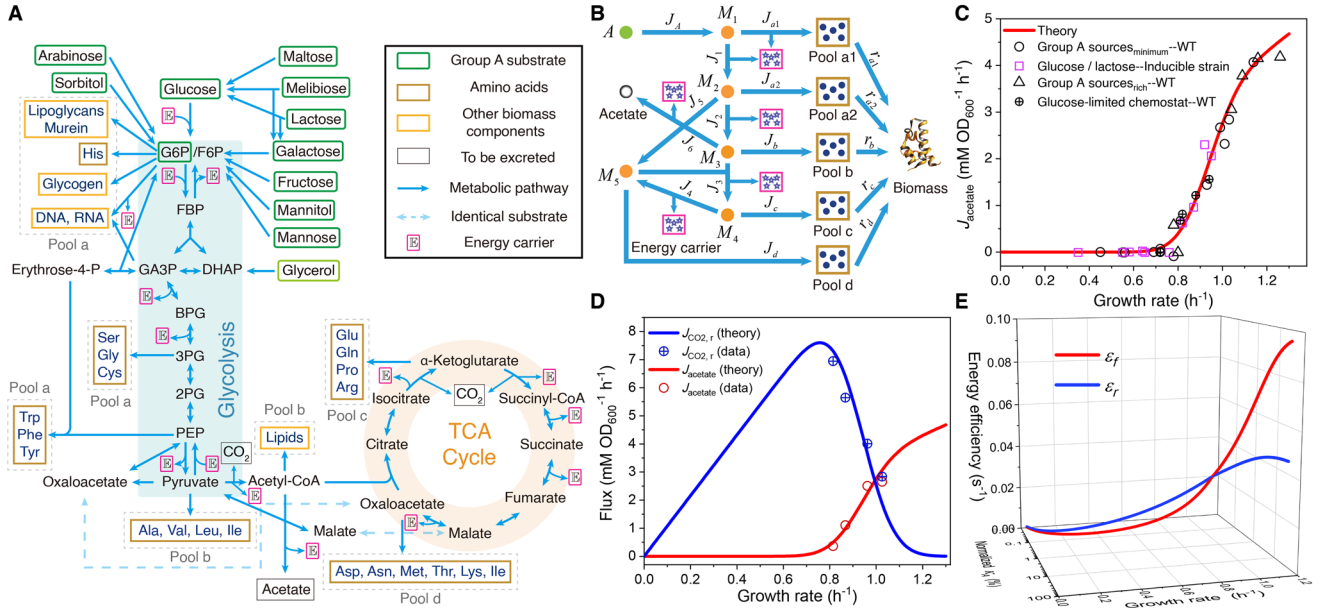


Fig. 1 | Model and results of overflow metabolism. (A) The central metabolic network of carbon source utilization. The Group A carbon sources (Wang et al., 2019) are labeled with green squares. (B) Coarse-grained model for Group A carbon source utilization. (C) Model predictions (Eqs. S47 and S160) and experimental results (Basan et al., 2015; Holms, 1996) of overflow metabolism, covering the data for all the Group A carbon sources shown in (A). (D) Growth rate dependence of respiration and fermentation fluxes (Eqs. S47 and S160). (E) The energy efficiencies of respiration and fermentation pathways vary with the growth rate as functions of the substrate quality of a Group A carbon source (Eqs. S31 and S36). See Appendix 8 for model parameter settings and experimental data sources (Basan et al., 2015; Holms, 1996; Hui et al., 2015) of Figs. 1-4.

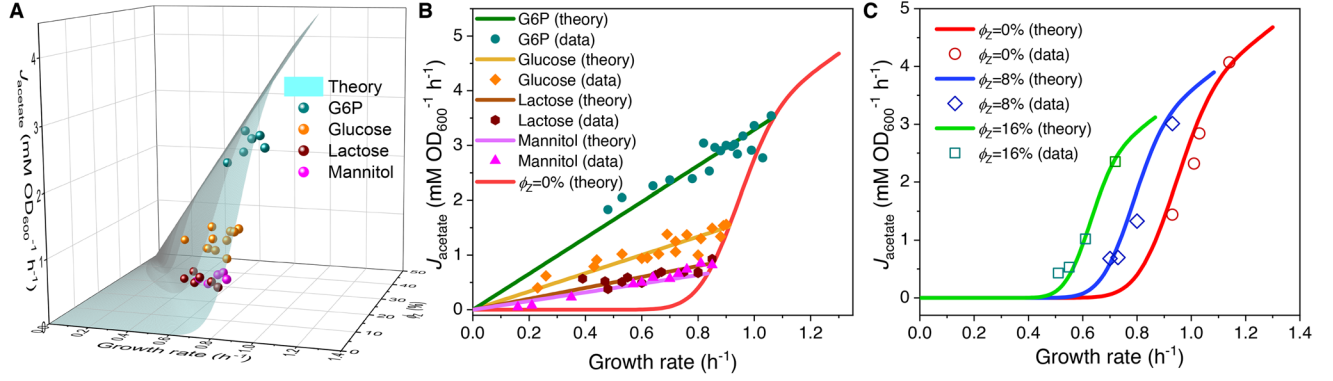


Fig. 2 | Influence of protein overexpression on overflow metabolism. (A) A 3D plot of the relations among fermentation flux, growth rate, and the expression level of useless proteins. In this plot, both the acetate excretion rate and growth rate vary as bivariate functions of the substrate quality of a Group A carbon source (denoted as κ_A) and the useless protein expression encoded by LacZ (denoted as ϕ_Z perturbation, see Eqs. S57 and S160). (B) Growth rate dependence of the acetate excretion rate upon ϕ_Z perturbation for each fixed nutrient condition (Eq. S58 and S160). (C) Growth rate dependence of the acetate excretion rate as κ_A varies (Eqs. S57 and S160), with each fixed expression level of LacZ.

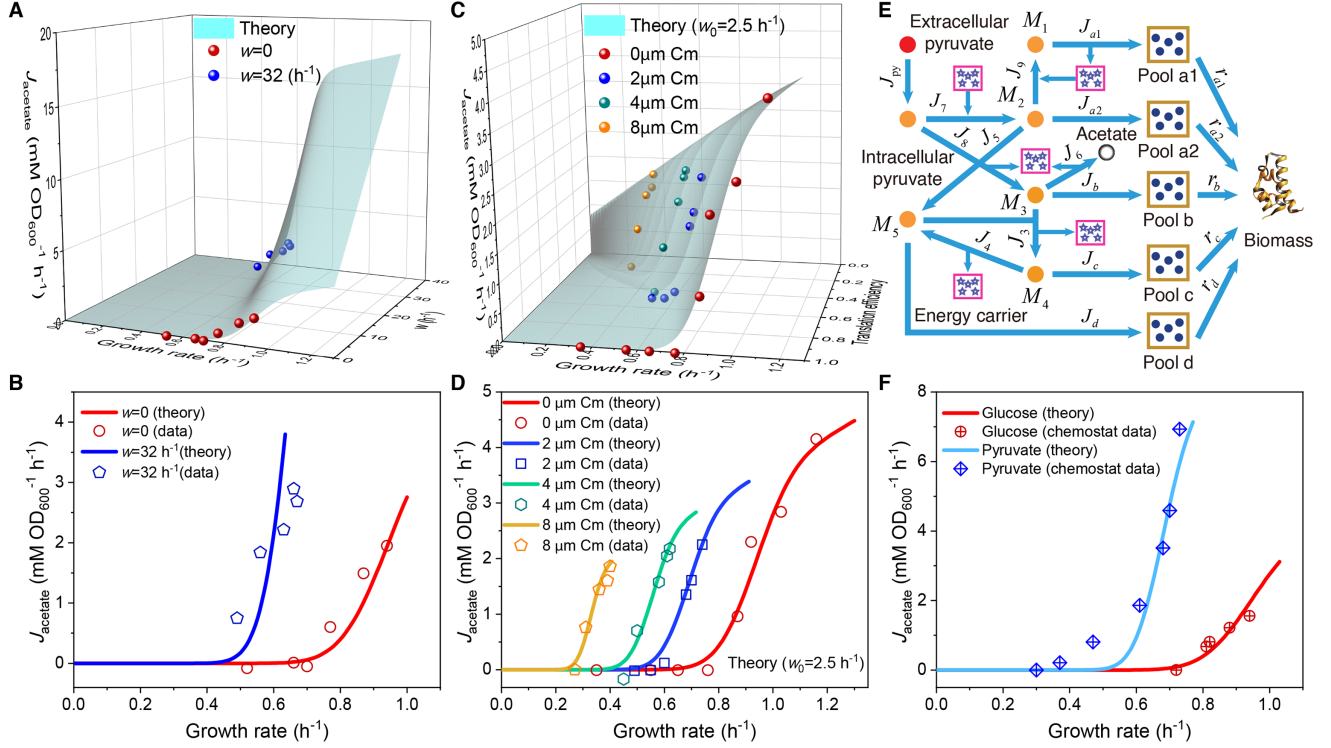


Fig. 3 | Influence of energy dissipation, translation inhibition, and carbon source category alteration on overflow metabolism. (A) A 3D plot of the relations among fermentation flux, growth rate, and the energy dissipation coefficient (Eqs. S70 and S160). (B) Growth rate dependence of the acetate excretion rate as κ_A varies, with each fixed energy dissipation coefficient determined by/fitted from experimental data. (C) A 3D plot of the relations among fermentation flux, growth rate, and the translation efficiency (Eqs. 85 and S160). Here, the translation efficiency is adjusted by the dose of chloramphenicol (Cm). (D) Growth rate dependence of the acetate excretion rate as κ_A varies, with each fixed dose of Cm. (E) Coarse-grained model for pyruvate utilization. (F) The growth rate dependence of fermentation flux in pyruvate (Eqs. 105 and S160) significantly differs from that of the Group A carbon sources (Eqs. 47 and S160).

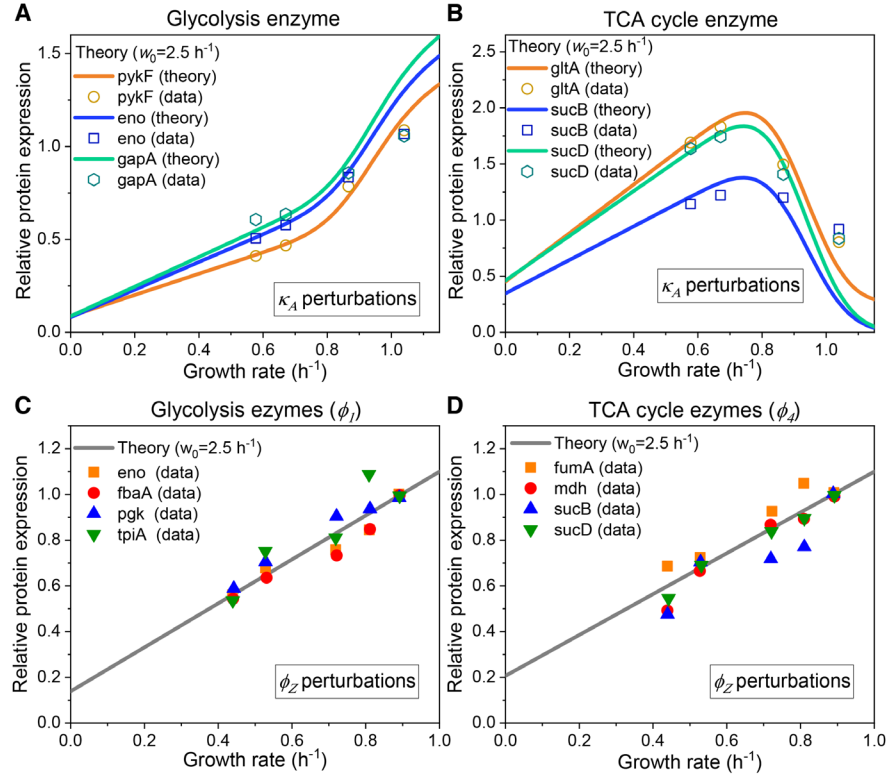


Fig. 4 | Relative protein expression of central metabolic enzymes under κ_A and ϕ_Z perturbations. (A, C) Relative protein expression of representative genes from glycolysis. (B, D) Relative protein expression of representative genes from the TCA cycle. (A, B) Results of κ_A perturbation (Eq. S119). (C, D) Results of ϕ_Z perturbation (Eq. S121).

Appendices for

Overflow metabolism originates from growth optimization and cell heterogeneity

Xin Wang^{*}

^{*}Correspondence: wangxin36@mail.sysu.edu.cn

This PDF file includes:

Appendices 1-8
Appendix-figures 1-4
Appendix-tables 1-2
Appendix References

Other supporting materials for this manuscript include the following:

Appendix-source data 1-2

Appendix 1 Model framework.....	1
Appendix 1.1 Proteome partition.....	1
Appendix 1.2 Precursor pools	1
Appendix 1.3 Stoichiometric flux	2
Appendix 1.4 Carbon flux and cell growth rate	2
Appendix 1.5 Intermediate nodes.....	4
Appendix 2 Model and analysis.....	4
Appendix 2.1 Coarse-grained model	4
Appendix 2.2 The reason for overflow metabolism.....	7
Appendix 2.3 The relation between respiration/fermentation fluxes and growth rate	9
Appendix 3 Model perturbations	11
Appendix 3.1 Overexpression of useless proteins.....	11
Appendix 3.2 Energy dissipation.....	14
Appendix 3.3 Translation inhibition.....	16
Appendix 4 Overflow metabolism in substrates other than Group A carbon sources.....	20
Appendix 4.1 Pyruvate	20
Appendix 4.2 Mixture of a Group A carbon source with extracellular amino acids.....	24
Appendix 5 Enzyme allocation upon perturbations.....	26
Appendix 5.1 Carbon limitation within Group A carbon sources	26
Appendix 5.2 Overexpression of useless proteins.....	27
Appendix 5.3 Energy dissipation.....	29
Appendix 6 Other aspects of the model.....	30
Appendix 6.1 A coarse-grained model with more details	30
Appendix 6.2 Estimation of the in vivo enzyme catalytic rates	32
Appendix 6.3 Comparison with existing models that illustrate experimental results	32
Appendix 6.4 Explanation of the Warburg effect in tumor cells.....	34
Appendix 7 Probability density functions of variables and parameters	35
Appendix 7.1 Probability density function of κ_i	35
Appendix 7.2 Probability density function of the growth rate λ	38

Appendix 8 Model comparison with experiments	39
Appendix 8.1 Flux comparison with experiments.....	39
Appendix 8.2 Model parameter settings using experimental data.....	40
Appendix 8.3 Notes on the application of reference data.....	43
Appendix Tables	45
Appendix-table 1. Molecular weight and in vivo/ in vitro k_{cat} data for <i>E. coli</i>	45
Appendix-table 2. Proteome and flux data used to calculate the in vivo k_{cat}	47
Appendix Figures.....	48
Appendix-figure 1. Central metabolic network and carbon utilization pathways.	48
Appendix-figure 2. Model and results for experimental comparison.....	49
Appendix-figure 3. Relative protein expression of central metabolic enzymes under various types of perturbations.	51
Appendix-figure 4. Asymptotic distributions of inverse Gaussian distribution and the inverse of Gaussian distribution.....	53
Appendix References	54

Appendix 1 Model framework

Appendix 1.1 Proteome partition

Here we adopt the proteome partition framework similar to that introduced by Scott *et al.* (Scott et al., 2010). All proteins in a cell are classified into three classes: the fixed portion Q-class, the active ribosome-affiliated R-class, and the remaining catabolic/anabolic enzymes C-class. Each proteome class has a mass $M_i^{(p)}$ ($i = Q, R, C$) and mass fraction ϕ_i , where ϕ_Q is a constant, and we define $\phi_{\max} \equiv 1 - \phi_Q$. In the exponential growth phase, the ribosome allocation for protein synthesis of each class is f_i , with $f_Q + f_R + f_C = 1$.

To analyze cell growth optimization, we first consider the homogeneous case where all cells share identical biochemical parameters and simplify the mass accumulation of a cell population into a big cell. Essentially, this approximation would not influence the value of growth rate λ . For bacteria, the protein turnover rate is negligible, and thus the mass accumulation of each class follows:

$$dM_i^{(p)}/dt = f_i \cdot k_T \cdot N_R \cdot m_{AA} \quad (i = Q, R, C), \quad (S1)$$

where m_{AA} stands for the average molecular weight of amino acids, k_T is the translation rate, $N_R = M_{rp}^{(p)}/m_R$ is the number of ribosomes, m_R is the protein mass of a single ribosome, and $M_{rp}^{(p)}$ is the protein mass of the ribosomes with $M_R^{(p)}/M_{rp}^{(p)} = \varsigma \approx 1.67$ (Neidhardt, 1996; Scott et al., 2010). For a specific stable nutrient environment, f_R and k_T are temporal invariants. Then,

$$M_i^{(p)}(t) = M_i^{(p)}(0) + f_i/f_R \cdot M_R^{(p)}(0) \cdot [\exp(\lambda \cdot t) - 1] \quad (i = Q, R, C), \quad (S2)$$

where $\lambda = f_R \cdot k_T \cdot m_{AA}/(\varsigma \cdot m_R)$, and the protein mass of the cell population $M_{\text{protein}} \equiv \sum_i^{Q,R,C} M_i^{(p)}$ follows:

$$M_{\text{protein}}(t) = M_{\text{protein}}(0) + M_R(0) \cdot [\exp(\lambda \cdot t) - 1]/f_R. \quad (S3)$$

Over a long period in the exponential growth phase ($t \rightarrow +\infty$), $\phi_i = f_i$ ($i = Q, R, C$) and

$$\lambda = \phi_R \cdot \kappa_t, \quad (S4)$$

where $\kappa_t = k_T \cdot m_{AA}/(\varsigma \cdot m_R)$.

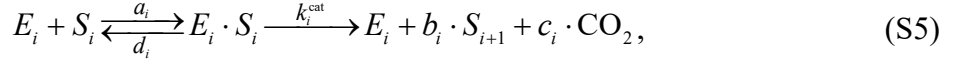
Appendix 1.2 Precursor pools

Based on the entry point of the metabolic network, we classify the precursors of biomass components into five pools (Fig. 1A-B): a1 (entry point: G6P/F6P), a2 (entry point: GA3P/3PG/PEP), b (entry point: pyruvate/acetyl-CoA), c (entry point: α -ketoglutarate) and d

(entry point: oxaloacetate). For bacteria, these five pools draw roughly $r_{a1} = 24\%$, $r_{a2} = 24\%$, $r_b = 28\%$, $r_c = 12\%$ and $r_d = 12\%$ of the carbon flux (Nelson et al., 2008; Wang et al., 2019). There are overlapping components between Pools a1 and a2 due to the joint synthesis of some precursors, thus we also use Pool a to represent Pools a1-a2 in the descriptions.

Appendix 1.3 Stoichiometric flux

We consider the following biochemical reaction between substrate S_i and enzyme E_i :



where a_i , d_i and k_i^{cat} are the reaction parameters, S_{i+1} is the product, b_i and c_i are the stoichiometric coefficients. For most of the reactions in the central metabolism, $b_i = 1$ and $c_i = 0$. The reaction rate follows Michaelis–Menten kinetics (Nelson et al., 2008):

$$v_i = k_i^{\text{cat}} \cdot [E_i] \cdot \frac{[S_i]}{[S_i] + K_i}, \quad (\text{S6})$$

where $K_i \equiv (d_i + k_i^{\text{cat}})/a_i$, $[E_i]$ and $[S_i]$ are the concentrations of enzyme E_i and substrate S_i , respectively. For this reaction (Eq. S5), $d[S_{i+1}]/dt = b_i \cdot v_i$ and $d[S_i]/dt = -v_i$. In the cell populations (the “big cell”), suppose that the cell volume is V_{cell} , then the stoichiometric flux of the reaction is:

$$J_i \equiv V_{\text{cell}} \cdot v_i. \quad (\text{S7})$$

The copy number of enzyme E_i is $N_{E_i} = V_{\text{cell}} \cdot [E_i]$ with a total weight of $M_{E_i} = N_{E_i} \cdot m_{E_i}$, where m_{E_i} is the molecular weight of E_i . By defining the enzyme cost of an E_i molecule as $n_{E_i} \equiv m_{E_i}/m_0$, where m_0 is a unit mass, then the cost of all E_i molecules is $\Phi_i \equiv N_{E_i} \cdot n_{E_i}$ (Wang et al., 2019). By further defining $\xi_i \equiv \frac{k_i^{\text{cat}}}{n_{E_i}} \cdot \frac{[S_i]}{[S_i] + K_i}$, then,

$$J_i = \Phi_i \cdot \xi_i. \quad (\text{S8})$$

The mass fraction of E_i is $\phi_i = M_{E_i}/M_{\text{protein}}$, and thus

$$\phi_i = \Phi_i \cdot \frac{m_0}{M_{\text{protein}}}. \quad (\text{S9})$$

Appendix 1.4 Carbon flux and cell growth rate

To clarify the relation between the stoichiometric flux J_i and growth rate λ , we consider the carbon flux in the biomass production. The carbon mass of the cell population (the “big cell”) is given by $M_{\text{carbon}} = M_{\text{protein}} \cdot r_{\text{carbon}} / r_{\text{protein}}$, where r_{carbon} and r_{protein} represent the mass fraction of carbon and protein within a cell. In the exponential growth phase, the carbon flux of the biomass production is given by:

$$J_{\text{BM}} = \frac{1}{m_{\text{carbon}}} \cdot \frac{dM_{\text{carbon}}}{dt} = \lambda \cdot \frac{M_{\text{carbon}}}{m_{\text{carbon}}}, \quad (\text{S10})$$

where m_{carbon} is the mass of a carbon atom. In fact, the carbon mass flux per stoichiometry varies depending on the entry point of the precursor pool. Taking Pool b as an example, there are three carbon atoms in a molecule of the entry point metabolite (i.e., pyruvate). Assuming that carbon atoms are conserved from pyruvate to Pool b, then the carbon flux of Pool b is given by $J_b^{\text{carbon}} = J_b \cdot N_{\text{py}}^{\text{carbon}}$, where J_b is the stoichiometric flux from pyruvate to Pool b (Fig. 1A-B) and $N_{\text{py}}^{\text{carbon}}$ stands for the carbon number of a pyruvate molecule. Combining with Eq. S10 and noting that $J_b^{\text{carbon}} = r_b \cdot J_{\text{BM}}$, we get $J_b \cdot N_{\text{py}}^{\text{carbon}} \cdot m_{\text{carbon}} = r_b \cdot \lambda \cdot M_{\text{carbon}}$. Similarly, for each precursor pool, we have:

$$J_i \cdot N_{\text{EP}_i}^{\text{carbon}} \cdot m_{\text{carbon}} = r_i \cdot \lambda \cdot M_{\text{carbon}} \quad (i = a1, a2, b, c, d), \quad (\text{S11})$$

where the subscript “EP_{*i*}” represents the entry point of Pool *i*, and $N_{\text{EP}_i}^{\text{carbon}}$ stands for the number of carbon atoms in a molecule of the entry point metabolite.

For each substrate in intermediate steps of the metabolic network, we define κ_i as the substrate quality:

$$\kappa_i \equiv \xi_i \cdot \frac{r_{\text{protein}}}{r_{\text{carbon}}} = \frac{r_{\text{protein}}}{r_{\text{carbon}}} \cdot \frac{k_i^{\text{cat}}}{n_{E_i}} \cdot \frac{[S_i]}{[S_i] + K_i}, \quad (\text{S12})$$

and for each precursor pool, we define:

$$\eta_i \equiv r_i \cdot m_0 / (N_{\text{EP}_i}^{\text{carbon}} \cdot m_{\text{carbon}}) \quad (i = a1, a2, b, c, d). \quad (\text{S13})$$

Combining Eqs. S8, S9 and S11, we have

$$\phi_i \cdot \kappa_i = \eta_i \cdot \lambda \quad (i = a1, a2, b, c, d). \quad (\text{S14})$$

Then, we define the normalized flux, which can be regarded as the flux per unit of biomass:

$$J_i^{(\text{N})} \equiv \phi_i \cdot \kappa_i, \quad (\text{S15})$$

where the superscript “(N)” stands for normalized. Combined with Eqs. S8, S9 and S12, we have:

$$J_i^{(N)} \equiv J_i \cdot \frac{m_0}{M_{\text{carbon}}} . \quad (\text{S16})$$

Since $\sum_i^{a1,a2,b,c,d} r_i = 1$, by setting

$$m_0 = \left[\sum_i r_i / N_{\text{EP}_i}^{\text{carbon}} \right]^{-1} \cdot m_{\text{carbon}} , \quad (\text{S17})$$

then,

$$\eta_i = \frac{r_i}{N_{\text{EP}_i}^{\text{carbon}}} \cdot \left[\sum_j^{a1,a2,b,c,d} \frac{r_j}{N_{\text{EP}_j}^{\text{carbon}}} \right]^{-1} \quad (i = a1, a2, b, c, d) , \quad (\text{S18})$$

and we have $\sum_i^{a1,a2,b,c,d} \eta_i = 1$, and

$$\sum_i^{a1,a2,b,c,d} \phi_i \cdot \kappa_i = \lambda . \quad (\text{S19})$$

Appendix 1.5 Intermediate nodes

In a metabolic network, the metabolites between the carbon source and precursor pools are the intermediate nodes. As specified in Wang *et al.* (Wang et al., 2019), to optimize cell growth rate, the substrate of each intermediate node is nearly saturated, and thus

$$\kappa_i \approx \frac{r_{\text{protein}}}{r_{\text{carbon}}} \cdot \frac{k_i^{\text{cat}}}{n_{E_i}} . \quad (\text{S20})$$

The real cases could be more complicated because of other metabolic regulations. Recent quantitative studies (Bennett et al., 2009; Park et al., 2016) have shown that at least in *E. coli*, for

most of the substrate-enzyme pairs $[S_i] > K_i$, which implies $\kappa_i \approx \frac{r_{\text{protein}}}{r_{\text{carbon}}} \cdot \frac{k_i^{\text{cat}}}{n_{E_i}}$.

Appendix 2 Model and analysis

Appendix 2.1 Coarse-grained model

In the coarse-grained model shown in Fig. 1B, node *A* represents an arbitrary carbon source of Group A (Wang et al., 2019), which joins at the upper part of glycolysis. Nodes M1, M2, M3, M4, and M5 stand for G6P, PEP, acetyl-CoA, α -ketoglutarate, and oxaloacetate, respectively. In the analysis of carbon supply into precursor pools, we lump sum G6P/F6P as M1, GA3P/3PG/PEP as M2, and pyruvate/acetyl-CoA as M3 for approximation. For the biochemical reactions, each follows Eq. S5 with $b_i = 1$ except that $M1 \rightarrow 2M2$ and $M3 + M5 \rightarrow M4$. Basically,

there are 3 possible destinies of a Group A carbon source (e.g., glucose, see Appendix-fig. 1C-E): energy contributions in the fermentation and respiration pathways (Appendix-fig.1C-D), or biomass components accompanied by energy production in the biomass pathway (Appendix-fig. 1E).

By applying flux balance to the stoichiometric fluxes and combining with Eq. S8, we have:

$$\begin{cases} \Phi_A \cdot \xi_A = \Phi_1 \cdot \xi_1 + \Phi_{a1} \cdot \xi_{a1}, \\ 2\Phi_1 \cdot \xi_1 = \Phi_2 \cdot \xi_2 + \Phi_5 \cdot \xi_5 + \Phi_{a2} \cdot \xi_{a2}, \\ \Phi_2 \cdot \xi_2 = \Phi_3 \cdot \xi_3 + \Phi_6 \cdot \xi_6 + \Phi_b \cdot \xi_b, \\ \Phi_5 \cdot \xi_5 + \Phi_4 \cdot \xi_4 = \Phi_3 \cdot \xi_3 + \Phi_d \cdot \xi_d, \\ \Phi_3 \cdot \xi_3 = \Phi_4 \cdot \xi_4 + \Phi_c \cdot \xi_c. \end{cases} \quad (\text{S21})$$

Obviously, the stoichiometric fluxes of respiration J_r and fermentation J_f (Appendix-fig. 1C-D) are:

$$\begin{cases} J_r \equiv J_4 = \Phi_4 \cdot \xi_4, \\ J_f \equiv J_6 = \Phi_6 \cdot \xi_6. \end{cases} \quad (\text{S22})$$

We further assume that the carbon atoms are conserved from each entry point metabolite to the precursor pool, and then,

$$\Phi_i \cdot \xi_i \cdot N_{\text{EP}_i}^{\text{carbon}} = r_i \cdot J_{\text{BM}} \quad (i = a1, a2, b, c, d). \quad (\text{S23})$$

In terms of energy production for the relevant reactions, for convenience, we convert all the energy currencies into ATPs, namely, $\text{NADH} \rightarrow 2\text{ATP}$ (Neidhardt et al., 1990), $\text{NADPH} \rightarrow 2\text{ATP}$ (Neidhardt et al., 1990; Sauer et al., 2004), $\text{FADH}_2 \rightarrow 1\text{ATP}$ (Neidhardt et al., 1990). Then, we have

$$\beta_1 \cdot \Phi_1 \cdot \xi_1 + \beta_2 \cdot \Phi_2 \cdot \xi_2 + \beta_3 \cdot \Phi_3 \cdot \xi_3 + \beta_4 \cdot \Phi_4 \cdot \xi_4 + \beta_6 \cdot \Phi_6 \cdot \xi_6 + \beta_{a1} \cdot \Phi_{a1} \cdot \xi_{a1} = J_E, \quad (\text{S24})$$

where J_E represents the stoichiometric flux of ATPs, and β_i is the stoichiometric coefficient with $\beta_1 = 4$, $\beta_2 = 3$, $\beta_3 = 2$, $\beta_4 = 6$, $\beta_6 = 1$, and $\beta_{a1} = 4$ (Neidhardt et al., 1990; Sauer et al., 2004). Generally, the energy demand is proportional to the carbon flux infused into biomass production, thus,

$$J_E = r_E \cdot J_{\text{BM}}, \quad (\text{S25})$$

where r_E is the ratio and also a constant.

By applying the substitutions specified in Eqs. S9, S12, S14-S18, combined with Eqs. S4, S10, S21-S25, and the constraint of proteome resource allocation $\phi_R + \phi_C = \phi_{\text{max}}$, we have:

$$\begin{cases}
\phi_A \cdot \kappa_A = \phi_1 \cdot \kappa_1 + \phi_{a1} \cdot \kappa_{a1}, \\
2\phi_1 \cdot \kappa_1 = \phi_2 \cdot \kappa_2 + \phi_5 \cdot \kappa_5 + \phi_{a2} \cdot \kappa_{a2}, \\
\phi_2 \cdot \kappa_2 = \phi_3 \cdot \kappa_3 + \phi_6 \cdot \kappa_6 + \phi_b \cdot \kappa_b, \\
\phi_5 \cdot \kappa_5 + \phi_4 \cdot \kappa_4 = \phi_3 \cdot \kappa_3 + \phi_d \cdot \kappa_d, \\
\phi_3 \cdot \kappa_3 = \phi_4 \cdot \kappa_4 + \phi_c \cdot \kappa_c, \\
\phi_{a1} \cdot \kappa_{a1} = \eta_{a1} \cdot \lambda, \phi_{a2} \cdot \kappa_{a2} = \eta_{a2} \cdot \lambda, \phi_b \cdot \kappa_b = \eta_b \cdot \lambda, \phi_c \cdot \kappa_c = \eta_c \cdot \lambda, \phi_d \cdot \kappa_d = \eta_d \cdot \lambda, \\
\beta_1 \cdot \phi_1 \cdot \kappa_1 + \beta_2 \cdot \phi_2 \cdot \kappa_2 + \beta_3 \cdot \phi_3 \cdot \kappa_3 + \beta_4 \cdot \phi_4 \cdot \kappa_4 + \beta_6 \cdot \phi_6 \cdot \kappa_6 + \beta_{a1} \cdot \phi_{a1} \cdot \kappa_{a1} = J_E^{(N)}, \\
J_E^{(N)} = \eta_E \cdot \lambda, \lambda = \phi_R \cdot \kappa_r, J_r^{(N)} = \phi_4 \cdot \kappa_4, J_f^{(N)} = \phi_6 \cdot \kappa_6, \\
\phi_R + \phi_A + \phi_1 + \phi_2 + \phi_3 + \phi_4 + \phi_5 + \phi_6 + \phi_{a1} + \phi_{a2} + \phi_b + \phi_c + \phi_d = \phi_{\max},
\end{cases} \quad (S26)$$

where $\eta_E = r_E \cdot \left[\sum_i r_i / N_{EP_i}^{\text{carbon}} \right]^{-1}$. Here, for each intermediate node, κ_i follows Eq. S20, which can be approximated as a constant. The substrate quality of the Group A carbon source κ_A varies with the identity and concentration of the Group A carbon source:

$$\kappa_A \equiv \frac{r_{\text{protein}}}{r_{\text{carbon}}} \cdot \frac{k_A^{\text{cat}}}{m_{E_A}} \cdot \frac{[A]}{[A] + K_A} \cdot m_0, \quad (S27)$$

which is determined externally by the culture condition. From Eq. S26, all ϕ_i can be expressed by $J_r^{(N)}$, $J_f^{(N)}$, and λ :

$$\begin{cases}
\phi_A = \left[J_r^{(N)} + J_f^{(N)} + (2\eta_{a1} + \eta_{a2} + \eta_b + 2\eta_c + \eta_d) \lambda \right] / (2 \cdot \kappa_A), \\
\phi_1 = \left[J_r^{(N)} + J_f^{(N)} + (\eta_{a2} + \eta_b + 2\eta_c + \eta_d) \lambda \right] / (2 \cdot \kappa_1), \\
\phi_2 = \left[J_r^{(N)} + J_f^{(N)} + (\eta_b + \eta_c) \lambda \right] / \kappa_2, \\
\phi_3 = (J_r^{(N)} + \eta_c \cdot \lambda) / \kappa_3, \phi_4 = J_r^{(N)} / \kappa_4, \\
\phi_5 = (\eta_c + \eta_d) \lambda / \kappa_5, \phi_6 = J_f^{(N)} / \kappa_6, \\
\phi_i = \eta_i \cdot \lambda / \kappa_i \quad (i = a1, a2, b, c, d).
\end{cases} \quad (S28)$$

By substituting Eq. S28 into Eq. S26, we have:

$$\begin{cases}
J_r^{(E)} + J_f^{(E)} = \varphi \cdot \lambda, \\
\frac{J_r^{(E)}}{\varepsilon_r} + \frac{J_f^{(E)}}{\varepsilon_f} = \phi_{\max} - \psi \cdot \lambda.
\end{cases} \quad (S29)$$

Here, $J_r^{(E)}$ and $J_f^{(E)}$ stand for the normalized energy fluxes of respiration and fermentation, with

$$\begin{cases} J_r^{(E)} = (\beta_1/2 + \beta_2 + \beta_3 + \beta_4) \cdot J_r^{(N)}, \\ J_f^{(E)} = (\beta_1/2 + \beta_2 + \beta_6) \cdot J_f^{(N)}. \end{cases} \quad (S30)$$

The coefficients ε_r and ε_f represent the proteome energy efficiencies of the respiration and fermentation pathways (Appendix-fig. 1C-D), respectively, with

$$\begin{cases} \varepsilon_r = \frac{\beta_1/2 + \beta_2 + \beta_3 + \beta_4}{1/(2\kappa_A) + 1/(2\kappa_1) + 1/\kappa_2 + 1/\kappa_3 + 1/\kappa_4}, \\ \varepsilon_f = \frac{\beta_1/2 + \beta_2 + \beta_6}{1/(2\kappa_A) + 1/(2\kappa_1) + 1/\kappa_2 + 1/\kappa_6}. \end{cases} \quad (S31)$$

ψ^{-1} is the proteome efficiency of biomass pathway (Appendix-fig. 1E), with

$$\psi = \frac{1}{\kappa_t} + \frac{1 + \eta_{a1} + \eta_c}{2\kappa_A} + \frac{\eta_{a2} + \eta_b + 2\eta_c + \eta_d}{2\kappa_1} + \frac{\eta_b + \eta_c}{\kappa_2} + \frac{\eta_c}{\kappa_3} + \frac{\eta_c + \eta_d}{\kappa_5} + \sum_i^{a1,a2,b,c,d} \frac{\eta_i}{\kappa_i}. \quad (S32)$$

φ is the energy demand coefficient (a constant), with

$$\varphi \equiv \eta_E - \beta_1 \cdot (\eta_{a2} + \eta_b + 2\eta_c + \eta_d)/2 - \beta_2 \cdot (\eta_b + \eta_c) - \beta_3 \cdot \eta_c - \beta_{a1} \cdot \eta_{a1}, \quad (S33)$$

and $\varphi \cdot \lambda$ stands for the normalized energy demand other than the accompanying energy production from the biomass pathway.

Appendix 2.2 The reason for overflow metabolism

Microbes optimize their growth rate to survive in the evolutionary process (Vander Heiden et al., 2009). Basically, this also applies to tumor cells, which proliferate rapidly ignoring signals of growth restriction (Vander Heiden et al., 2009). To optimize cell growth, we first consider the best strategy for a single cell. The coarse-grained model is summarized in Eq. S26 and further simplified into Eq. S29. Here, ε_r , ε_f and ψ are functions of κ_A (see Eqs. S31, S32), so we also denote them as $\varepsilon_r(\kappa_A)$, $\varepsilon_f(\kappa_A)$, $\psi(\kappa_A)$. Apparently, the fluxes of both respiration and fermentation take non-negative values, i.e., $J_r^{(E)}, J_f^{(E)} \geq 0$, and all the coefficients are positive: $\varepsilon_r(\kappa_A), \varepsilon_f(\kappa_A), \psi(\kappa_A), \varphi > 0$.

Thus, if $\varepsilon_r > \varepsilon_f$, then $(\psi + \varphi/\varepsilon_r) \cdot \lambda = \phi_{\max} - J_f^{(E)}(1/\varepsilon_f - 1/\varepsilon_r) \leq \phi_{\max}$. Obviously, the optimal solution is:

$$\begin{cases} J_f^{(E)} = 0, \\ J_r^{(E)} = \varphi \cdot \lambda. \end{cases} \quad \varepsilon_r > \varepsilon_f. \quad (S34)$$

Similarly, if $\varepsilon_f > \varepsilon_r$, then the optimal solution is:

$$\begin{cases} J_f^{(E)} = \varphi \cdot \lambda, \\ J_r^{(E)} = 0. \end{cases} \quad \varepsilon_r < \varepsilon_f. \quad (\text{S35})$$

In both cases, the growth rate λ takes the maximum value for a given nutrient condition (i.e., given κ_A):

$$\lambda = \begin{cases} \lambda_r \equiv \frac{\phi_{\max}}{\varphi/\varepsilon_r(\kappa_A) + \psi(\kappa_A)} & \varepsilon_r(\kappa_A) > \varepsilon_f(\kappa_A), \\ \lambda_f \equiv \frac{\phi_{\max}}{\varphi/\varepsilon_f(\kappa_A) + \psi(\kappa_A)} & \varepsilon_r(\kappa_A) < \varepsilon_f(\kappa_A). \end{cases} \quad (\text{S36})$$

So, why do microbes use the wasteful fermentation pathway when the growth rate is large under aerobic conditions? An intuitive speculation is that the fermentation pathway is more efficient in terms of the proteome energy efficiency, i.e., $\varepsilon_f > \varepsilon_r$. If so, then why do microbes still use the normal respiration pathway when the growth rate is small? The answer lies in that both $\varepsilon_r(\kappa_A)$ and $\varepsilon_f(\kappa_A)$ are not constants, but are dependent on nutrient conditions. In Eq. S31, when κ_A is small, just consider the extreme case of $\kappa_A \rightarrow 0$, and then

$$\begin{cases} \varepsilon_r(\kappa_A \rightarrow 0) \approx [\beta_1 + 2(\beta_2 + \beta_3 + \beta_4)] \cdot \kappa_A, \\ \varepsilon_f(\kappa_A \rightarrow 0) \approx [\beta_1 + 2(\beta_2 + \beta_6)] \cdot \kappa_A. \end{cases} \quad (\text{S37})$$

Since $\beta_3 + \beta_4 \gg \beta_6$, clearly,

$$\varepsilon_r(\kappa_A \rightarrow 0) > \varepsilon_f(\kappa_A \rightarrow 0). \quad (\text{S38})$$

Combined with Eq. S36, thus cells would certainly use the respiration pathway when the growth rate is very small. Meanwhile, suppose that κ_A^{\max} is the maximum value of κ_A available across different Group A carbon sources, and if there exists a κ_A (with $\kappa_A \leq \kappa_A^{\max}$) satisfying $\varepsilon_r(\kappa_A) < \varepsilon_f(\kappa_A)$, specifically,

$$\frac{\beta_3 + \beta_4 - \beta_6}{2\kappa_A} < \left(\frac{\beta_1}{2} + \beta_2 + \beta_6 \right) \left(\frac{1}{2\kappa_1} + \frac{1}{\kappa_2} + \frac{1}{\kappa_3} + \frac{1}{\kappa_4} \right) - \left(\frac{\beta_1}{2} + \beta_2 + \beta_3 + \beta_4 \right) \cdot \left(\frac{1}{2\kappa_1} + \frac{1}{\kappa_2} + \frac{1}{\kappa_6} \right), \quad (\text{S39})$$

then $\Delta(\kappa_A) \equiv \varepsilon_f(\kappa_A)/\varepsilon_r(\kappa_A)$ is a monotonously increasing function of κ_A . Thus,

$$\varepsilon_r(\kappa_A^{\max}) < \varepsilon_f(\kappa_A^{\max}), \quad (\text{S40})$$

and cells would use the fermentation pathway when the growth rate is large.

In practice, experimental studies (Basan et al., 2015) in *E. coli* have reported that the proteome energy efficiency in fermentation is higher than that in respiration when the Group A carbon source is lactose at saturated concentration (Molenaar et al., 2009), i.e., $\varepsilon_r(\kappa_{\text{lactose}}^{(\text{ST})}) < \varepsilon_f(\kappa_{\text{lactose}}^{(\text{ST})})$. Here, $\kappa_{\text{lactose}}^{(\text{ST})}$ represents the substrate quality of lactose and the superscript “(ST)” signifies saturated concentration. In fact, *E. coli* grows much faster in G6p than lactose (Basan et al., 2015), thus, $\kappa_A^{\text{max}} > \kappa_{\text{lactose}}^{(\text{ST})}$. The above example verifies that Eq. S40 holds for *E. coli*. In fact, more recent studies (Chen and Nielsen, 2019) supported that Eq. S40 holds generically for many microbial species. From the theoretical side, we can verify Eq. S39 and thus Eq. S40 using Eq. S20 combined with the in vivo/in vitro biochemical parameters obtained from experimental data (see Appendix-tables 1-2). For example, it is easy to check that $\varepsilon_r(\kappa_{\text{glucose}}^{(\text{ST})}) < \varepsilon_f(\kappa_{\text{glucose}}^{(\text{ST})})$ with this method (see Appendix 8.2), which also confirms the validity of Eqs. S39-S40.

Now that Eqs. S38-S40 are all valid, then there exists a critical value of κ_A (denoted as $\kappa_A^{(\text{C})}$) satisfying $\Delta(\kappa_A^{(\text{C})}) = 1$. Thus,

$$\begin{cases} \varepsilon_f(\kappa_A) > \varepsilon_r(\kappa_A), & \kappa_A > \kappa_A^{(\text{C})}; \\ \varepsilon_f(\kappa_A) = \varepsilon_r(\kappa_A), & \kappa_A = \kappa_A^{(\text{C})}; \\ \varepsilon_f(\kappa_A) < \varepsilon_r(\kappa_A), & \kappa_A < \kappa_A^{(\text{C})}. \end{cases} \quad (\text{S41})$$

Combined with Eq. S31, we have:

$$\kappa_A^{(\text{C})} = \frac{\beta_3 + \beta_4 - \beta_6}{(\beta_1/2 + \beta_2 + \beta_6)(1/\kappa_1 + 2/\kappa_2 + 2/\kappa_3 + 2/\kappa_4) - (\beta_1/2 + \beta_2 + \beta_3 + \beta_4)(1/\kappa_1 + 2/\kappa_2 + 2/\kappa_6)}. \quad (\text{S42})$$

By substituting Eq. S42 into Eqs. S31, S32 and S36, we obtain the expressions for $\varepsilon_r(\kappa_A^{(\text{C})})$, $\varepsilon_f(\kappa_A^{(\text{C})})$ and the critical growth rate at the transition point (i.e., $\lambda_c \equiv \lambda(\kappa_A^{(\text{C})})$):

$$\begin{cases} \varepsilon_r(\kappa_A^{(\text{C})}) = \varepsilon_f(\kappa_A^{(\text{C})}) = \frac{\beta_3 + \beta_4 - \beta_6}{1/\kappa_3 + 1/\kappa_4 - 1/\kappa_6}, \\ \lambda_c = \frac{\phi_{\text{max}}}{\varphi/\varepsilon_{r/f}(\kappa_A^{(\text{C})}) + \psi(\kappa_A^{(\text{C})})}, \end{cases} \quad (\text{S43})$$

where $\varepsilon_{r/f}$ represents either ε_r or ε_f . In Fig. 1E, we show the dependencies of $\varepsilon_r(\kappa_A)$, $\varepsilon_f(\kappa_A)$ and $\lambda(\kappa_A)$ on κ_A in a 3-dimensional form, as κ_A changes.

Appendix 2.3 The relation between respiration/fermentation fluxes and growth rate

We proceed to study the relation between the respiration/fermentation flux and the cell growth rate. From Eqs. S16 and S30, we see that the stoichiometric fluxes J_r , J_f , the normalized fluxes $J_r^{(N)}$, $J_f^{(N)}$ and the normalized energy fluxes $J_r^{(E)}$, $J_f^{(E)}$ are all interconvertible. For convenience, we first analyze the relations between $J_r^{(E)}$, $J_f^{(E)}$ and λ under growth rate optimization. In fact, all these terms are merely functions of κ_A (see Eqs. S34-S36), which is determined by the nutrient condition (Eq. S27).

In the homogeneous case, i.e., all microbes share identical biochemical parameters, as $\lambda(\kappa_A)$ increases with κ_A , $J_f^{(E)}$ show up abruptly and $J_r^{(E)}$ vanish simultaneously as κ_A right exceeds $\kappa_A^{(C)}$ (Fig. 1E, see also Eqs. S34-S35, S41). Combining Eqs. S34-S36 and S43, we have:

$$\begin{cases} J_f^{(E)} = \varphi \cdot \lambda \cdot \theta(\lambda - \lambda_c), \\ J_r^{(E)} = \varphi \cdot \lambda \cdot [1 - \theta(\lambda - \lambda_c)], \end{cases} \quad (\text{S44})$$

where “ θ ” stands for the Heaviside step function. Defining $\lambda_{\max} = \lambda(\kappa_A^{\max})$, and then, $[0, \lambda_{\max}]$ is the relevant range of the x axis. In fact, the digital responses in Eq. S44 are consistent with the numerical simulation results in Molenaar *et al.* (Molenaar *et al.*, 2009). However, these results are incompatible with the threshold-analog response in the standard picture of overflow metabolism (Basan *et al.*, 2015; Holms, 1996).

In practice, the values of k_i^{cat} can be greatly influenced by the concentrations of potassium and phosphate (García-Contreras *et al.*, 2012), which vary from cell to cell. Then, there is a distribution of the values for k_i^{cat} among the cell populations, commonly we call it extrinsic noise (Elowitz *et al.*, 2002). For convenience, we assume that each k_i^{cat} (and thus κ_i) follows a Gaussian distribution with the coefficient of variation (CV) taken as 25%. Then, the distribution of λ_c can be approximated by a Gaussian distribution (see Appendix 7.1):

$$\lambda_c \sim \mathcal{N}(\mu_{\lambda_c}, \sigma_{\lambda_c}^2), \quad (\text{S45})$$

where μ_{λ_c} and σ_{λ_c} stand for the mean and standard deviation of λ_c , with the CV $\sigma_{\lambda_c}/\mu_{\lambda_c}$ calculated to be 12% (see Appendix 8.2 for details). Note that λ is κ_A dependent, while λ_c is independent of κ_A . Thus, given the growth rate of microbes in a culturing medium (e.g., in a chemostat), the normalized energy fluxes are:

$$\begin{cases} J_f^{(E)}(\lambda) = \frac{1}{2} \varphi \cdot \lambda \cdot \left[\operatorname{erf} \left(\frac{\lambda - \mu_{\lambda_c}}{\sqrt{2} \sigma_{\lambda_c}} \right) + 1 \right], \\ J_r^{(E)}(\lambda) = \frac{1}{2} \varphi \cdot \lambda \cdot \left[1 - \operatorname{erf} \left(\frac{\lambda - \mu_{\lambda_c}}{\sqrt{2} \sigma_{\lambda_c}} \right) \right], \end{cases} \quad (\text{S46})$$

where “erf” represents the error function. In practice, given a culturing medium, there is also a probability distribution for the growth rate (Appendix-fig. 2B, see also Eq. S157). For approximation, in plotting the flux-growth rate relations, we use the deterministic (noise-free) value of the growth rate as the proxy. To compare with experiments, basically, we are comparing the normalized fluxes $J_r^{(N)}$, $J_f^{(N)}$ (see Appendix 8.1 for details). Combining Eqs. S30 and S46, we get:

$$\begin{cases} J_f^{(N)}(\lambda) = \frac{\varphi}{\beta_1 + 2(\beta_2 + \beta_6)} \cdot \lambda \cdot \left[\operatorname{erf} \left(\frac{\lambda - \mu_{\lambda_c}}{\sqrt{2} \sigma_{\lambda_c}} \right) + 1 \right], \\ J_r^{(N)}(\lambda) = \frac{\varphi}{\beta_1 + 2(\beta_2 + \beta_3 + \beta_4)} \cdot \lambda \cdot \left[1 - \operatorname{erf} \left(\frac{\lambda - \mu_{\lambda_c}}{\sqrt{2} \sigma_{\lambda_c}} \right) \right]. \end{cases} \quad (\text{S47})$$

In Fig. 1C-D, we see that Eq. S47 quantitatively illustrates the experimental data (Basan et al., 2015), where the model parameters were obtained using the biochemical data for the catalytic enzymes (see Appendix-table 1 for details).

Appendix 3 Model perturbations

Appendix 3.1 Overexpression of useless proteins

Here we consider the case of overexpression of the protein encoded by LacZ gene in *E. coli*. Effectively, this limits the proteome by altering ϕ_{\max} :

$$\phi_{\max} \xrightarrow{\text{LacZ overexpression}} \phi_{\max} - \phi_Z, \quad (\text{S48})$$

where ϕ_Z stands for the fraction of useless proteins, which is controllable in experiments. Then, the growth rate changes into a bivariate function of κ_A and ϕ_Z :

$$\lambda(\kappa_A, \phi_Z) = \begin{cases} \frac{\phi_{\max} - \phi_Z}{\varphi / \varepsilon_r(\kappa_A) + \psi(\kappa_A)} & \varepsilon_r(\kappa_A) > \varepsilon_f(\kappa_A), \\ \frac{\phi_{\max} - \phi_Z}{\varphi / \varepsilon_f(\kappa_A) + \psi(\kappa_A)} & \varepsilon_r(\kappa_A) < \varepsilon_f(\kappa_A), \end{cases} \quad (\text{S49})$$

and thus,

$$\lambda(\kappa_A, \phi_Z) = \lambda(\kappa_A, 0)(1 - \phi_Z/\phi_{\max}). \quad (\text{S50})$$

Obviously, $\kappa_A^{(c)}$ is still a constant (following Eq. S42), while $\lambda_c(\phi_Z) \equiv \lambda(\kappa_A^{(c)}, \phi_Z)$ and $\lambda_{\max}(\phi_Z) \equiv \lambda(\kappa_A^{\max}, \phi_Z)$ become functions of ϕ_Z :

$$\begin{cases} \lambda_c(\phi_Z) = \lambda_c(0)(1 - \phi_Z/\phi_{\max}), \\ \lambda_{\max}(\phi_Z) = \lambda_{\max}(0)(1 - \phi_Z/\phi_{\max}). \end{cases} \quad (\text{S51})$$

In the homogeneous case, $J_f^{(E)}$ and $J_r^{(E)}$ follow:

$$\begin{cases} J_f^{(E)}(\kappa_A, \phi_Z) = \varphi \cdot \lambda(\kappa_A, \phi_Z) \cdot \theta(\lambda(\kappa_A, \phi_Z) - \lambda_c(\phi_Z)), \\ J_r^{(E)}(\kappa_A, \phi_Z) = \varphi \cdot \lambda(\kappa_A, \phi_Z) \cdot [1 - \theta(\lambda(\kappa_A, \phi_Z) - \lambda_c(\phi_Z))]. \end{cases} \quad (\text{S52})$$

Combined with Eqs. S50-S51, we have:

$$\begin{cases} J_f^{(E)}(\kappa_A, \phi_Z) = \varphi \cdot \lambda(\kappa_A, \phi_Z) \cdot \theta(\lambda(\kappa_A, 0) - \lambda_c(0)), \\ J_r^{(E)}(\kappa_A, \phi_Z) = \varphi \cdot \lambda(\kappa_A, \phi_Z) \cdot [1 - \theta(\lambda(\kappa_A, 0) - \lambda_c(0))]. \end{cases} \quad (\text{S53})$$

To compare with experiments, we assume that each k_i^{cat} and κ_i follow the extrinsic noise with a CV of 25% specified in Appendix 2.3, and neglect the noise on ϕ_Z and ϕ_{\max} . Combining Eqs. S45 and S51, we see that $\lambda_c(\phi_Z)$ approximately follows a Gaussian distribution:

$$\lambda_c(\phi_Z) \sim \mathcal{N}(\mu_{\lambda_c}(\phi_Z), \sigma_{\lambda_c}(\phi_Z)^2), \quad (\text{S54})$$

where $\mu_{\lambda_c}(\phi_Z)$ and $\sigma_{\lambda_c}(\phi_Z)$ represent the mean and standard deviation of $\lambda_c(\phi_Z)$, with

$$\begin{cases} \mu_{\lambda_c}(\phi_Z) = \mu_{\lambda_c}(0)(1 - \phi_Z/\phi_{\max}), \\ \sigma_{\lambda_c}(\phi_Z) = \sigma_{\lambda_c}(0)(1 - \phi_Z/\phi_{\max}). \end{cases} \quad (\text{S55})$$

Here, $\mu_{\lambda_c}(0)$, $\sigma_{\lambda_c}(0)$, $\lambda_c(0)$, $\lambda_{\max}(0)$ and $\lambda(\kappa_A, 0)$ represent the parameters or variables free from LacZ perturbation, just as those in Appendix 2.3. Since the noise on the multiplier term (i.e., $1 - \phi_Z/\phi_{\max}$) is negligible, the CV of $\lambda_c(\phi_Z)$ (i.e., $\sigma_{\lambda_c}(\phi_Z)/\mu_{\lambda_c}(\phi_Z)$) is unaffected by ϕ_Z . By combining Eqs. S46 and S48, we obtain the relations between the normalized energy fluxes and growth rate:

$$\begin{cases} J_f^{(E)}(\lambda(\kappa_A, \phi_Z), \phi_Z) = \frac{1}{2} \varphi \cdot \lambda(\kappa_A, \phi_Z) \cdot \left[\operatorname{erf} \left(\frac{\lambda(\kappa_A, \phi_Z) - \mu_{\lambda_c}(\phi_Z)}{\sqrt{2} \sigma_{\lambda_c}(\phi_Z)} \right) + 1 \right], \\ J_r^{(E)}(\lambda(\kappa_A, \phi_Z), \phi_Z) = \frac{1}{2} \varphi \cdot \lambda(\kappa_A, \phi_Z) \cdot \left[1 - \operatorname{erf} \left(\frac{\lambda(\kappa_A, \phi_Z) - \mu_{\lambda_c}(\phi_Z)}{\sqrt{2} \sigma_{\lambda_c}(\phi_Z)} \right) \right], \end{cases} \quad (\text{S56})$$

where $\lambda(\kappa_A, \phi_Z)$, $\mu_{\lambda_c}(\phi_Z)$ and $\sigma_{\lambda_c}(\phi_Z)$ follow Eqs. S50 and S55 accordingly. For a given value of ϕ_Z , i.e., ϕ_Z is fixed, then, $\lambda(\kappa_A, \phi_Z)$ changes monotonously with κ_A . Combining Eqs. S55-S56 and S30, we have the relation between the normalized fluxes $J_r^{(N)}$, $J_f^{(N)}$ and growth rate (here ϕ_Z is a parameter):

$$\begin{cases} J_f^{(N)}(\lambda, \phi_Z) = \frac{\varphi}{\beta_1 + 2(\beta_2 + \beta_6)} \cdot \lambda \cdot \left[\operatorname{erf} \left(\frac{\lambda - \mu_{\lambda_c}(0)(1 - \phi_Z/\phi_{\max})}{\sqrt{2} \sigma_{\lambda_c}(0)(1 - \phi_Z/\phi_{\max})} \right) + 1 \right], \\ J_r^{(N)}(\lambda, \phi_Z) = \frac{\varphi}{\beta_1 + 2(\beta_2 + \beta_3 + \beta_4)} \cdot \lambda \cdot \left[1 - \operatorname{erf} \left(\frac{\lambda - \mu_{\lambda_c}(0)(1 - \phi_Z/\phi_{\max})}{\sqrt{2} \sigma_{\lambda_c}(0)(1 - \phi_Z/\phi_{\max})} \right) \right]. \end{cases} \quad (\text{S57})$$

In Fig. 2C. we show that the model predictions (Eq. S57) quantitatively agree with the experiments (Basan et al., 2015).

Meanwhile, we can also perturb the growth rate by tuning ϕ_Z in a stable culturing environment with fixed concentration of a Group A carbon source (i.e., given $[A]$). In fact, for this case there is a distribution of κ_A values due to the extrinsic noise in k_A^{cat} , yet this distribution is fixed. For convenience of description, we still referred to it as fixed κ_A . Then, combining Eqs. S30, S50, S55 and S56, we get:

$$\begin{cases} J_f^{(N)}(\lambda, \phi_Z) = \frac{\varphi}{\beta_1 + 2(\beta_2 + \beta_6)} \cdot \left[\operatorname{erf} \left(\frac{\lambda(\kappa_A, 0) - \mu_{\lambda_c}(0)}{\sqrt{2} \sigma_{\lambda_c}(0)} \right) + 1 \right] \cdot \lambda, \\ J_r^{(N)}(\lambda, \phi_Z) = \frac{\varphi}{\beta_1 + 2(\beta_2 + \beta_3 + \beta_4)} \cdot \left[1 - \operatorname{erf} \left(\frac{\lambda(\kappa_A, 0) - \mu_{\lambda_c}(0)}{\sqrt{2} \sigma_{\lambda_c}(0)} \right) \right] \cdot \lambda. \end{cases} \quad (\text{S58})$$

Here, $\lambda(\kappa_A, 0)$ remains unaltered as κ_A is fixed. Therefore, in this case, $J_f^{(N)}$ and $J_r^{(N)}$ are proportional to λ , where the slopes are both functions of κ_A . More specifically, the slope of $J_f^{(N)}$ is a monotonically increasing function of κ_A , while that of $J_r^{(N)}$ is a monotonically decreasing function of κ_A . In Fig. 2B, we see that the model predictions (Eq. S58) agree quantitatively with the experiments (Basan et al., 2015).

In fact, the growth rate can be altered by tuning ϕ_Z and κ_A simultaneously. Then, the relations among the energy fluxes, growth rate and ϕ_Z still follow Eq. S57 (here ϕ_Z is a variable). In a 3-D representation, these relations correspond to a surface. In Fig. 2A, we show that the model predictions (Eq. S57) match well with the experimental data (Basan et al., 2015).

Appendix 3.2 Energy dissipation

In practice, energy dissipation breaks the proportional relationship between energy demand and biomass production. Thus, Eq. S25 changes to:

$$J_E = r_E \cdot J_{BM} + w \cdot \frac{M_{\text{carbon}}}{m_0}, \quad (\text{S59})$$

where w represents the dissipation coefficient. In fact, maintenance energy contributes to energy dissipation, and we define the maintenance energy coefficient as w_0 . In bacteria, the impact of w_0 is often negligible, particularly for all the analysis in the sections above. While in tumor cell, w_0 plays a much more significant role.

The introduction of energy dissipation leads to a modification to Eq. S26: combining Eq. S59 and Eq. S16, we have:

$$J_E^{(N)} = \eta_E \cdot \lambda + w. \quad (\text{S60})$$

Then, Eq. S29 changes to:

$$\begin{cases} J_r^{(E)} + J_f^{(E)} = \phi \cdot \lambda + w, \\ \frac{J_r^{(E)}}{\varepsilon_r} + \frac{J_f^{(E)}}{\varepsilon_f} = \phi_{\max} - \psi \cdot \lambda. \end{cases} \quad (\text{S61})$$

Consequently, if $\varepsilon_r > \varepsilon_f$, the best strategy for the cell is:

$$\begin{cases} J_f^{(E)} = 0, \\ J_r^{(E)} = \phi \cdot \lambda + w, \end{cases} \quad \varepsilon_r > \varepsilon_f, \quad (\text{S62})$$

and if $\varepsilon_f > \varepsilon_r$, the best strategy is:

$$\begin{cases} J_f^{(E)} = \phi \cdot \lambda + w, \\ J_r^{(E)} = 0. \end{cases} \quad \varepsilon_r < \varepsilon_f. \quad (\text{S63})$$

Then, the growth rate turns into a bivariate function of both κ_A and w :

$$\lambda(\kappa_A, w) = \begin{cases} \frac{\phi_{\max} - w/\varepsilon_r(\kappa_A)}{\varphi/\varepsilon_r(\kappa_A) + \psi(\kappa_A)} & \varepsilon_r(\kappa_A) > \varepsilon_f(\kappa_A), \\ \frac{\phi_{\max} - w/\varepsilon_f(\kappa_A)}{\varphi/\varepsilon_f(\kappa_A) + \psi(\kappa_A)} & \varepsilon_r(\kappa_A) < \varepsilon_f(\kappa_A). \end{cases} \quad (\text{S64})$$

Clearly, $\kappa_A^{(c)}$ is still a constant, while $\lambda_c(w) \equiv \lambda(\kappa_A^{(c)}, w)$ and $\lambda_{\max}(w) \equiv \lambda(\kappa_A^{\max}, w)$ changes into functions of w :

$$\begin{cases} \lambda_c(w) = \lambda_c(0) \left\{ 1 - w / \left[\varepsilon_{r/f}(\kappa_A^{(c)}) \phi_{\max} \right] \right\}, \\ \lambda_{\max}(w) = \lambda_{\max}(0) \left\{ 1 - w / \left[\varepsilon_f(\kappa_A^{\max}) \phi_{\max} \right] \right\}. \end{cases} \quad (\text{S65})$$

For a cell population, in the homogeneous case, $J_f^{(E)}$ and $J_r^{(E)}$ follow:

$$\begin{cases} J_f^{(E)}(\kappa_A, w) = [\varphi \cdot \lambda(\kappa_A, w) + w] \cdot \theta(\lambda(\kappa_A, w) - \lambda_c(w)), \\ J_r^{(E)}(\kappa_A, w) = [\varphi \cdot \lambda(\kappa_A, w) + w] \cdot [1 - \theta(\lambda(\kappa_A, w) - \lambda_c(w))]. \end{cases} \quad (\text{S66})$$

To compare with experiments, we assume the same extent of extrinsic noise in k_i^{cat} (and thus κ_i) as that specified in Appendix 2.3. Combining Eqs. S45 and S65, then, $\lambda_c(w)$ approximately follows a Gaussian distribution:

$$\lambda_c(w) \sim \mathcal{N}(\mu_{\lambda_c}(w), \sigma_{\lambda_c}(w)^2), \quad (\text{S67})$$

where $\mu_{\lambda_c}(w)$ and $\sigma_{\lambda_c}(w)$ represent the mean and standard deviation of $\lambda_c(w)$, and

$$\begin{cases} \mu_{\lambda_c}(w) = \mu_{\lambda_c}(0) \left\{ 1 - w / \left[\varepsilon_{r/f}(\kappa_A^{(c)}) \phi_{\max} \right] \right\}, \\ \sigma_{\lambda_c}(w) \approx \sigma_{\lambda_c}(0) \left\{ 1 - w / \left[\varepsilon_{r/f}(\kappa_A^{(c)}) \phi_{\max} \right] \right\}. \end{cases} \quad (\text{S68})$$

Here, $\mu_{\lambda_c}(0)$, $\sigma_{\lambda_c}(0)$, $\lambda_c(0)$, $\lambda_{\max}(0)$ and $\lambda(\kappa_A, 0)$ represent the parameters or variables free from energy dissipation. In fact, there is a distribution of values for $\varepsilon_{r/f}(\kappa_A^{(c)})$. For approximation, we use the deterministic value of $\varepsilon_{r/f}(\kappa_A^{(c)})$ in Eq. S68, and then the CV of $\lambda_c(w)$ is roughly unperturbed by w . Combining Eqs. S46, S66 and S67, we have:

$$\begin{cases} J_f^{(E)}(\lambda(\kappa_A, w), w) = \frac{1}{2}(\varphi \cdot \lambda(\kappa_A, w) + w) \cdot \left[\operatorname{erf}\left(\frac{\lambda(\kappa_A, w) - \mu_{\lambda_c}(w)}{\sqrt{2}\sigma_{\lambda_c}(w)}\right) + 1 \right], \\ J_r^{(E)}(\lambda(\kappa_A, w), w) = \frac{1}{2}(\varphi \cdot \lambda(\kappa_A, w) + w) \cdot \left[1 - \operatorname{erf}\left(\frac{\lambda(\kappa_A, w) - \mu_{\lambda_c}(w)}{\sqrt{2}\sigma_{\lambda_c}(w)}\right) \right]. \end{cases} \quad (\text{S69})$$

Since the dissipation coefficient w is tunable in experiments, for a given value of w , $\lambda(\kappa_A, w)$ changes monotonously with κ_A . Combining Eqs. S68-S69 and S30, we have (here w is a parameter):

$$\begin{cases} J_f^{(N)}(\lambda, w) = \frac{\varphi \cdot \lambda + w}{\beta_1 + 2(\beta_2 + \beta_6)} \cdot \left[\operatorname{erf}\left(\frac{\lambda - \mu_{\lambda_c}(0) \left\{1 - w / \left[\varepsilon_{r/f}(\kappa_A^{(C)}) \phi_{\max} \right] \right\}}{\sqrt{2}\sigma_{\lambda_c}(0) \left\{1 - w / \left[\varepsilon_{r/f}(\kappa_A^{(C)}) \phi_{\max} \right] \right\}}\right) + 1 \right], \\ J_r^{(N)}(\lambda, w) = \frac{\varphi \cdot \lambda + w}{\beta_1 + 2(\beta_2 + \beta_3 + \beta_4)} \cdot \left[1 - \operatorname{erf}\left(\frac{\lambda - \mu_{\lambda_c}(0) \left\{1 - w / \left[\varepsilon_{r/f}(\kappa_A^{(C)}) \phi_{\max} \right] \right\}}{\sqrt{2}\sigma_{\lambda_c}(0) \left\{1 - w / \left[\varepsilon_{r/f}(\kappa_A^{(C)}) \phi_{\max} \right] \right\}}\right) \right]. \end{cases} \quad (\text{S70})$$

The comparison between model predictions (Eq. S70) and experimental results (Basan et al., 2015) is shown in Fig. 3B, which agrees quantitatively. Meanwhile, the growth rate can also be perturbed by changing κ_A and w simultaneously. Then, the relations among the energy fluxes, growth rate and w follow Eq. S70 (here w is a variable). In a 3D representation, these relations correspond to a surface. As shown in Fig. 3A, the model predictions (Eq. S70) agree quantitatively with the experimental results (Basan et al., 2015).

Appendix 3.3 Translation inhibition

In *E. coli*, the translation rate can be modified by adding different concentrations of translation inhibitors, e.g., chloramphenicol (Cm). The net effect of this perturbation is represented as:

$$\kappa_t \xrightarrow{\text{Translation inhibition}} \kappa_t / (1 + \iota), \quad (\text{S71})$$

where ι stands for the inhibition coefficient with $\iota > 0$, and $(1 + \iota)^{-1}$ represents the translation efficiency. Thus, Eq. S32 changes to:

$$\psi(\kappa_A, \iota) = \frac{\iota + 1}{\kappa_t} + \frac{1 + \eta_{a1} + \eta_c}{2\kappa_A} + \frac{\eta_{a2} + \eta_b + 2\eta_c + \eta_d}{2\kappa_1} + \frac{\eta_b + \eta_c}{\kappa_2} + \frac{\eta_c}{\kappa_3} + \frac{\eta_c + \eta_d}{\kappa_5} + \sum_i^{a1, a2, b, c, d} \frac{\eta_i}{\kappa_i}. \quad (\text{S72})$$

First, we consider the case of neglecting the maintenance energy, i.e., $w_0 = 0$. Then, the growth rate takes the following form:

$$\lambda(\kappa_A, \iota) = \begin{cases} \frac{\phi_{\max}}{\varphi/\varepsilon_r(\kappa_A) + \psi(\kappa_A, \iota)} & \varepsilon_r(\kappa_A) > \varepsilon_f(\kappa_A), \\ \frac{\phi_{\max}}{\varphi/\varepsilon_f(\kappa_A) + \psi(\kappa_A, \iota)} & \varepsilon_r(\kappa_A) < \varepsilon_f(\kappa_A), \end{cases} \quad (\text{S73})$$

where $\lambda(\kappa_A, 0)$ and $\psi(\kappa_A, 0)$ represent the terms free from translation inhibition. Thus, $\lambda_c(\iota) \equiv \lambda(\kappa_A^{(c)}, \iota)$ and $\lambda_{\max}(\iota) \equiv \lambda(\kappa_A^{\max}, \iota)$ change into functions of ι :

$$\begin{cases} \lambda_c(\iota) = \lambda_c(0) \frac{\varphi/\varepsilon_{r/f}(\kappa_A^{(c)}) + \psi(\kappa_A^{(c)}, 0)}{\varphi/\varepsilon_{r/f}(\kappa_A^{(c)}) + \psi(\kappa_A^{(c)}, \iota)}, \\ \lambda_{\max}(\iota) = \lambda_{\max}(0) \frac{\varphi/\varepsilon_f(\kappa_A^{\max}) + \psi(\kappa_A^{\max}, 0)}{\varphi/\varepsilon_f(\kappa_A^{\max}) + \psi(\kappa_A^{\max}, \iota)}. \end{cases} \quad (\text{S74})$$

In the homogeneous case, $J_f^{(E)}$ and $J_r^{(E)}$ follow:

$$\begin{cases} J_f^{(E)}(\kappa_A, \iota) = \varphi \cdot \lambda(\kappa_A, \iota) \cdot \theta(\lambda(\kappa_A, \iota) - \lambda_c(\iota)), \\ J_r^{(E)}(\kappa_A, \iota) = \varphi \cdot \lambda(\kappa_A, \iota) \cdot [1 - \theta(\lambda(\kappa_A, \iota) - \lambda_c(\iota))]. \end{cases} \quad (\text{S75})$$

To compare with experiments, we assume that there exists extrinsic noise in k_i^{cat} and κ_i as specified in Appendix 2.3. Combining Eqs. S45 and S74, $\lambda_c(\iota)$ can be approximated by a Gaussian distribution:

$$\lambda_c(\iota) \sim \mathcal{N}(\mu_{\lambda_c}(\iota), \sigma_{\lambda_c}(\iota)^2), \quad (\text{S76})$$

where $\mu_{\lambda_c}(\iota)$ and $\sigma_{\lambda_c}(\iota)$ represent the mean and standard deviation of $\lambda_c(\iota)$, with

$$\begin{cases} \mu_{\lambda_c}(\iota) = \mu_{\lambda_c}(0) \frac{\varphi/\varepsilon_{r/f}(\kappa_A^{(c)}) + \psi(\kappa_A^{(c)}, 0)}{\varphi/\varepsilon_{r/f}(\kappa_A^{(c)}) + \psi(\kappa_A^{(c)}, \iota)}, \\ \sigma_{\lambda_c}(\iota) \approx \sigma_{\lambda_c}(0) \frac{\varphi/\varepsilon_{r/f}(\kappa_A^{(c)}) + \psi(\kappa_A^{(c)}, 0)}{\varphi/\varepsilon_{r/f}(\kappa_A^{(c)}) + \psi(\kappa_A^{(c)}, \iota)}. \end{cases} \quad (\text{S77})$$

Here, $\mu_{\lambda_c}(0)$, $\sigma_{\lambda_c}(0)$, $\psi(\kappa_A^{(c)}, 0)$, $\lambda_c(0)$ and $\lambda_{\max}(0)$ stand for the terms free from translation inhibition. Basically, there are distributions of values for $\varepsilon_{r/f}(\kappa_A^{(c)})$, $\psi(\kappa_A^{(c)}, 0)$ and $\psi(\kappa_A^{(c)}, \iota)$. For approximation, we use the deterministic values of these terms in Eq. S77, and then the CV of $\lambda_c(\iota)$ can be approximated by $\lambda_c(0)$. Combining Eqs. S46, S75 and S76, we have:

$$\begin{cases} J_f^{(E)}(\lambda(\kappa_A, \iota), \iota) = \frac{1}{2} \varphi \cdot \lambda(\kappa_A, \iota) \cdot \left[\operatorname{erf}\left(\frac{\lambda(\kappa_A, \iota) - \mu_{\lambda_c}(\iota)}{\sqrt{2}\sigma_{\lambda_c}(\iota)}\right) + 1 \right], \\ J_r^{(E)}(\lambda(\kappa_A, \iota), \iota) = \frac{1}{2} \varphi \cdot \lambda(\kappa_A, \iota) \cdot \left[1 - \operatorname{erf}\left(\frac{\lambda(\kappa_A, \iota) - \mu_{\lambda_c}(\iota)}{\sqrt{2}\sigma_{\lambda_c}(\iota)}\right) \right]. \end{cases} \quad (\text{S78})$$

In the experiments, the inhibition coefficient ι is controllable by tuning the concentration of translation inhibitor. For a given value of ι , $\lambda(\kappa_A, \iota)$ changes monotonously with κ_A . Combining Eqs. S30 and S78, we have (ι is a parameter here):

$$\begin{cases} J_f^{(N)}(\lambda, \iota) = \frac{\varphi \cdot \lambda}{\beta_1 + 2(\beta_2 + \beta_6)} \cdot \left[\operatorname{erf}\left(\frac{\lambda - \mu_{\lambda_c}(\iota)}{\sqrt{2}\sigma_{\lambda_c}(\iota)}\right) + 1 \right], \\ J_r^{(N)}(\lambda, \iota) = \frac{\varphi \cdot \lambda}{\beta_1 + 2(\beta_2 + \beta_3 + \beta_4)} \cdot \left[1 - \operatorname{erf}\left(\frac{\lambda - \mu_{\lambda_c}(\iota)}{\sqrt{2}\sigma_{\lambda_c}(\iota)}\right) \right], \end{cases} \quad (\text{S79})$$

where $\mu_{\lambda_c}(\iota)$ and $\sigma_{\lambda_c}(\iota)$ follow Eq. S77. The growth rate can also be perturbed by altering κ_A and ι simultaneously. Then, the relations among the energy fluxes, growth rate and ι still follow Eq. S79 (here ι is a variable). The comparison between Eq. S79 and experimental data (Basan et al., 2015) is shown in Appendix-fig. 2D (3-D) and 2E (2-D). Overall, it shows good consistency, however, there is still a noticeable discrepancy when ι is large (i.e., with high concentration of translation inhibitor). Then, it led us to consider the maintenance energy w_0 , which is small but may account for this discrepancy. Then, $\lambda(\kappa_A, \iota)$ changes into:

$$\lambda(\kappa_A, \iota) = \begin{cases} \frac{\phi_{\max} - w_0/\varepsilon_r(\kappa_A)}{\varphi/\varepsilon_r(\kappa_A) + \psi(\kappa_A, \iota)} & \varepsilon_r(\kappa_A) > \varepsilon_f(\kappa_A), \\ \frac{\phi_{\max} - w_0/\varepsilon_f(\kappa_A)}{\varphi/\varepsilon_f(\kappa_A) + \psi(\kappa_A, \iota)} & \varepsilon_r(\kappa_A) < \varepsilon_f(\kappa_A), \end{cases} \quad (\text{S80})$$

while $\lambda_c(\iota) \equiv \lambda(\kappa_A^{(C)}, \iota)$ and $\lambda_{\max}(\iota) \equiv \lambda(\kappa_A^{\max}, \iota)$ still follow Eq. S74, although the forms of $\lambda_c(0)$ and $\lambda_{\max}(0)$ change into:

$$\begin{cases} \lambda_c(0) = \frac{\phi_{\max} - w_0/\varepsilon_{r/f}(\kappa_A^{(C)})}{\varphi/\varepsilon_{r/f}(\kappa_A^{(C)}) + \psi(\kappa_A^{(C)}, 0)}, \\ \lambda_{\max}(0) = \frac{\phi_{\max} - w_0/\varepsilon_f(\kappa_A^{\max})}{\varphi/\varepsilon_f(\kappa_A^{\max}) + \psi(\kappa_A^{\max}, 0)}. \end{cases} \quad (\text{S81})$$

In the homogeneous case, $J_f^{(E)}$ and $J_r^{(E)}$ follow:

$$\begin{cases} J_f^{(E)}(\kappa_A, \iota) = [\varphi \cdot \lambda(\kappa_A, \iota) + w_0] \cdot \theta(\lambda(\kappa_A, \iota) - \lambda_c(\iota)), \\ J_r^{(E)}(\kappa_A, \iota) = [\varphi \cdot \lambda(\kappa_A, \iota) + w_0] \cdot [1 - \theta(\lambda(\kappa_A, \iota) - \lambda_c(\iota))]. \end{cases} \quad (S82)$$

To compare with experiments, we assume that the extrinsic noise follows that specified in Appendix 2.3. Combining Eqs. S45, S74 and S81, then, $\lambda_c(\iota)$ approximately follows a Gaussian distribution:

$$\lambda_c(\iota) \sim \mathcal{N}(\mu_{\lambda_c}(\iota), \sigma_{\lambda_c}(\iota)^2). \quad (S83)$$

Here $\mu_{\lambda_c}(\iota)$ and $\sigma_{\lambda_c}(\iota)$ still follow Eq. S77, while $\mu_{\lambda_c}(0)$ and $\sigma_{\lambda_c}(0)$ change accordingly with Eq. S81. For approximation, we use the deterministic values of the relevant terms in Eq. S77, and then the CV of $\lambda_c(\iota)$ is roughly the same as $\lambda_c(0)$. Combining Eqs. S46, S82 and S83, we have:

$$\begin{cases} J_f^{(E)}(\lambda(\kappa_A, \iota), \iota) = \frac{1}{2}(\varphi \cdot \lambda(\kappa_A, \iota) + w_0) \cdot \left[\operatorname{erf}\left(\frac{\lambda(\kappa_A, \iota) - \mu_{\lambda_c}(\iota)}{\sqrt{2}\sigma_{\lambda_c}(\iota)}\right) + 1 \right], \\ J_r^{(E)}(\lambda(\kappa_A, \iota), \iota) = \frac{1}{2}(\varphi \cdot \lambda(\kappa_A, \iota) + w_0) \cdot \left[1 - \operatorname{erf}\left(\frac{\lambda(\kappa_A, \iota) - \mu_{\lambda_c}(\iota)}{\sqrt{2}\sigma_{\lambda_c}(\iota)}\right) \right]. \end{cases} \quad (S84)$$

Thus, for a given ι , $\lambda(\kappa_A, \iota)$ changes monotonously with κ_A . Combining Eqs. S30 and S84, we have (here ι is a parameter):

$$\begin{cases} J_f^{(N)}(\lambda, \iota) = \frac{\varphi \cdot \lambda + w_0}{\beta_1 + 2(\beta_2 + \beta_6)} \cdot \left[\operatorname{erf}\left(\frac{\lambda - \mu_{\lambda_c}(\iota)}{\sqrt{2}\sigma_{\lambda_c}(\iota)}\right) + 1 \right], \\ J_r^{(N)}(\lambda, \iota) = \frac{\varphi \cdot \lambda + w_0}{\beta_1 + 2(\beta_2 + \beta_3 + \beta_4)} \cdot \left[1 - \operatorname{erf}\left(\frac{\lambda - \mu_{\lambda_c}(\iota)}{\sqrt{2}\sigma_{\lambda_c}(\iota)}\right) \right]. \end{cases} \quad (S85)$$

The growth rate and fluxes can also be perturbed by altering κ_A and ι simultaneously. The relations among the energy fluxes, growth rate and ι would still follow Eq. S85 other than that now ι is regarded as a variable. Assuming that there is a tiny amount of maintenance energy. Basically, we assign $w_0 = 2.5 \text{ (h}^{-1}\text{)}$. Then, we see that the experimental results (Basan et al., 2015) agree quantitatively well with the model predictions (Fig. 3C-D).

Appendix 4 Overflow metabolism in substrates other than Group A carbon sources

Due to the topology of metabolic network, Group A carbon sources follow the equation (Eq. S47) of overflow metabolism upon κ_A perturbation (i.e., varying the type or concentration of a Group A carbon source). This has been demonstrated clearly in the above analysis, which agrees quantitatively with experiments. However, further analysis is required for substrates other than Group A sources due to the topological differences in carbon utilization (Wang et al., 2019). Basically, substrates entering from glycolysis or the points before acetyl-CoA are potentially involved in overflow metabolism, while those join from the TCA cycle are not relevant to this behavior. Still, mixed carbon sources are likely to induce a different profile of overflow metabolism, so long as there is a carbon source coming from glycolysis.

Appendix 4.1 Pyruvate

The coarse-grained model for pyruvate utilization is shown in Fig. 3E. Here, nodes M_1, M_2, M_3, M_4, M_5 follow everything depicted in Appendix 2.1. Each biochemical reaction follows Eq. S5 with $b_i = 1$ except that $2M_2 \rightarrow M_1$ and $M_3 + M_5 \rightarrow M_4$. By applying flux balance to the stoichiometric fluxes, combining with Eq. S8, we have:

$$\begin{cases} \Phi_{py} \cdot \xi_{py} = \Phi_7 \cdot \xi_7 + \Phi_8 \cdot \xi_8, \\ \Phi_7 \cdot \xi_7 = 2\Phi_9 \cdot \xi_9 + \Phi_5 \cdot \xi_5 + \Phi_{a2} \cdot \xi_{a2}, \\ \Phi_9 \cdot \xi_9 = \Phi_{a1} \cdot \xi_{a1}, \\ \Phi_8 \cdot \xi_8 = \Phi_3 \cdot \xi_3 + \Phi_6 \cdot \xi_6 + \Phi_b \cdot \xi_b, \\ \Phi_5 \cdot \xi_5 + \Phi_4 \cdot \xi_4 = \Phi_3 \cdot \xi_3 + \Phi_d \cdot \xi_d, \\ \Phi_3 \cdot \xi_3 = \Phi_4 \cdot \xi_4 + \Phi_c \cdot \xi_c. \end{cases} \quad (S86)$$

For energy production, we convert all the energy currencies into ATPs, and then,

$$\beta_8 \cdot \Phi_8 \cdot \xi_8 + \beta_3 \cdot \Phi_3 \cdot \xi_3 + \beta_4 \cdot \Phi_4 \cdot \xi_4 + \beta_6 \cdot \Phi_6 \cdot \xi_6 + \beta_{a1} \cdot \Phi_{a1} \cdot \xi_{a1} - \beta_7 \cdot \Phi_7 \cdot \xi_7 - \beta_9 \cdot \Phi_9 \cdot \xi_9 = J_E, \quad (S87)$$

where $\beta_7 = 1$, $\beta_8 = 2$, $\beta_3 = 2$, $\beta_4 = 6$, $\beta_6 = 1$, $\beta_9 = 6$, $\beta_{a1} = 4$ (Neidhardt et al., 1990; Sauer et al., 2004), and J_E follows Eq. S25. By applying the substitutions specified in Eqs. S9, S12, S14-S18, combined with Eqs. S4, S10, S22, S23, S25, S86-S87, and the constraint of proteome resource allocation, we have:

$$\begin{cases}
\phi_{\text{py}} \cdot \kappa_{\text{py}} = \phi_7 \cdot \kappa_7 + \phi_8 \cdot \kappa_8, \\
\phi_7 \cdot \kappa_7 = 2\phi_9 \cdot \kappa_9 + \phi_5 \cdot \kappa_5 + \phi_{a2} \cdot \kappa_{a2}, \\
\phi_9 \cdot \kappa_9 = \phi_{a1} \cdot \kappa_{a1} \\
\phi_8 \cdot \kappa_8 = \phi_3 \cdot \kappa_3 + \phi_6 \cdot \kappa_6 + \phi_b \cdot \kappa_b \\
\phi_3 \cdot \kappa_3 = \phi_4 \cdot \kappa_4 + \phi_c \cdot \kappa_c \\
\phi_5 \cdot \kappa_5 + \phi_4 \cdot \kappa_4 = \phi_3 \cdot \kappa_3 + \phi_d \cdot \kappa_d \\
\phi_{a1} \cdot \kappa_{a1} = \eta_{a1} \cdot \lambda, \phi_{a2} \cdot \kappa_{a2} = \eta_{a2} \cdot \lambda, \phi_b \cdot \kappa_b = \eta_b \cdot \lambda, \phi_c \cdot \kappa_c = \eta_c \cdot \lambda, \phi_d \cdot \kappa_d = \eta_d \cdot \lambda, \\
\beta_8 \cdot \phi_8 \cdot \kappa_8 + \beta_3 \cdot \phi_3 \cdot \kappa_3 + \beta_4 \cdot \phi_4 \cdot \kappa_4 + \beta_6 \cdot \phi_6 \cdot \kappa_6 + \beta_{a1} \cdot \phi_{a1} \cdot \kappa_{a1} - \beta_7 \cdot \phi_7 \cdot \kappa_7 - \beta_9 \cdot \phi_9 \cdot \kappa_9 = J_{\text{E}}^{(\text{N})}, \\
J_{\text{E}}^{(\text{N})} = \eta_{\text{E}} \cdot \lambda, \lambda = \phi_R \cdot \kappa_r, J_r^{(\text{N})} = \phi_4 \cdot \kappa_4, J_f^{(\text{N})} = \phi_6 \cdot \kappa_6, \\
\phi_R + \phi_{\text{py}} + \phi_3 + \phi_4 + \phi_5 + \phi_6 + \phi_7 + \phi_8 + \phi_9 + \phi_{a1} + \phi_{a2} + \phi_b + \phi_c + \phi_d = \phi_{\text{max}},
\end{cases} \quad (\text{S88})$$

where $\eta_{\text{E}} = r_{\text{E}} \cdot \left[\sum_i r_i / N_{\text{EP}_i}^{\text{carbon}} \right]^{-1}$. κ_i is approximately a constant which follows Eq. S20 for each of the intermediate node. The substrate quality of κ_{py} varies with the external concentration of pyruvate ([py]),

$$\kappa_{\text{py}} \equiv \frac{r_{\text{protein}}}{r_{\text{carbon}}} \cdot \frac{k_{\text{py}}^{\text{cat}}}{m_{E_{\text{py}}}} \cdot \frac{[\text{py}]}{[\text{py}] + K_{\text{py}}} \cdot m_0. \quad (\text{S89})$$

From Eq. S88, all ϕ_i can be expressed by $J_r^{(\text{N})}$, $J_f^{(\text{N})}$, and λ :

$$\begin{cases}
\phi_{\text{py}} = \left[(2\eta_{a1} + \eta_{a2} + \eta_b + 2\eta_c + \eta_d) \lambda + J_r^{(\text{N})} + J_f^{(\text{N})} \right] / \kappa_{\text{py}}, \\
\phi_7 = (2\eta_{a1} + \eta_{a2} + \eta_c + \eta_d) \lambda / \kappa_7, \phi_9 = \eta_{a1} \cdot \lambda / \kappa_9 \\
\phi_8 = \left[J_r^{(\text{N})} + J_f^{(\text{N})} + (\eta_b + \eta_c) \lambda \right] / \kappa_8 \\
\phi_3 = (J_r^{(\text{N})} + \eta_c \cdot \lambda) / \kappa_3, \phi_4 = J_r^{(\text{N})} / \kappa_4, \\
\phi_5 = (\eta_c + \eta_d) \lambda / \kappa_5, \phi_6 = J_f^{(\text{N})} / \kappa_6, \\
\phi_i = \eta_i \cdot \lambda / \kappa_i \quad (i = a1, a2, b, c, d).
\end{cases} \quad (\text{S90})$$

By substituting Eq. S90 into Eq. S88, we have:

$$\begin{cases}
J_r^{(\text{E,py})} + J_f^{(\text{E,py})} = \phi_{\text{py}} \cdot \lambda, \\
\frac{J_r^{(\text{E,py})}}{\mathcal{E}_r^{(\text{py})}} + \frac{J_f^{(\text{E,py})}}{\mathcal{E}_f^{(\text{py})}} = \phi_{\text{max}} - \psi_{\text{py}} \cdot \lambda.
\end{cases} \quad (\text{S91})$$

Here, $J_r^{(E,py)}$ and $J_f^{(E,py)}$ stand for the normalized energy fluxes of respiration and fermentation, respectively, with

$$\begin{cases} J_r^{(E,py)} = (\beta_3 + \beta_4 + \beta_8) \cdot J_r^{(N)}, \\ J_f^{(E,py)} = (\beta_6 + \beta_8) \cdot J_f^{(N)}. \end{cases} \quad (S92)$$

The coefficients $\varepsilon_r^{(py)}$ and $\varepsilon_f^{(py)}$ represent the proteome energy efficiencies of respiration and fermentation, respectively (Appendix-fig. 1C-D), with

$$\begin{cases} \varepsilon_r^{(py)} = \frac{\beta_3 + \beta_4 + \beta_8}{1/\kappa_{py} + 1/\kappa_8 + 1/\kappa_3 + 1/\kappa_4}, \\ \varepsilon_f^{(py)} = \frac{\beta_6 + \beta_8}{1/\kappa_{py} + 1/\kappa_8 + 1/\kappa_6}. \end{cases} \quad (S93)$$

ψ_{py}^{-1} is the proteome efficiency of biomass pathway (Appendix-fig. 1E), with

$$\psi_{py} = \frac{1}{\kappa_t} + \frac{1 + \eta_{a1} + \eta_c}{\kappa_{py}} + \frac{1 - \eta_b + \eta_{a1}}{\kappa_7} + \frac{\eta_b + \eta_c}{\kappa_8} + \frac{\eta_{a1}}{\kappa_9} + \frac{\eta_c}{\kappa_3} + \frac{\eta_c + \eta_d}{\kappa_5} + \sum_i^{a1,a2,b,c,d} \frac{\eta_i}{\kappa_i}. \quad (S94)$$

φ_{py} is the energy demand coefficient (a constant), with

$$\varphi_{py} \equiv \eta_E + \beta_7 \cdot (1 - \eta_b + \eta_{a1}) + \beta_9 \cdot \eta_{a1} - \beta_8 \cdot (\eta_c + \eta_b) - \beta_3 \cdot \eta_c - \beta_{a1} \cdot \eta_{a1}, \quad (S95)$$

Evidently, Eq. S91 is identical in form with Eq. S29. The growth rate changes into κ_{py} dependent:

$$\lambda(\kappa_{py}) = \begin{cases} \frac{\phi_{\max}}{\varphi_{py}/\varepsilon_r^{(py)}(\kappa_{py}) + \psi_{py}(\kappa_{py})} & \varepsilon_r^{(py)}(\kappa_{py}) > \varepsilon_f^{(py)}(\kappa_{py}), \\ \frac{\phi_{\max}}{\varphi_{py}/\varepsilon_f^{(py)}(\kappa_{py}) + \psi_{py}(\kappa_{py})} & \varepsilon_r^{(py)}(\kappa_{py}) < \varepsilon_f^{(py)}(\kappa_{py}). \end{cases} \quad (S96)$$

When κ_{py} is very small, combined with Eq. S93, then,

$$\begin{cases} \varepsilon_r^{(py)}(\kappa_{py} \rightarrow 0) \approx (\beta_3 + \beta_4 + \beta_8) \cdot \kappa_{py}, \\ \varepsilon_f^{(py)}(\kappa_{py} \rightarrow 0) \approx (\beta_6 + \beta_8) \cdot \kappa_{py}. \end{cases} \quad (S97)$$

Obviously,

$$\varepsilon_r^{(py)}(\kappa_{py} \rightarrow 0) > \varepsilon_f^{(py)}(\kappa_{py} \rightarrow 0). \quad (S98)$$

As long as

$$\frac{\beta_3 + \beta_4 - \beta_6}{\kappa_{\text{py}}^{(\text{ST})}} < (\beta_6 + \beta_8) \left(\frac{1}{\kappa_8} + \frac{1}{\kappa_3} + \frac{1}{\kappa_4} \right) - (\beta_3 + \beta_4 + \beta_8) \cdot \left(\frac{1}{\kappa_8} + \frac{1}{\kappa_6} \right), \quad (\text{S99})$$

where the superscript “(ST)” stands for the saturated concentration, then,

$$\varepsilon_r^{(\text{py})}(\kappa_{\text{py}}^{(\text{ST})}) < \varepsilon_f^{(\text{py})}(\kappa_{\text{py}}^{(\text{ST})}), \quad (\text{S100})$$

and there exists a critical value of κ_{py} , denoted as $\kappa_{\text{py}}^{(\text{C})}$, with

$$\begin{cases} \varepsilon_r^{(\text{py})}(\kappa_{\text{py}}^{(\text{C})}) = \varepsilon_f^{(\text{py})}(\kappa_{\text{py}}^{(\text{C})}) = \frac{\beta_3 + \beta_4 - \beta_6}{1/\kappa_3 + 1/\kappa_4 - 1/\kappa_6}, \\ \lambda_{\text{C}}^{(\text{py})} \equiv \lambda(\kappa_{\text{py}}^{(\text{C})}) = \frac{\phi_{\text{max}}}{\varphi_{\text{py}}/\varepsilon_{r/f}^{(\text{py})}(\kappa_{\text{py}}^{(\text{C})}) + \psi_{\text{py}}(\kappa_{\text{py}}^{(\text{C})})}. \end{cases} \quad (\text{S101})$$

Here, $\lambda_{\text{C}}^{(\text{py})}$ is the growth rate at the transition point, and $\varepsilon_{r/f}^{(\text{py})}$ stands for either $\varepsilon_r^{(\text{py})}$ or $\varepsilon_f^{(\text{py})}$. In Appendix-fig. 2H, we show the dependencies of $\varepsilon_r^{(\text{py})}(\kappa_{\text{py}})$, $\varepsilon_f^{(\text{py})}(\kappa_{\text{py}})$ and $\lambda(\kappa_{\text{py}})$ on κ_{py} in a 3-dimensional form. In the homogeneous case, $J_f^{(\text{E,py})}$ and $J_r^{(\text{E,py})}$ follow:

$$\begin{cases} J_f^{(\text{E,py})} = \varphi_{\text{py}} \cdot \lambda \cdot \theta(\lambda - \lambda_{\text{C}}^{(\text{py})}), \\ J_r^{(\text{E,py})} = \varphi_{\text{py}} \cdot \lambda \cdot [1 - \theta(\lambda - \lambda_{\text{C}}^{(\text{py})})]. \end{cases} \quad (\text{S102})$$

Defining $\lambda_{\text{max}}^{(\text{py})} = \lambda(\kappa_{\text{py}}^{(\text{ST})})$, and then, $[0, \lambda_{\text{max}}^{(\text{py})}]$ is the relevant range of the x axis. To compare with experiments, we assume the same extent of extrinsic noise in k_i^{cat} as specified in Appendix 2.3. Then, $\lambda_{\text{C}}^{(\text{py})}$ approximately follows a Gaussian distribution:

$$\lambda_{\text{C}}^{(\text{py})} \sim \mathcal{N}\left(\mu_{\lambda_{\text{C}}^{(\text{py})}}, \sigma_{\lambda_{\text{C}}^{(\text{py})}}^2\right), \quad (\text{S103})$$

where $\mu_{\lambda_{\text{C}}^{(\text{py})}}$ and $\sigma_{\lambda_{\text{C}}^{(\text{py})}}$ stand for the mean and standard deviation of $\lambda_{\text{C}}^{(\text{py})}$. Then, the relations between the normalized energy fluxes and growth rate are:

$$\begin{cases} J_f^{(\text{E,py})}(\lambda) = \frac{1}{2} \varphi_{\text{py}} \cdot \lambda \cdot \left[\text{erf}\left(\frac{\lambda - \mu_{\lambda_{\text{C}}^{(\text{py})}}}{\sqrt{2}\sigma_{\lambda_{\text{C}}^{(\text{py})}}}\right) + 1 \right], \\ J_r^{(\text{E,py})}(\lambda) = \frac{1}{2} \varphi_{\text{py}} \cdot \lambda \cdot \left[1 - \text{erf}\left(\frac{\lambda - \mu_{\lambda_{\text{C}}^{(\text{py})}}}{\sqrt{2}\sigma_{\lambda_{\text{C}}^{(\text{py})}}}\right) \right]. \end{cases} \quad (\text{S104})$$

Combined with Eq. S92, we have:

$$\begin{cases} J_f^{(N)}(\lambda) = \frac{\varphi_{py}}{2(\beta_6 + \beta_8)} \cdot \lambda \cdot \left[\operatorname{erf}\left(\frac{\lambda - \mu_{\lambda_c^{(py)}}}{\sqrt{2}\sigma_{\lambda_c^{(py)}}}\right) + 1 \right], \\ J_r^{(N)}(\lambda) = \frac{\varphi_{py}}{2(\beta_3 + \beta_4 + \beta_8)} \cdot \lambda \cdot \left[1 - \operatorname{erf}\left(\frac{\lambda - \mu_{\lambda_c^{(py)}}}{\sqrt{2}\sigma_{\lambda_c^{(py)}}}\right) \right]. \end{cases} \quad (\text{S105})$$

In Fig. 3F, we show that the model predictions (Eq. S105) agree quantitatively with the experimental results (Holms, 1996).

Appendix 4.2 Mixture of a Group A carbon source with extracellular amino acids

In the case of a Group A carbon source mixed with amino acids, the coarse-grained model is shown in Appendix-fig. 2A. In fact, this model can be used to analyze mixtures with one or multiple types of extracellular amino acids. Here, Eqs. S21, S22, S24 and S25 still apply, but Eq. S23 changes to (the case of $i = a1$ remains the same as Eq. S23):

$$\Phi_i \cdot \xi_i \cdot N_{EP_i}^{\text{carbon}} + \Phi'_i \cdot \xi'_i \cdot N_{P_i}^{\text{carbon}} = r_i \cdot J_{\text{BM}} \quad (i = a2, b, c, d). \quad (\text{S106})$$

Here, $N_{P_i}^{\text{carbon}}$ represents the number of carbon atoms in a molecule of Pool i . For simplicity, we assume:

$$N_{P_i}^{\text{carbon}} \approx N_{EP_i}^{\text{carbon}}. \quad (\text{S107})$$

In the case where all 21 types of amino acids are present and each in saturated concentration (denoted as “21AA”), we have:

$$\begin{cases} \phi_A \cdot \kappa_A = \phi_1 \cdot \kappa_1 + \phi_{a1} \cdot \kappa_{a1}, \\ 2\phi_1 \cdot \kappa_1 = \phi_2 \cdot \kappa_2 + \phi_5 \cdot \kappa_5 + \phi_{a2} \cdot \kappa_{a2}, \\ \phi_2 \cdot \kappa_2 = \phi_3 \cdot \kappa_3 + \phi_6 \cdot \kappa_6 + \phi_b \cdot \kappa_b, \\ \phi_5 \cdot \kappa_5 + \phi_4 \cdot \kappa_4 = \phi_3 \cdot \kappa_3 + \phi_d \cdot \kappa_d, \\ \phi_3 \cdot \kappa_3 = \phi_4 \cdot \kappa_4 + \phi_c \cdot \kappa_c, \\ \phi_{a1} \cdot \kappa_{a1} = \eta_{a1} \cdot \lambda, \phi_{a2} \cdot \kappa_{a2} + \phi_{a2}^{(21AA)} \cdot \kappa_{a2}^{(21AA)} = \eta_{a2} \cdot \lambda, \phi_b \cdot \kappa_b + \phi_b^{(21AA)} \cdot \kappa_b^{(21AA)} = \eta_b \cdot \lambda, \\ \phi_c \cdot \kappa_c + \phi_c^{(21AA)} \cdot \kappa_c^{(21AA)} = \eta_c \cdot \lambda, \phi_d \cdot \kappa_d + \phi_d^{(21AA)} \cdot \kappa_d^{(21AA)} = \eta_d \cdot \lambda, \\ \beta_1 \cdot \phi_1 \cdot \kappa_1 + \beta_2 \cdot \phi_2 \cdot \kappa_2 + \beta_3 \cdot \phi_3 \cdot \kappa_3 + \beta_4 \cdot \phi_4 \cdot \kappa_4 + \beta_6 \cdot \phi_6 \cdot \kappa_6 + \beta_{a1} \cdot \phi_{a1} \cdot \kappa_{a1} = J_E^{(N)}, \\ J_E^{(N)} = \eta_E \cdot \lambda, \lambda = \phi_R \cdot \kappa_i, J_r^{(N)} = \phi_4 \cdot \kappa_4, J_f^{(N)} = \phi_6 \cdot \kappa_6, \\ \phi_R + \phi_A + \sum_i^6 \phi_i + \sum_j^{a1, a2, b, c, d} \phi_j + \phi_{a2}^{(21AA)} + \phi_b^{(21AA)} + \phi_c^{(21AA)} + \phi_d^{(21AA)} = \phi_{\text{max}}, \end{cases} \quad (\text{S108})$$

where ϕ_i and κ_i are defined following Eqs. S9 and S12. Since the cell growth rate elevates significantly with the mixture of amino acids, we deduce that Pools a2-d are supplied by amino acids in growth optimization, with

$$\phi_i = 0 \quad (i = a2, b, c, d). \quad (\text{S109})$$

Basically, amino acids should be more efficient in the supply of biomass production than the Group A carbon source for Pools a2-d, i.e.,

$$\begin{cases} 1/\kappa_{a2}^{(21AA)} < 1/\kappa_{a2} + 1/(2\kappa_1) + 1/(2\kappa_A), \\ 1/\kappa_b^{(21AA)} < 1/\kappa_b + 1/\kappa_2 + 1/(2\kappa_1) + 1/(2\kappa_A), \\ 1/\kappa_c^{(21AA)} < 1/\kappa_c + 1/\kappa_5 + 1/\kappa_3 + 1/\kappa_2 + 1/\kappa_1 + 1/\kappa_A, \\ 1/\kappa_d^{(21AA)} < 1/\kappa_d + 1/\kappa_5 + 1/(2\kappa_1) + 1/(2\kappa_A). \end{cases} \quad (\text{S110})$$

In practice, the requirement is even higher for proteome efficiency using amino acids, since the biomass production pathway is accompanied by energy production in the case of Group A carbon sources, yet not for amino acids. Combining Eqs. S108 and S109, we have:

$$\begin{cases} J_r^{(E)} + J_f^{(E)} = \varphi_{21AA} \cdot \lambda, \\ \frac{J_r^{(E)}}{\varepsilon_r} + \frac{J_f^{(E)}}{\varepsilon_f} = \phi_{\max} - \psi_{21AA} \cdot \lambda, \end{cases} \quad (\text{S111})$$

where $J_r^{(E)}$, $J_f^{(E)}$ follow Eq. S30, while ε_r and ε_f follow Eq. S31. ψ_{21AA}^{-1} is the proteome efficiency of biomass pathway under this nutrient condition, with

$$\psi_{21AA} = \frac{1}{\kappa_t} + \frac{\eta_{a1}}{\kappa_A} + \frac{\eta_{a1}}{\kappa_{a1}} + \frac{\eta_{a2}}{\kappa_{a2}^{(21AA)}} + \frac{\eta_b}{\kappa_b^{(21AA)}} + \frac{\eta_c}{\kappa_c^{(21AA)}} + \frac{\eta_d}{\kappa_d^{(21AA)}}. \quad (\text{S112})$$

φ_{21AA} is the energy demand coefficient, with

$$\varphi_{21AA} \equiv \eta_E - \beta_{a1} \cdot \eta_{a1}. \quad (\text{S113})$$

Combining Eqs. S111 and S31, it is easy to obtain the formula for the growth rate:

$$\lambda(\kappa_A) = \begin{cases} \lambda_r^{(21AA)} \equiv \frac{\phi_{\max}}{\varphi_{21AA}/\varepsilon_r(\kappa_A) + \psi_{21AA}(\kappa_A)} & \varepsilon_r(\kappa_A) > \varepsilon_f(\kappa_A), \\ \lambda_f^{(21AA)} \equiv \frac{\phi_{\max}}{\varphi_{21AA}/\varepsilon_f(\kappa_A) + \psi_{21AA}(\kappa_A)} & \varepsilon_r(\kappa_A) < \varepsilon_f(\kappa_A). \end{cases} \quad (\text{S114})$$

In fact, Eqs. S37-S42 still apply. $\varepsilon_{r/f}(\kappa_A^{(C)})$ satisfies Eq. S43, while $\lambda_C^{(21AA)} \equiv \lambda(\kappa_A^{(C)})$ and $\lambda_{\max}^{(21AA)} \equiv \lambda(\kappa_A^{\max})$ are:

$$\begin{cases} \lambda_c^{(21AA)} = \frac{\phi_{\max}}{\varphi_{21AA}/\varepsilon_{r/f}(\kappa_A^{(C)}) + \psi_{21AA}(\kappa_A^{(C)})}, \\ \lambda_{\max}^{(21AA)} = \frac{\phi_{\max}}{\varphi_{21AA}/\varepsilon_f(\kappa_A^{\max}) + \psi_{21AA}(\kappa_A^{\max})}. \end{cases} \quad (\text{S115})$$

When extrinsic noise is taken into account, $\lambda_c^{(21AA)}$ approximately follows a Gaussian distribution:

$$\lambda_c^{(21AA)} \sim \mathcal{N}\left(\mu_{\lambda_c^{(21AA)}}, \sigma_{\lambda_c^{(21AA)}}^2\right), \quad (\text{S116})$$

and the normalized fluxes $J_r^{(N)}$, $J_f^{(N)}$ change into:

$$\begin{cases} J_f^{(N)}(\lambda) = \frac{\varphi_{21AA}}{\beta_1 + 2(\beta_2 + \beta_6)} \cdot \lambda \cdot \left[\text{erf}\left(\frac{\lambda - \mu_{\lambda_c^{(21AA)}}}{\sqrt{2}\sigma_{\lambda_c^{(21AA)}}}\right) + 1 \right], \\ J_r^{(N)}(\lambda) = \frac{\varphi_{21AA}}{\beta_1 + 2(\beta_2 + \beta_3 + \beta_4)} \cdot \lambda \cdot \left[1 - \text{erf}\left(\frac{\lambda - \mu_{\lambda_c^{(21AA)}}}{\sqrt{2}\sigma_{\lambda_c^{(21AA)}}}\right) \right]. \end{cases} \quad (\text{S117})$$

In fact, the above analysis can be extended to cases where a Group A carbon source is mixed with arbitrary combinations of amino acids. Eqs. S111, S114-S117 would remain in a similar form, while Eqs. S112-S113 would change depending on the amino acid combinations. In Appendix-fig. 2B-C, we show the comparisons between model predictions (see also Appendix 7.2 and Eq. S157) and experimental data (Basan et al., 2015; Wallden et al., 2016) in mixtures of 21 or 7 types of amino acids together with a Group A carbon source, which agree quantitatively.

Appendix 5 Enzyme allocation upon perturbations

Appendix 5.1 Carbon limitation within Group A carbon sources

In Eq. S28, we present the model predictions of the dependencies of enzyme protein fractions on growth rate and energy fluxes. To compare with experiments, we assume the same extent of extrinsic noise in k_i^{cat} as specified in Appendix 2.3. In fact, relative protein expression data for enzymes within glycolysis and the TCA cycle are available from existing studies, which are comparable to the ϕ_1 - ϕ_4 enzymes of our model (Fig. 1B). Upon κ_A perturbation, κ_A is a variable while $w_0 = 0$ is fixed (see Appendix 1.5). Combining Eqs. S28 and S47 (with $w_0 = 0$), we obtain:

$$\begin{cases}
\phi_1 = \frac{\lambda}{\kappa_1} \left\{ \frac{\varphi \cdot (\beta_3 + \beta_4 - \beta_6)}{[\beta_1 + 2(\beta_2 + \beta_3 + \beta_4)] \cdot [\beta_1 + 2(\beta_2 + \beta_6)]} \cdot \left[\operatorname{erf} \left(\frac{\lambda - \mu_{\lambda_c}}{\sqrt{2}\sigma_{\lambda_c}} \right) + 1 \right] + \frac{\varphi}{\beta_1 + 2(\beta_2 + \beta_3 + \beta_4)} + \frac{\eta_{a2} + \eta_b + 2\eta_c + \eta_d}{2} \right\}, \\
\phi_2 = \frac{\lambda}{\kappa_2} \left\{ \frac{2\varphi \cdot (\beta_3 + \beta_4 - \beta_6)}{[\beta_1 + 2(\beta_2 + \beta_3 + \beta_4)] \cdot [\beta_1 + 2(\beta_2 + \beta_6)]} \cdot \left[\operatorname{erf} \left(\frac{\lambda - \mu_{\lambda_c}}{\sqrt{2}\sigma_{\lambda_c}} \right) + 1 \right] + \frac{2\varphi}{\beta_1 + 2(\beta_2 + \beta_3 + \beta_4)} + \eta_b + \eta_c \right\}, \\
\phi_3 = \frac{\lambda}{\kappa_3} \left\{ \frac{\varphi}{\beta_1 + 2(\beta_2 + \beta_3 + \beta_4)} \cdot \left[1 - \operatorname{erf} \left(\frac{\lambda - \mu_{\lambda_c}}{\sqrt{2}\sigma_{\lambda_c}} \right) \right] + \eta_c \right\}, \\
\phi_4 = \frac{\lambda}{\kappa_4} \cdot \frac{\varphi}{\beta_1 + 2(\beta_2 + \beta_3 + \beta_4)} \cdot \left[1 - \operatorname{erf} \left(\frac{\lambda - \mu_{\lambda_c}}{\sqrt{2}\sigma_{\lambda_c}} \right) \right].
\end{cases} \tag{S118}$$

In Appendix-fig. 3C-D, we show the comparisons between model predictions (Eq. S118, $w_0 = 0$) and experimental data (Hui et al., 2015), which are consistent overall. We proceed to consider the influence of maintenance energy as specified in Appendix 3.2. Here, we still choose $w_0 = 2.5 \text{ (} h^{-1} \text{)}$ as previously adopted in Appendix 3.3. Then, Eq. S28 still holds, combined with Eq. S85 in the condition that $t = 0$, we have:

$$\begin{cases}
\phi_1 = \frac{1}{2 \cdot \kappa_1} \left\{ \frac{\varphi \cdot \lambda + w_0}{\beta_1 + 2(\beta_2 + \beta_6)} \cdot \left[\operatorname{erf} \left(\frac{\lambda - \mu_{\lambda_c}}{\sqrt{2}\sigma_{\lambda_c}} \right) + 1 \right] + \frac{\varphi \cdot \lambda + w_0}{\beta_1 + 2(\beta_2 + \beta_3 + \beta_4)} \cdot \left[1 - \operatorname{erf} \left(\frac{\lambda - \mu_{\lambda_c}}{\sqrt{2}\sigma_{\lambda_c}} \right) \right] + (\eta_{a2} + \eta_b + 2\eta_c + \eta_d) \lambda \right\}, \\
\phi_2 = \frac{1}{\kappa_2} \left\{ \frac{\varphi \cdot \lambda + w_0}{\beta_1 + 2(\beta_2 + \beta_6)} \cdot \left[\operatorname{erf} \left(\frac{\lambda - \mu_{\lambda_c}}{\sqrt{2}\sigma_{\lambda_c}} \right) + 1 \right] + \frac{\varphi \cdot \lambda + w_0}{\beta_1 + 2(\beta_2 + \beta_3 + \beta_4)} \cdot \left[1 - \operatorname{erf} \left(\frac{\lambda - \mu_{\lambda_c}}{\sqrt{2}\sigma_{\lambda_c}} \right) \right] + (\eta_b + \eta_c) \lambda \right\}, \\
\phi_3 = \frac{1}{\kappa_3} \left\{ \frac{\varphi \cdot \lambda + w_0}{\beta_1 + 2(\beta_2 + \beta_3 + \beta_4)} \cdot \left[1 - \operatorname{erf} \left(\frac{\lambda - \mu_{\lambda_c}}{\sqrt{2}\sigma_{\lambda_c}} \right) \right] + \eta_c \cdot \lambda \right\}, \\
\phi_4 = \frac{1}{\kappa_4} \cdot \frac{\varphi \cdot \lambda + w_0}{\beta_1 + 2(\beta_2 + \beta_3 + \beta_4)} \cdot \left[1 - \operatorname{erf} \left(\frac{\lambda - \mu_{\lambda_c}}{\sqrt{2}\sigma_{\lambda_c}} \right) \right].
\end{cases} \tag{S119}$$

In Fig. 4A-B, we show that the model predictions (Eq. S119, $w_0 = 2.5 \text{ (} h^{-1} \text{)}$) generally agree with the experiments (Hui et al., 2015). However, there are different basal expressions of these enzymes, which are probably due to living demands other than cell proliferation, such as preparation for starvation (Mori et al., 2017) or alteration in the type of the nutrient (Basan et al., 2020; Kussell and Leibler, 2005).

Appendix 5.2 Overexpression of useless proteins

In the case of ϕ_Z perturbation under each nutrient condition with fixed κ_A (see Appendix 3.1), we consider the same extent of extrinsic noise in k_i^{cat} as specified in Appendix 2.3. The relation

between enzyme allocation and growth rate can be obtained by combining Eqs. S28 and S58 (with $w_0 = 0$):

$$\begin{aligned}
 \phi_1 &= \frac{\lambda}{2 \cdot \kappa_1} \left\{ \frac{\varphi \cdot \left[1 - \operatorname{erf} \left(\frac{\lambda(\kappa_A, 0) - \mu_{\lambda_c}(0)}{\sqrt{2}\sigma_{\lambda_c}(0)} \right) \right]}{\beta_1 + 2(\beta_2 + \beta_3 + \beta_4)} + \frac{\varphi \cdot \left[\operatorname{erf} \left(\frac{\lambda(\kappa_A, 0) - \mu_{\lambda_c}(0)}{\sqrt{2}\sigma_{\lambda_c}(0)} \right) + 1 \right]}{\beta_1 + 2(\beta_2 + \beta_6)} + (\eta_{a2} + \eta_b + 2\eta_c + \eta_d) \right\}, \\
 \phi_2 &= \frac{\lambda}{\kappa_2} \left\{ \frac{\varphi \cdot \left[1 - \operatorname{erf} \left(\frac{\lambda(\kappa_A, 0) - \mu_{\lambda_c}(0)}{\sqrt{2}\sigma_{\lambda_c}(0)} \right) \right]}{\beta_1 + 2(\beta_2 + \beta_3 + \beta_4)} + \frac{\varphi \cdot \left[\operatorname{erf} \left(\frac{\lambda(\kappa_A, 0) - \mu_{\lambda_c}(0)}{\sqrt{2}\sigma_{\lambda_c}(0)} \right) + 1 \right]}{\beta_1 + 2(\beta_2 + \beta_6)} + (\eta_b + \eta_c) \right\}, \\
 \phi_3 &= \frac{\lambda}{\kappa_3} \left\{ \frac{\varphi}{\beta_1 + 2(\beta_2 + \beta_3 + \beta_4)} \cdot \left[1 - \operatorname{erf} \left(\frac{\lambda(\kappa_A, 0) - \mu_{\lambda_c}(0)}{\sqrt{2}\sigma_{\lambda_c}(0)} \right) \right] + \eta_c \right\}, \\
 \phi_4 &= \frac{\lambda}{\kappa_4} \left\{ \frac{\varphi}{\beta_1 + 2(\beta_2 + \beta_3 + \beta_4)} \cdot \left[1 - \operatorname{erf} \left(\frac{\lambda(\kappa_A, 0) - \mu_{\lambda_c}(0)}{\sqrt{2}\sigma_{\lambda_c}(0)} \right) \right] \right\}.
 \end{aligned} \tag{S120}$$

Here $\lambda(\kappa_A, 0)$ is the growth rate for $\phi_z = 0$ and thus is a parameter rather than a variable. The growth rate is defined as $\lambda(\kappa_A, \phi_z)$, which follows Eq. S50. Thus, ϕ_i is proportional to the growth rate λ . In Appendix-fig. 3E-F, we see that the model predictions (Eq. S120) agree with the experiments (Basan et al., 2015) overall. Next, we consider the influence of maintenance energy with $w_0 = 2.5 \text{ (h}^{-1}\text{)}$. Combining Eqs. S28, S58 and S85 (with $\iota = 0$), we get:

$$\begin{aligned}
 \phi_1 &= \frac{w_0}{2 \cdot \kappa_1} \left\{ \frac{1}{\beta_1 + 2(\beta_2 + \beta_6)} \cdot \left[\operatorname{erf} \left(\frac{\lambda(\kappa_A, 0) - \mu_{\lambda_c}(0)}{\sqrt{2}\sigma_{\lambda_c}(0)} \right) + 1 \right] + \frac{1}{\beta_1 + 2(\beta_2 + \beta_3 + \beta_4)} \cdot \left[1 - \operatorname{erf} \left(\frac{\lambda(\kappa_A, 0) - \mu_{\lambda_c}(0)}{\sqrt{2}\sigma_{\lambda_c}(0)} \right) \right] \right\} \\
 &+ \frac{\lambda}{2 \cdot \kappa_1} \left\{ \frac{\varphi}{\beta_1 + 2(\beta_2 + \beta_6)} \cdot \left[\operatorname{erf} \left(\frac{\lambda(\kappa_A, 0) - \mu_{\lambda_c}(0)}{\sqrt{2}\sigma_{\lambda_c}(0)} \right) + 1 \right] + \frac{\varphi}{\beta_1 + 2(\beta_2 + \beta_3 + \beta_4)} \cdot \left[1 - \operatorname{erf} \left(\frac{\lambda(\kappa_A, 0) - \mu_{\lambda_c}(0)}{\sqrt{2}\sigma_{\lambda_c}(0)} \right) \right] + (\eta_{a2} + \eta_b + 2\eta_c + \eta_d) \right\}, \\
 \phi_2 &= \frac{w_0}{\kappa_2} \left\{ \frac{1}{\beta_1 + 2(\beta_2 + \beta_6)} \cdot \left[\operatorname{erf} \left(\frac{\lambda(\kappa_A, 0) - \mu_{\lambda_c}(0)}{\sqrt{2}\sigma_{\lambda_c}(0)} \right) + 1 \right] + \frac{1}{\beta_1 + 2(\beta_2 + \beta_3 + \beta_4)} \cdot \left[1 - \operatorname{erf} \left(\frac{\lambda(\kappa_A, 0) - \mu_{\lambda_c}(0)}{\sqrt{2}\sigma_{\lambda_c}(0)} \right) \right] \right\} \\
 &+ \frac{\lambda}{\kappa_2} \left\{ \frac{\varphi}{\beta_1 + 2(\beta_2 + \beta_6)} \cdot \left[\operatorname{erf} \left(\frac{\lambda(\kappa_A, 0) - \mu_{\lambda_c}(0)}{\sqrt{2}\sigma_{\lambda_c}(0)} \right) + 1 \right] + \frac{\varphi}{\beta_1 + 2(\beta_2 + \beta_3 + \beta_4)} \cdot \left[1 - \operatorname{erf} \left(\frac{\lambda(\kappa_A, 0) - \mu_{\lambda_c}(0)}{\sqrt{2}\sigma_{\lambda_c}(0)} \right) \right] + (\eta_b + \eta_c) \right\}, \\
 \phi_3 &= \frac{\lambda}{\kappa_3} \left\{ \frac{\varphi}{\beta_1 + 2(\beta_2 + \beta_3 + \beta_4)} \cdot \left[1 - \operatorname{erf} \left(\frac{\lambda(\kappa_A, 0) - \mu_{\lambda_c}(0)}{\sqrt{2}\sigma_{\lambda_c}(0)} \right) \right] + \eta_c \right\} + \frac{w_0}{\kappa_3} \cdot \frac{1}{\beta_1 + 2(\beta_2 + \beta_3 + \beta_4)} \cdot \left[1 - \operatorname{erf} \left(\frac{\lambda(\kappa_A, 0) - \mu_{\lambda_c}(0)}{\sqrt{2}\sigma_{\lambda_c}(0)} \right) \right], \\
 \phi_4 &= \frac{\lambda}{\kappa_4} \cdot \frac{\varphi}{\beta_1 + 2(\beta_2 + \beta_3 + \beta_4)} \cdot \left[1 - \operatorname{erf} \left(\frac{\lambda(\kappa_A, 0) - \mu_{\lambda_c}(0)}{\sqrt{2}\sigma_{\lambda_c}(0)} \right) \right] + \frac{w_0}{\kappa_4} \cdot \frac{1}{\beta_1 + 2(\beta_2 + \beta_3 + \beta_4)} \cdot \left[1 - \operatorname{erf} \left(\frac{\lambda(\kappa_A, 0) - \mu_{\lambda_c}(0)}{\sqrt{2}\sigma_{\lambda_c}(0)} \right) \right].
 \end{aligned} \tag{S121}$$

Here, the growth rate is defined as $\lambda(\kappa_A, \phi_Z)$, and $\lambda(\kappa_A, 0)$ is a parameter rather than a variable. Thus, ϕ_i is a linear function of the growth rate λ , with a positive slope and a positive y -intercept. In Fig. 4C-D and Appendix-fig. 3I-J, we show that the model predictions (Eq. S121) agree quantitatively with the experimental data (Basan et al., 2015).

Appendix 5.3 Energy dissipation

In the case of energy dissipation under each nutrient condition, w is perturbed while κ_A is fixed. The relation between protein allocation and growth rate can be obtained by combining Eqs. S28 and S70. However, since w is explicitly present in Eq. S70, we need to reduce this variable to obtain the growth rate dependence of enzyme allocation. In fact, from Eq. S64, we have:

$$\lambda(\kappa_A, w) = \lambda(\kappa_A, 0) \left\{ 1 - \frac{w}{\phi_{\max}} \cdot \left[\frac{1}{\varepsilon_r(\kappa_A)} - \theta(\varepsilon_f(\kappa_A) - \varepsilon_r(\kappa_A)) \cdot \left(\frac{1}{\varepsilon_r(\kappa_A)} - \frac{1}{\varepsilon_f(\kappa_A)} \right) \right] \right\}. \quad (\text{S122})$$

Here, $\lambda(\kappa_A, 0) \equiv \lambda(\kappa_A, w=0)$ (satisfying Eq. S64), which is a parameter rather than a variable. “ θ ” stands for the Heaviside step function. Thus, we have:

$$w(\lambda) = \frac{\phi_{\max} \cdot [1 - \lambda/\lambda(\kappa_A, 0)]}{\left[1/\varepsilon_r(\kappa_A) - \theta(\varepsilon_f(\kappa_A) - \varepsilon_r(\kappa_A)) \cdot (1/\varepsilon_r(\kappa_A) - 1/\varepsilon_f(\kappa_A)) \right]}, \quad (\text{S123})$$

where the energy dissipation coefficient w is regarded as a function of the growth rate.

Combining Eqs. S28, S70 and S123, we get:

$$\left\{ \begin{aligned} \phi_1 &= \frac{1}{2\kappa_1} \left\{ \left[\frac{\varphi \cdot \lambda + w(\lambda)}{\beta_1 + 2(\beta_2 + \beta_6)} - \frac{\varphi \cdot \lambda + w(\lambda)}{\beta_1 + 2(\beta_2 + \beta_3 + \beta_4)} \right] \cdot \left[\operatorname{erf} \left(\frac{\lambda - \mu_{\lambda_c}(0) \left\{ 1 - w/\left[\varepsilon_{r/f}(\kappa_A^{(C)}) \phi_{\max} \right] \right\}}{\sqrt{2}\sigma_{\lambda_c}(0) \left\{ 1 - w/\left[\varepsilon_{r/f}(\kappa_A^{(C)}) \phi_{\max} \right] \right\}} \right) \right] + 1 \right\} + \frac{2[\varphi \cdot \lambda + w(\lambda)]}{\beta_1 + 2(\beta_2 + \beta_3 + \beta_4)} + (\eta_{a2} + \eta_b + 2\eta_c + \eta_d) \cdot \lambda \right\}, \\ \phi_2 &= \frac{1}{\kappa_2} \left\{ \left[\frac{\varphi \cdot \lambda + w(\lambda)}{\beta_1 + 2(\beta_2 + \beta_6)} - \frac{\varphi \cdot \lambda + w(\lambda)}{\beta_1 + 2(\beta_2 + \beta_3 + \beta_4)} \right] \cdot \left[\operatorname{erf} \left(\frac{\lambda - \mu_{\lambda_c}(0) \left\{ 1 - w/\left[\varepsilon_{r/f}(\kappa_A^{(C)}) \phi_{\max} \right] \right\}}{\sqrt{2}\sigma_{\lambda_c}(0) \left\{ 1 - w/\left[\varepsilon_{r/f}(\kappa_A^{(C)}) \phi_{\max} \right] \right\}} \right) \right] + 1 \right\} + \frac{2[\varphi \cdot \lambda + w(\lambda)]}{\beta_1 + 2(\beta_2 + \beta_3 + \beta_4)} + (\eta_b + \eta_c) \cdot \lambda \right\}, \\ \phi_3 &= \frac{1}{\kappa_3} \left\{ \frac{\varphi \cdot \lambda + w(\lambda)}{\beta_1 + 2(\beta_2 + \beta_3 + \beta_4)} \cdot \left[1 - \operatorname{erf} \left(\frac{\lambda - \mu_{\lambda_c}(0) \left\{ 1 - w/\left[\varepsilon_{r/f}(\kappa_A^{(C)}) \phi_{\max} \right] \right\}}{\sqrt{2}\sigma_{\lambda_c}(0) \left\{ 1 - w/\left[\varepsilon_{r/f}(\kappa_A^{(C)}) \phi_{\max} \right] \right\}} \right) \right] + \eta_c \cdot \lambda \right\}, \\ \phi_4 &= \frac{1}{\kappa_4} \cdot \frac{\varphi \cdot \lambda + w(\lambda)}{\beta_1 + 2(\beta_2 + \beta_3 + \beta_4)} \cdot \left[1 - \operatorname{erf} \left(\frac{\lambda - \mu_{\lambda_c}(0) \left\{ 1 - w/\left[\varepsilon_{r/f}(\kappa_A^{(C)}) \phi_{\max} \right] \right\}}{\sqrt{2}\sigma_{\lambda_c}(0) \left\{ 1 - w/\left[\varepsilon_{r/f}(\kappa_A^{(C)}) \phi_{\max} \right] \right\}} \right) \right] \right\}, \end{aligned} \right. \quad (\text{S124})$$

where $w(\lambda)$ follows Eq. S123. When κ_A lies in the vicinity of $\kappa_A^{(C)}$ or w is small so that

$$\left(1 - \frac{w}{\varepsilon_{r/f}(\kappa_A) \cdot \phi_{\max}} \right) \bigg/ \left(1 - \frac{w}{\varepsilon_{r/f}(\kappa_A^{(C)}) \cdot \phi_{\max}} \right) \approx 1, \quad (\text{S125})$$

then we have:

$$\begin{cases} J_f^{(N)}(\lambda, w) = \frac{\varphi \cdot \lambda + w}{\beta_1 + 2(\beta_2 + \beta_6)} \cdot \left[\operatorname{erf} \left(\frac{\lambda(\kappa_A, 0) - \mu_{\lambda_c}(0)}{\sqrt{2}\sigma_{\lambda_c}(0)} \right) + 1 \right], \\ J_r^{(N)}(\lambda, w) = \frac{\varphi \cdot \lambda + w}{\beta_1 + 2(\beta_2 + \beta_3 + \beta_4)} \cdot \left[1 - \operatorname{erf} \left(\frac{\lambda(\kappa_A, 0) - \mu_{\lambda_c}(0)}{\sqrt{2}\sigma_{\lambda_c}(0)} \right) \right], \end{cases} \quad (\text{S126})$$

and thus,

$$\begin{cases} \phi_1 = \frac{1}{2\kappa_1} \left\{ \left[\frac{\varphi \cdot \lambda + w(\lambda)}{\beta_1 + 2(\beta_2 + \beta_6)} - \frac{\varphi \cdot \lambda + w(\lambda)}{\beta_1 + 2(\beta_2 + \beta_3 + \beta_4)} \right] \cdot \left[\operatorname{erf} \left(\frac{\lambda(\kappa_A, 0) - \mu_{\lambda_c}(0)}{\sqrt{2}\sigma_{\lambda_c}(0)} \right) + 1 \right] + \frac{2[\varphi \cdot \lambda + w(\lambda)]}{\beta_1 + 2(\beta_2 + \beta_3 + \beta_4)} + (\eta_{a2} + \eta_b + 2\eta_c + \eta_d) \cdot \lambda \right\}, \\ \phi_2 = \frac{1}{\kappa_2} \left\{ \left[\frac{\varphi \cdot \lambda + w(\lambda)}{\beta_1 + 2(\beta_2 + \beta_6)} - \frac{\varphi \cdot \lambda + w(\lambda)}{\beta_1 + 2(\beta_2 + \beta_3 + \beta_4)} \right] \cdot \left[\operatorname{erf} \left(\frac{\lambda(\kappa_A, 0) - \mu_{\lambda_c}(0)}{\sqrt{2}\sigma_{\lambda_c}(0)} \right) + 1 \right] + \frac{2[\varphi \cdot \lambda + w(\lambda)]}{\beta_1 + 2(\beta_2 + \beta_3 + \beta_4)} + (\eta_b + \eta_c) \cdot \lambda \right\}, \\ \phi_3 = \frac{1}{\kappa_3} \left(\frac{\varphi \cdot \lambda + w(\lambda)}{\beta_1 + 2(\beta_2 + \beta_3 + \beta_4)} \cdot \left[1 - \operatorname{erf} \left(\frac{\lambda(\kappa_A, 0) - \mu_{\lambda_c}(0)}{\sqrt{2}\sigma_{\lambda_c}(0)} \right) \right] + \eta_c \cdot \lambda \right), \\ \phi_4 = \frac{1}{\kappa_4} \cdot \frac{\varphi \cdot \lambda + w(\lambda)}{\beta_1 + 2(\beta_2 + \beta_3 + \beta_4)} \cdot \left[1 - \operatorname{erf} \left(\frac{\lambda(\kappa_A, 0) - \mu_{\lambda_c}(0)}{\sqrt{2}\sigma_{\lambda_c}(0)} \right) \right], \end{cases} \quad (\text{S127})$$

Note that in Eq. S123, w is a linear function of λ with a negative slope. Thus ϕ_i exhibits a linear relation with λ when Eq. S125 is satisfied (see Eq. S127). In fact, the slope of ϕ_4 is surely negative (combining Eqs. S64, S123 and S127), while the slope sign of other ϕ_i depends on parameters. For a given nutrient, the enzymes corresponding to the same ϕ_i should exhibit the same slope sign. Another restriction is that if the slope sign of ϕ_1 is negative, then the slope sign of ϕ_2 is surely negative. In Appendix-fig. 3K-N, we show that our model results agree well with the experimental data (Basan et al., 2015) (Eq. S127).

Appendix 6 Other aspects of the model

Appendix 6.1 A coarse-grained model with more details

To compare with experiments, we consider a coarse-grained model with more details as shown in Appendix-fig. 2F. Here, nodes M_6, M_7 represent GA3P and DHAP, respectively. Other nodes follow the descriptions specified in Appendix 2.1. Each biochemical reaction follows Eq. S5 with $b_i = 1$ except that $M_1 \rightarrow M_6 + M_7$ and $M_3 + M_5 \rightarrow M_4$. By applying flux balance to the stoichiometric fluxes, combined with Eq. S8, we obtain:

$$\left\{ \begin{array}{l} \Phi_A \cdot \xi_A = \Phi_1 \cdot \xi_1 + \Phi_{a1} \cdot \xi_{a1}, \\ \Phi_{11} \cdot \xi_{11} = \Phi_{10} \cdot \xi_{10} + \Phi_1 \cdot \xi_1, \Phi_{10} \cdot \xi_{10} = \Phi_1 \cdot \xi_1, \\ \Phi_{11} \cdot \xi_{11} = \Phi_2 \cdot \xi_2 + \Phi_5 \cdot \xi_5 + \Phi_{a2} \cdot \xi_{a2}, \\ \Phi_2 \cdot \xi_2 = \Phi_3 \cdot \xi_3 + \Phi_6 \cdot \xi_6 + \Phi_b \cdot \xi_b, \\ \Phi_5 \cdot \xi_5 + \Phi_4 \cdot \xi_4 = \Phi_3 \cdot \xi_3 + \Phi_d \cdot \xi_d, \\ \Phi_3 \cdot \xi_3 = \Phi_4 \cdot \xi_4 + \Phi_c \cdot \xi_c. \end{array} \right. \quad (\text{S128})$$

While Eqs. S22-S25 still hold. By applying the substitutions specified in Eqs. S9, S12, S14-S18, combined with Eqs. S4, S10, S22-S25, S128, and the constraint of proteome resource allocation, we get:

$$\left\{ \begin{array}{l} \phi_A \cdot \kappa_A = \phi_1 \cdot \kappa_1 + \phi_{a1} \cdot \kappa_{a1}, \\ \phi_{11} \cdot \kappa_{11} = \phi_{10} \cdot \kappa_{10} + \phi_1 \cdot \kappa_1, \phi_{10} \cdot \kappa_{10} = \phi_1 \cdot \kappa_1, \\ \phi_{11} \cdot \kappa_{11} = \phi_2 \cdot \kappa_2 + \phi_5 \cdot \kappa_5 + \phi_{a2} \cdot \kappa_{a2}, \\ \phi_2 \cdot \kappa_2 = \phi_3 \cdot \kappa_3 + \phi_6 \cdot \kappa_6 + \phi_b \cdot \kappa_b, \\ \phi_5 \cdot \kappa_5 + \phi_4 \cdot \kappa_4 = \phi_3 \cdot \kappa_3 + \phi_d \cdot \kappa_d, \\ \phi_3 \cdot \kappa_3 = \phi_4 \cdot \kappa_4 + \phi_c \cdot \kappa_c, \\ \phi_{a1} \cdot \kappa_{a1} = \eta_{a1} \cdot \lambda, \phi_{a2} \cdot \kappa_{a2} = \eta_{a2} \cdot \lambda, \phi_b \cdot \kappa_b = \eta_b \cdot \lambda, \phi_c \cdot \kappa_c = \eta_c \cdot \lambda, \phi_d \cdot \kappa_d = \eta_d \cdot \lambda, \\ \beta_1 \cdot \phi_1 \cdot \kappa_1 + \beta_2 \cdot \phi_2 \cdot \kappa_2 + \beta_3 \cdot \phi_3 \cdot \kappa_3 + \beta_4 \cdot \phi_4 \cdot \kappa_4 + \beta_6 \cdot \phi_6 \cdot \kappa_6 + \beta_{a1} \cdot \phi_{a1} \cdot \kappa_{a1} = J_E^{(N)}, \\ J_E^{(N)} = \eta_E \cdot \lambda, \lambda = \phi_R \cdot \kappa_r, J_r^{(N)} = \phi_4 \cdot \kappa_4, J_f^{(N)} = \phi_6 \cdot \kappa_6, \\ \phi_R + \phi_A + \phi_1 + \phi_2 + \phi_3 + \phi_4 + \phi_5 + \phi_6 + \phi_7 + \phi_8 + \phi_{a1} + \phi_{a2} + \phi_b + \phi_c + \phi_d = \phi_{\max}. \end{array} \right. \quad (\text{S129})$$

Then, Eq. S28 still hold, while ϕ_{10} and ϕ_{11} are:

$$\left\{ \begin{array}{l} \phi_{10} = \left[J_r^{(N)} + J_f^{(N)} + (\eta_{a2} + \eta_b + 2\eta_c + \eta_d) \lambda \right] / (2 \cdot \kappa_{10}), \\ \phi_{11} = \left[J_r^{(N)} + J_f^{(N)} + (\eta_{a2} + \eta_b + 2\eta_c + \eta_d) \lambda \right] / \kappa_{11}. \end{array} \right. \quad (\text{S130})$$

By substituting Eqs. S28 and S130 into Eq. S129, we get:

$$\left\{ \begin{array}{l} J_r^{(E)} + J_f^{(E)} = \varphi \cdot \lambda, \\ \frac{J_r^{(E)}}{\mathcal{E}_r^{(\text{dt})}} + \frac{J_f^{(E)}}{\mathcal{E}_f^{(\text{dt})}} = \phi_{\max} - \psi_{\text{dt}} \cdot \lambda, \end{array} \right. \quad (\text{S131})$$

where “dt” stands for details. Eqs. S30 and S33 still hold. $\mathcal{E}_r^{(\text{dt})}$ and $\mathcal{E}_f^{(\text{dt})}$ represent the proteome energy efficiencies of respiration and fermentation, respectively, with

$$\begin{cases} \mathcal{E}_r^{(\text{dt})} = \frac{\beta_1/2 + \beta_2 + \beta_3 + \beta_4}{1/(2\kappa_A) + 1/(2\kappa_1) + 1/(2\kappa_{10}) + 1/\kappa_{11} + 1/\kappa_2 + 1/\kappa_3 + 1/\kappa_4}, \\ \mathcal{E}_f^{(\text{dt})} = \frac{\beta_1/2 + \beta_2 + \beta_6}{1/(2\kappa_A) + 1/(2\kappa_1) + 1/(2\kappa_{10}) + 1/\kappa_{11} + 1/\kappa_2 + 1/\kappa_6}. \end{cases} \quad (\text{S132})$$

ψ_{dt}^{-1} is the proteome efficiency of biomass pathway, with

$$\psi_{\text{dt}} = \frac{1}{\kappa_t} + \frac{1 + \eta_{a1} + \eta_c}{2\kappa_A} + (\eta_{a2} + \eta_b + 2\eta_c + \eta_d) \left(\frac{1}{2\kappa_1} + \frac{1}{2\kappa_{10}} + \frac{1}{\kappa_{11}} \right) + \frac{\eta_b + \eta_c}{\kappa_2} + \frac{\eta_c}{\kappa_3} + \frac{\eta_c + \eta_d}{\kappa_5} + \sum_i^{a1,a2,b,c,d} \frac{\eta_i}{\kappa_i}. \quad (\text{S133})$$

Appendix 6.2 Estimation of the in vivo enzyme catalytic rates

We use the method introduced by Davidi *et al.* (Davidi et al., 2016), combined with proteome experimental data (Basan et al., 2015) (Appendix-table 2), to estimate the in vivo enzyme catalytic rates. Combining Eqs. S28 and S130, we have:

$$\begin{cases} \kappa_1 = \left[J_r^{(\text{N})} + J_f^{(\text{N})} + (\eta_{a2} + \eta_b + 2\eta_c + \eta_d) \lambda \right] / (2 \cdot \phi_1), \\ \kappa_2 = \left[J_r^{(\text{N})} + J_f^{(\text{N})} + (\eta_b + \eta_c) \lambda \right] / \phi_2, \\ \kappa_3 = (J_r^{(\text{N})} + \eta_c \cdot \lambda) / \phi_3, \kappa_4 = J_r^{(\text{N})} / \phi_4, \\ \kappa_5 = (\eta_c + \eta_d) \lambda / \phi_5, \kappa_6 = J_f^{(\text{N})} / \phi_6, \\ \kappa_{10} = \left[J_r^{(\text{N})} + J_f^{(\text{N})} + (\eta_{a2} + \eta_b + 2\eta_c + \eta_d) \lambda \right] / (2 \cdot \phi_{10}), \\ \kappa_{11} = \left[J_r^{(\text{N})} + J_f^{(\text{N})} + (\eta_{a2} + \eta_b + 2\eta_c + \eta_d) \lambda \right] / \phi_{11}. \end{cases} \quad (\text{S134})$$

Here, $J_r^{(\text{N})}$, $J_f^{(\text{N})}$, λ and ϕ_i ($i=1-6,10-11$) are measurable from experiments (see Appendix 8.1 and Appendix-table 2). Thus, we can obtain the in vivo values of κ_i from Eq. S134. Combined with Eqs. S17 and S20, we have

$$k_i^{\text{cat}} = \frac{r_{\text{carbon}}}{r_{\text{protein}}} \cdot \frac{m_{E_i}}{m_{\text{carbon}}} \cdot \kappa_i \cdot \left[\sum_i r_i / N_{\text{EP}_i}^{\text{carbon}} \right]. \quad (\text{S135})$$

Eq. S135 is the in vivo result for the enzyme catalytic rate. In Appendix-fig. 2G, we show a comparison between in vivo and in intro results for k_{cat} values of enzymes within glycolysis and the TCA cycle, which are roughly consistent. In the applications, we prioritized the use of in vivo results for enzyme catalytic rates, and use in intro data as a substitute when there were vacancies.

Appendix 6.3 Comparison with existing models that illustrate experimental results

For the coarse-grained model described in Appendix 2, the normalized stoichiometric influx of a Group A carbon source is given by:

$$J_{in}^{(N)} \equiv J_A^{(N)} = \phi_A \cdot \kappa_A. \quad (S136)$$

Combined with the first equation in Eq. S28, we obtain:

$$J_{in}^{(N)} - \mathcal{G} \cdot \lambda = \frac{J_r^{(E)}}{e_r} + \frac{J_f^{(E)}}{e_f}, \quad (S137)$$

where $e_r = \beta_1 + 2(\beta_2 + \beta_3 + \beta_4)$, $e_f = \beta_1 + 2(\beta_2 + \beta_6)$, and $\mathcal{G} = \eta_{a1} + \eta_c + (\eta_{a2} + \eta_b + \eta_d)/2$.

Evidently, e_r , e_f and \mathcal{G} are constant parameters. In this subsection, we highlight the major differences between our model presented in Appendix 2 and existing models that may illustrate the growth rate dependence of fermentation flux in the standard picture (Basan et al., 2015; Holms, 1996; Meyer et al., 1984; Nanchen et al., 2006) of overflow metabolism.

Based on the modeling principles rather than the detailed mechanisms, there are two major classes of existing models that can illustrate experimental results. In fact, both classes of models regard the proteome energy efficiencies ε_r and ε_f as constants, with $\varepsilon_f > \varepsilon_r$ if used, or follow functionally equivalent propositions. In our model, however, ε_r and ε_f are both functions of κ_A , which vary significantly upon nutrient perturbation, where $\varepsilon_r(\kappa_A \rightarrow 0) > \varepsilon_f(\kappa_A \rightarrow 0)$ and $\varepsilon_r(\kappa_A^{\max}) < \varepsilon_f(\kappa_A^{\max})$ (see Eqs. S38, S40-S41). Furthermore, there are significant differences in the modeling/optimization principles, as listed below.

The first class of models (Chen and Nielsen, 2019; Majewski and Domach, 1990; Niebel et al., 2019; Shlomi et al., 2011; Varma and Palsson, 1994; Vazquez et al., 2010; Vazquez and Oltvai, 2016) optimize the ratio of biomass outflow to carbon influx: $\lambda/J_{in}^{(N)}$. Either to optimize the growth rate for a given carbon influx, or to minimize the carbon influx for a given growth rate. Since respiration is far more efficient than fermentation in terms of the energy production per unit carbon, to optimize the ratio $\lambda/J_{in}^{(N)}$, cells would preferentially use respiration when the carbon influx is small. As carbon influx increases above a certain threshold, factors such as proteome allocation direct cells towards fermentation in an analog way since they consider $\varepsilon_f > \varepsilon_r$. Our model is significantly different from this class of models in the optimization principle, where we purely optimize the cell growth rate for a given nutrient condition, without any further constraints on the carbon influx.

The second class of models, represented by Basan *et al.* (Basan et al., 2015), also adopt the optimization of $\lambda/J_{in}^{(N)}$ in the interpretation of their model results. However, the growth rate dependence of fermentation flux was derived prior to the application of growth rate optimization. In fact, Eqs. S29 and S137 in our model are very similar form to Basan *et al.* (Basan et al., 2015),

yet there are critical differences as we list below. In Eq. S29, by regarding $J_r^{(E)}$ and $J_f^{(E)}$ as the two variables in a system of linear equations, we obtain the following expressions:

$$\begin{cases} J_r^{(E)} = \frac{\phi_{\max} - (\psi + \varphi/\varepsilon_f) \cdot \lambda}{1/\varepsilon_r - 1/\varepsilon_f}, \\ J_f^{(E)} = \frac{(\psi + \varphi/\varepsilon_r) \cdot \lambda - \phi_{\max}}{1/\varepsilon_r - 1/\varepsilon_f}. \end{cases} \quad (\text{S138})$$

In Basan *et al.* (Basan et al., 2015), Eq. S138 is considered to be the relation between $J_{r/f}^{(E)}$ and λ upon nutrient (and thus $J_{in}^{(N)}$) perturbation, while ε_r and ε_f are regarded as constants through the perturbation. By contrast, in our model, Eq. S138 is the constraint under a given nutrient condition with fixed κ_A , yet not relevant to nutrient perturbation. For wild-type strains, if $\varepsilon_r(\kappa_A) > \varepsilon_f(\kappa_A)$ (or vice versa), then the optimal solution is $J_r^{(E)}(\kappa_A) = \varphi \cdot \lambda(\kappa_A)$ and $J_f^{(E)}(\kappa_A) = 0$, with $\lambda(\kappa_A) = \frac{\varepsilon_r(\kappa_A) \cdot \phi_{\max}}{\varphi + \varepsilon_r(\kappa_A) \cdot \psi(\kappa_A)}$. This solution (which satisfies Eq. S138) corresponds to a point rather than a line in the relation between $J_{r/f}^{(E)}$ and λ upon κ_A perturbation.

Appendix 6.4 Explanation of the Warburg effect in tumor cells

Our model and analysis shown in Appendix 2 can be naturally extended to explain the Warburg effect in tumor cell metabolism with the following modifications in the model settings. In the applications for tumor cell metabolism, the fermentation flux changes from acetate secretion rate into the lactate secretion rate, and thus the stoichiometric coefficients (β_i) for ATP production change accordingly. Consequently, in the coarse-grained model shown in Fig. 1B, M_3 stands for pyruvate, and β_2, β_6 change into $\beta_2 = 1, \beta_6 = -2$ (Nelson et al., 2008).

Evidently, Eqs. S37-S38 still hold. As long as $\varepsilon_r(\kappa_A^{\max}) < \varepsilon_f(\kappa_A^{\max})$ (Eq. S40), then there exists a critical switching point for κ_A (denoted as $\kappa_A^{(C)}$, see Eq. S41), below which the respiration pathway is more efficient, while above $\kappa_A^{(C)}$, the fermentation pathway is more efficient in the proteome energy production. To maximize proliferation rate, the tumor cells would preferentially use the respiration pathway upon starvation while use the aerobic glycolysis pathway with abundant nutrient (Warburg effect). Based on the facts that the rate of glucose metabolism is 10-100 times faster in aerobic glycolysis than that of respiration (Liberti and Locasale, 2016), and oncogenes induce Warburg effect intrinsically to promote cell proliferation (Hanahan and Weinberg, 2011; Liberti and Locasale, 2016), it is suggested that $\varepsilon_r(\kappa_A^{\max}) < \varepsilon_f(\kappa_A^{\max})$. Thus, the

aerobic glycolysis with abundant nutrients provides a fitness advantage for tumor cell proliferation.

Appendix 7 Probability density functions of variables and parameters

Appendix 7.1 Probability density function of κ_i

Enzyme catalysis is crucial for the survival of living organisms, as it can significantly accelerate the rate of a biochemical reaction by moderating the energy barrier between the substrate and product (Nelson et al., 2008). However, the maximal turnover rate of enzymes, k_{cat} values, vary notably between the in vivo and in vitro measurements (Davidi et al., 2016). Recent studies suggest that differences in the aquatic medium should be the causes (Davidi et al., 2016; García-Contreras et al., 2012). In particular, the concentrations of potassium and phosphate have a big influence on k_{cat} (García-Contreras et al., 2012), which possess a certain degree of variation among the cell populations under intracellular conditions (García-Contreras et al., 2012). For simplicity, we assume that the turnover rate of each E_i enzyme k_i^{cat} follows a Gaussian distribution $\mathcal{N}(\mu_{k_i^{\text{cat}}}, \sigma_{k_i^{\text{cat}}}^2)$ with $k_i^{\text{cat}} > 0$ among cells (extrinsic noise (Elowitz et al., 2002), denoted as η_{ext}), and then the probability density function of k_i^{cat} is given by:

$$k_i^{\text{cat}} \sim \mathcal{N}(x, \mu_{k_i^{\text{cat}}}, \sigma_{k_i^{\text{cat}}}^2) = \begin{cases} \frac{1}{\sigma_{k_i^{\text{cat}}} \sqrt{2\pi}} e^{-\frac{1}{2} \left(\frac{x - \mu_{k_i^{\text{cat}}}}{\sigma_{k_i^{\text{cat}}}} \right)^2}, & x \geq 0. \\ 0, & x < 0. \end{cases} \quad (\text{S139})$$

When the CV of the k_i^{cat} distribution (i.e., $\sigma_{k_i^{\text{cat}}} / \mu_{k_i^{\text{cat}}}$) is less than 1/3, $\mathcal{N}(x, \mu_{k_i^{\text{cat}}}, \sigma_{k_i^{\text{cat}}}^2)$ is almost identical to $\mathcal{N}(\mu_{k_i^{\text{cat}}}, \sigma_{k_i^{\text{cat}}}^2)$. In this regard, $1/k_i^{\text{cat}}$ follows the positive inverse of Gaussian distribution (IOG), and the probability density function is:

$$\text{IOG}(x, \mu_{1/k_i^{\text{cat}}}, \zeta_{1/k_i^{\text{cat}}}) = \begin{cases} \sqrt{\frac{\zeta_{1/k_i^{\text{cat}}}}{2\pi x^4}} \exp\left(-\frac{1}{2} \frac{\zeta_{1/k_i^{\text{cat}}} (x - \mu_{1/k_i^{\text{cat}}})^2}{x^2 \mu_{1/k_i^{\text{cat}}}^2}\right), & x \geq 0, \\ 0, & x < 0, \end{cases} \quad (\text{S140})$$

where $\zeta_{1/k_i^{\text{cat}}} = 1/\sigma_{k_i^{\text{cat}}}^2$ and $\mu_{1/k_i^{\text{cat}}} = 1/\mu_{k_i^{\text{cat}}}$.

Meanwhile, due to the stochastic nature of biochemical reactions, we apply Gillespie's chemical Langevin equation (Gillespie, 2000) to account for the intrinsic noise (Elowitz et al., 2002) (denoted as η_{int}). For cell size regulation of *E. coli* within a cell cycle, the cell mass at initiation of DNA per chromosome origin remains constant (Donachie, 1968). Thus, the duration

of enzyme E_i to finish a catalytic job (with a timescale of $1/k_i^{\text{cat}}$) can be approximated as the first passage time of a stochastic process, with

$$\begin{cases} X_i(t=0) = 0, \\ dX_i/dt = \alpha_i + \sqrt{\alpha_i} \Gamma_i(t), \\ T_\Theta = \inf\{t > 0 \mid X_i(t) = \Theta\}. \end{cases} \quad (\text{S141})$$

Here $\alpha_i \equiv k_i^{\text{cat}} \cdot \Theta$, Θ is proportional to the cell volume, and $\Gamma_i(t)$ is the independent temporally uncorrelated Gaussian white noise. Then, for a given value of k_i^{cat} , the first passage time T_Θ follows an Inverse Gaussian distribution (IG) (Folks and Chhikara, 1978):

$$\text{IG}\left(x, \mu'_{1/k_i^{\text{cat}}}, \zeta'_{1/k_i^{\text{cat}}}\right) = \begin{cases} \sqrt{\frac{\zeta'_{1/k_i^{\text{cat}}}}{2\pi x^3}} \exp\left(-\frac{1}{2} \frac{\zeta'_{1/k_i^{\text{cat}}} \left(x - \mu'_{1/k_i^{\text{cat}}}\right)^2}{x \mu'^2_{1/k_i^{\text{cat}}}}\right), & x \geq 0, \\ 0, & x < 0, \end{cases} \quad (\text{S142})$$

where $\mu'_{1/k_i^{\text{cat}}} = 1/k_i^{\text{cat}}$, $\zeta'_{1/k_i^{\text{cat}}} = \Theta/k_i^{\text{cat}}$, and the variance is $\sigma'^2_{1/k_i^{\text{cat}}} \equiv \mu'^3_{1/k_i^{\text{cat}}} / \zeta'_{1/k_i^{\text{cat}}} = 1/\left[\Theta \cdot \left(k_i^{\text{cat}}\right)^2\right]$.

Thus, we can obtain the CV:

$$\sigma'_{1/k_i^{\text{cat}}} / \mu'_{1/k_i^{\text{cat}}} = \Theta^{-\frac{1}{2}}, \quad (\text{S143})$$

which is inversely scaled with the square root of cell volume. Evidently, the intrinsic and extrinsic noise make orthogonal contributions to the total noise (Elowitz et al., 2002) (denoted as η_{tot}):

$$\eta_{\text{tot}}^2 = \eta_{\text{int}}^2 + \eta_{\text{ext}}^2. \quad (\text{S144})$$

In fact, when the CV is small (i.e., $\text{CV} \ll 1$), both IOG and IG distributions converge into Gaussian distributions (Appendix-fig. 4). In the back-of-the-envelope calculations, we approximate x in all the denominator terms of $\text{IOG}(x, \mu, \zeta)$ and $\text{IG}(x, \mu, \zeta)$ as μ (since $\text{CV} \ll 1$). Then, both IOG and IG distributions can be approximated as follows:

$$\text{IOG}\left(x, \mu_{1/k_i^{\text{cat}}}, \zeta_{1/k_i^{\text{cat}}}\right) \xrightarrow{\text{CV} \ll 1} \mathcal{N}\left(\mu_{1/k_i^{\text{cat}}}, \sigma^2_{1/k_i^{\text{cat}}}\right), \quad (\text{S145})$$

with $\sigma^2_{1/k_i^{\text{cat}}} = \mu^4_{1/k_i^{\text{cat}}} / \zeta_{1/k_i^{\text{cat}}}$, and

$$\text{IG}\left(x, \mu'_{1/k_i^{\text{cat}}}, \zeta'_{1/k_i^{\text{cat}}}\right) \xrightarrow{\text{CV} \ll 1} \mathcal{N}\left(\mu'_{1/k_i^{\text{cat}}}, \sigma'^2_{1/k_i^{\text{cat}}}\right), \quad (\text{S146})$$

with $\sigma_{1/k_i^{\text{cat}}}^2 = \mu_{1/k_i^{\text{cat}}}^3 / \zeta'_{1/k_i^{\text{cat}}}$. Rigorously, we show below that $\text{IG}(x, \mu, \zeta)$ shrinks to be $\mathcal{N}(\mu, \mu^3/\zeta)$ when the CV is small. Here, the characteristic function of the variable x is (Folks and Chhikara, 1978; Van Kampen, 1992):

$$G(k) = \int_{-\infty}^{\infty} e^{ikx} \cdot \text{IG}(x, \mu, \zeta) dx = \exp \left\{ \frac{\zeta}{\mu} \left[1 - \sqrt{1 - \frac{2i\mu^2 k}{\zeta}} \right] \right\}, \quad (\text{S147})$$

and thus,

$$\text{IG}(x, \mu, \zeta) = \frac{1}{2\pi} \int_{-\infty}^{\infty} e^{-ikx} \cdot G(k) dk. \quad (\text{S148})$$

When the variance $\sigma^2 \equiv \mu^3/\zeta$ is very small, basically, we require $2\mu^2 k/\zeta = 2\sigma^2 k/\mu \ll 1$, and

then $\sqrt{1 - \frac{2i\mu^2 k}{\zeta}} \approx 1 - \frac{\mu^2}{\zeta} ki + \frac{\mu^4}{2\zeta^2} k^2$. Thus,

$$\begin{cases} G(k) \approx \exp \left(\mu ki - \frac{\mu^3}{2\zeta} k^2 \right), \\ \text{IG}(x, \mu, \zeta) \approx \sqrt{\frac{\zeta}{2\pi\mu^3}} e^{-\frac{\zeta(x-\mu)^2}{2\mu^3}} = \mathcal{N}(\mu, \mu^3/\zeta). \end{cases} \quad (\text{S149})$$

Then, we have:

$$\lim_{\sigma \rightarrow 0} \text{IG}(x, \mu, \zeta) = \mathcal{N}(\mu, \mu^3/\zeta). \quad (\text{S150})$$

In fact, although intrinsic noise affects the short-term measurement of enzyme catalytic rate and growth rate at the single-cell level, its contribution in the long-term is negligible. Thus, we approximate $\eta_{\text{tot}} \approx \eta_{\text{ext}}$. Combined with Eqs. S145-S146, it is easy to check that $1/k_i^{\text{cat}}$ shares roughly identical CV as k_i^{cat} :

$$\sigma_{1/k_i^{\text{cat}}} / \mu_{1/k_i^{\text{cat}}} = \sigma_{k_i^{\text{cat}}} / \mu_{k_i^{\text{cat}}}. \quad (\text{S151})$$

For convenience, in the model analysis, we approximate both IOG and IG distributions as Gaussian distributions. Then, all $1/k_i^{\text{cat}}$ are normally distributed independent random variables following Gaussian distributions:

$$1/k_i^{\text{cat}} \sim \mathcal{N}(\mu_{1/k_i^{\text{cat}}}, \sigma_{1/k_i^{\text{cat}}}^2). \quad (\text{S152})$$

Using the properties of Gaussian distributions, for a series of constant real numbers γ_i , the summation of $\gamma_i/k_i^{\text{cat}}$, where we defined it as $\Xi \equiv \sum_{i=1}^n \gamma_i/k_i^{\text{cat}}$, follows a Gaussian distribution (Van Kampen, 1992):

$$\Xi \sim \mathcal{N}(\mu_{\Xi}, \sigma_{\Xi}^2), \quad (\text{S153})$$

with $\mu_{\Xi} = \sum_{i=1}^n \gamma_i \mu_{1/k_i^{\text{cat}}}$ and $\sigma_{\Xi}^2 = \sum_{i=1}^n (\gamma_i \sigma_{1/k_i^{\text{cat}}})^2$. The relation between κ_i and k_i^{cat} is shown in Eq. S12. To optimize growth rate, each κ_i of the intermediate nodes satisfies Eq. S20, while κ_A satisfies Eq. S27. Thus, for a given nutrient condition ($[A]$ is fixed), all the ratios $k_i^{\text{cat}}/\kappa_i$ are constants. Combined with Eqs. S139, S145-S146, S152, then, the distributions of all κ_i and $1/\kappa_i$ can be approximated as Gaussian distributions:

$$\begin{cases} \kappa_i \sim \mathcal{N}(\mu_{\kappa_i}, \sigma_{\kappa_i}^2), \\ 1/\kappa_i \sim \mathcal{N}(\mu_{1/\kappa_i}, \sigma_{1/\kappa_i}^2), \end{cases} \quad (\text{S154})$$

where μ_{κ_i} and μ_{1/κ_i} are the means of κ_i and $1/\kappa_i$, while σ_{κ_i} and σ_{1/κ_i} are their standard deviations. Using the properties of Gaussian distributions combined with Eq. S31, S32, S36, S42-S43, S145-S146 and S153, then ε_r , ε_f , ψ , λ_r , λ_f , $\kappa_A^{(C)}$ and λ_c also roughly follow Gaussian distributions.

Appendix 7.2 Probability density function of the growth rate λ

From Appendix 7.1, we note that λ_r and λ_f (see Eq. S36) roughly follow Gaussian distributions, with

$$\begin{cases} \lambda_r \sim \mathcal{N}(\mu_{\lambda_r}, \sigma_{\lambda_r}^2), \\ \lambda_f \sim \mathcal{N}(\mu_{\lambda_f}, \sigma_{\lambda_f}^2), \end{cases} \quad (\text{S155})$$

where $\mu_{\lambda_{r/f}}$ and $\sigma_{\lambda_{r/f}}$ represent the mean and standard deviation, respectively. We further assume that the correlation between λ_r and λ_f is ρ_{rf} . From Eq. S36, we see that the growth rate λ takes the maximum of λ_r and λ_f , i.e.,

$$\lambda = \max(\lambda_r, \lambda_f). \quad (\text{S156})$$

Then, the cumulative distribution function of λ is $P(\lambda \leq x) = \int_{-\infty}^x \int_{-\infty}^x f(x_1, x_2) dx_1 dx_2$, where

$$f(x_1, x_2) = \frac{(1 - \rho_{rf}^2)^{-\frac{1}{2}}}{2\pi\sigma_{\lambda_r}\sigma_{\lambda_f}} \exp \left(-\frac{1}{2(1 - \rho_{rf}^2)} \left[\left(\frac{x_1 - \mu_{\lambda_r}}{\sigma_{\lambda_r}} \right)^2 - 2\rho_{rf} \left(\frac{x_1 - \mu_{\lambda_r}}{\sigma_{\lambda_r}} \right) \left(\frac{x_2 - \mu_{\lambda_f}}{\sigma_{\lambda_f}} \right) + \left(\frac{x_2 - \mu_{\lambda_f}}{\sigma_{\lambda_f}} \right)^2 \right] \right).$$

Thus, the probability density function of the growth rate λ is given by:

$$f_\lambda(x) = \frac{1}{2\sqrt{2\pi}\sigma_{\lambda_r}} e^{-\frac{1}{2}\left(\frac{x - \mu_{\lambda_r}}{\sigma_{\lambda_r}}\right)^2} \left[\operatorname{erf} \left(\frac{(x - \mu_{\lambda_r})\sigma_{\lambda_r} - \rho_{rf}\sigma_{\lambda_f}(x - \mu_{\lambda_r})}{\sigma_{\lambda_r}\sigma_{\lambda_f}\sqrt{2(1 - \rho_{rf}^2)}} \right) + 1 \right] + \frac{1}{2\sqrt{2\pi}\sigma_{\lambda_f}} e^{-\frac{1}{2}\left(\frac{x - \mu_{\lambda_f}}{\sigma_{\lambda_f}}\right)^2} \left[\operatorname{erf} \left(\frac{(x - \mu_{\lambda_r})\sigma_{\lambda_r} - \rho_{rf}\sigma_{\lambda_f}(x - \mu_{\lambda_r})}{\sigma_{\lambda_r}\sigma_{\lambda_f}\sqrt{2(1 - \rho_{rf}^2)}} \right) + 1 \right]. \quad (\text{S157})$$

In Appendix-fig. 2B, we show that Eq. S157 quantitatively illustrates the experimental data of *E. coli* under the relevant conditions.

Appendix 8 Model comparison with experiments

Appendix 8.1 Flux comparison with experiments

In Appendix 6.2, we see that the values of $J_f^{(N)}$ and $J_r^{(N)}$ are required to calculate the in vivo enzyme catalytic rates of the intermediate nodes. Here, we use J_{acetate} and $J_{\text{CO}_2, r}$ to represent the stoichiometric fluxes of acetate from the fermentation pathway and CO₂ from the respiration pathway, respectively. Combined with the stoichiometric coefficients of both pathways, we have:

$$\begin{cases} J_{\text{acetate}} = J_f, \\ J_{\text{CO}_2, r} = 3 \cdot J_r. \end{cases} \quad (\text{S158})$$

By further combining with Eqs. S16-S17, we get:

$$\begin{cases} J_f^{(N)} = J_{\text{acetate}} \cdot \frac{m_{\text{carbon}}}{M_{\text{carbon}}} \cdot \left[\sum_i r_i / N_{\text{EP}_i}^{\text{carbon}} \right]^{-1}, \\ J_r^{(N)} = \frac{1}{3} \cdot J_{\text{CO}_2, r} \cdot \frac{m_{\text{carbon}}}{M_{\text{carbon}}} \cdot \left[\sum_i r_i / N_{\text{EP}_i}^{\text{carbon}} \right]^{-1}. \end{cases} \quad (\text{S159})$$

In fact, the values of J_{acetate} and $J_{\text{CO}_2, r}$ scale with the mass of the “big cell”, which increases over time. In experiments, the measurable fluxes are typically expressed in the unit of mM/OD₆₀₀/h (Basan et al., 2015). Thus, we define $J_{\text{acetate}}^{(M)}$ and $J_{\text{CO}_2, r}^{(M)}$ as the fluxes of J_{acetate} and $J_{\text{CO}_2, r}$ in the unit of mM/OD₆₀₀/h, respectively. The superscript “(M)” represents the measurable flux in this unit. For *E. coli*, we use the following biochemical data collected from published literature: 1 OD₆₀₀ roughly corresponds to 6×10^8 cells/mL (Stevenson et al., 2016), the average mass of a cell is 1pg (Milo and Phillips, 2015), the biomass percentage of the cell weight is 30% (Neidhardt et al., 1990), the molar mass of carbon is 12g (Nelson et al., 2008), $r_{\text{carbon}} = 0.48$

(Neidhardt et al., 1990) and $r_{\text{protein}} = 0.55$ (Neidhardt et al., 1990). Combined with the values of r_i (see Appendix 1.2) and $N_{\text{EP}_i}^{\text{carbon}}$, where $N_{\text{EP}_{a1}}^{\text{carbon}} = 6$, $N_{\text{EP}_{a2}}^{\text{carbon}} = 3$, $N_{\text{EP}_b}^{\text{carbon}} = 3$, $N_{\text{EP}_c}^{\text{carbon}} = 5$, and $N_{\text{EP}_d}^{\text{carbon}} = 4$ (Nelson et al., 2008), we have:

$$\begin{cases} J_f^{(N)} \approx J_{\text{acetate}}^{(M)} / 2, \\ J_r^{(N)} \approx J_{\text{CO}_2, r}^{(M)} / 6. \end{cases} \quad (\text{S160})$$

From Eq. S18, we obtain the values of η_i for each precursor pool : $\eta_{a1} = 0.15$, $\eta_{a2} = 0.30$, $\eta_b = 0.35$, $\eta_c = 0.09$, $\eta_d = 0.11$. Still, the value of η_E is required to compare the growth rate dependence of fermentation/respiration fluxes between model results and experiments, which we will specify in Appendix 8.2.

Appendix 8.2 Model parameter settings using experimental data

We have collected biochemical data of *E. coli* shown in Appendix-tables 1-2 to set the model parameters. This includes the molecular weight (MW) and in vitro k_{cat} values of the catalytic enzymes, as well as the proteome and flux data used to calculate the in vivo turnover numbers. To reduce measurement noise, we take the average rather than the maximum value of in vivo k_{cat} from calculations with data from four cultures (see Appendix-table 2). Here, we prioritize the use of in vivo k_{cat} wherever applicable unless there is a vacancy (see Appendix-table 1).

Note that our models are coarse grained. For example, the flux J_3 shown in Fig. 1B actually corresponds to three different reactions in the metabolic network (see Fig. 1A and Appendix-table 1), which we label as $J_3^{(i)}$ ($i = 1, 2, 3$). For each $J_3^{(i)}$, there are corresponding variables/parameters of $\Phi_3^{(i)}$, $\xi_3^{(i)}$, $\phi_3^{(i)}$, $\kappa_3^{(i)}$ satisfying Eqs. S8, S9 and S12. Evidently, $J_3^{(i)} = J_3$ ($i = 1, 2, 3$), and it is straightforward to derive the following relation between $\kappa_3^{(i)}$ and κ_3 :

$$1/\kappa_3 = \sum_{i=1}^3 1/\kappa_3^{(i)}. \quad (\text{S161})$$

In fact, Eq. S161 can be generalized to determine the values of other κ_i in the coarse-grained models combined with the biochemical data. For the coarse-grained model of Group A carbon source utilization shown in Fig. 1B, we have the values for parameters κ_i ($i = 1, \dots, 6$), and then $\varepsilon_r(\kappa_A^{(C)}) = 122 \text{ (h}^{-1}\text{)}$. Evidently, $\varepsilon_r(\kappa_{\text{glucose}}^{(\text{ST})}) < \varepsilon_f(\kappa_{\text{glucose}}^{(\text{ST})})$, $\varepsilon_r(\kappa_{\text{lactose}}^{(\text{ST})}) < \varepsilon_f(\kappa_{\text{lactose}}^{(\text{ST})})$, and thus $\varepsilon_r(\kappa_A^{\text{max}}) < \varepsilon_f(\kappa_A^{\text{max}})$. For pyruvate, we have $\varepsilon_{r/f}^{(\text{py})}(\kappa_{\text{py}}^{(C)}) = \varepsilon_{r/f}(\kappa_A^{(C)}) = 122 \text{ (h}^{-1}\text{)}$ (see Eqs. S43 and S101), and it is easy to check that $\varepsilon_r(\kappa_{\text{py}}^{(\text{ST})}) < \varepsilon_f(\kappa_{\text{py}}^{(\text{ST})})$.

For the remaining model parameters, note that we have classified the inactive ribosomal-affiliated proteins into the Q-class, and then $\phi_{\text{max}} = 48\%$ (Scott et al., 2010). The values of κ_i is

obtainable from experiments: the translational speed is 20.1aa/s (Scott et al., 2010), with 7336 amino acids per ribosome (Neidhardt, 1996) and $\zeta \approx 1.67$ (Neidhardt, 1996; Scott et al., 2010) (see Appendix 1.1), hence $\kappa_t = 1/610$ (s^{-1}). However, there are insufficient data to determine the values of κ_i ($i = a1, a2, b, c, d$) from the entry point metabolites to the precursor pools. Basically, it involves many steps, and thus these values should be considerably large. Here, we lump sum the contributions of κ_t and κ_i ($i = a1, a2, b, c, d$) by defining a composite parameter:

$$\Omega \equiv 1/\kappa_t + \sum_i^{a1,a2,b,c,d} \eta_i/\kappa_i. \quad (S162)$$

We proceed to estimate the values of Ω and φ using experimental data (Basan et al., 2015) for wild-type strains on the $J_{\text{acetate}}^{(M)}$ - λ relation (Fig. 1C), and then all the rest of model parameters are set accordingly.

For the case of $w_0 = 0$, where all k_{cat} values follow a Gaussian distribution with an extrinsic noise of 25% CV, which is the general setting we use unless otherwise specified, then $\varphi = 10.8$ and $\Omega = 1345$ (s). Accordingly, we have $\eta_E = 14.78$, $\mu_{\lambda_c} = 0.92$ (h^{-1}), and $\sigma_{\lambda_c} = 0.12\mu_{\lambda_c}$, where the CV of the extrinsic noise for Ω is estimated using the averaged CV of other κ_i . For the translation inhibition effect of Cm, we estimate the values for ι as $\iota_{w_0=0}^{(2\mu\text{m Cm})} = 1.15$, $\iota_{w_0=0}^{(4\mu\text{m Cm})} = 2.33$, $\iota_{w_0=0}^{(8\mu\text{m Cm})} = 6.25$, where the superscript stands for the concentration of Cm, and the subscript represents the choice of w_0 .

For pyruvate, with the value of η_E , we get $\varphi_{\text{py}} = 14.82$. However, there is still a lack of proteome data to determine the value of κ_9 , which actually involves many steps in the metabolic network and thus can be considerably large. Here we define another composite parameter $\Omega'_{\text{Gg}} \equiv (\eta_b + \eta_c)/\kappa_8 + \eta_{a1}/\kappa_9$ and estimate its value as $\Omega'_{\text{Gg}} = 690$ (s) from the growth rate data for *E. coli* measured under the relevant nutrient conditions (Basan et al., 2015), where the subscript “Gg” stands for glucogenesis. Then, $\mu_{\lambda_c^{(\text{py})}} = 0.67$ (h^{-1}), and $\sigma_{\lambda_c^{(\text{py})}} = 0.10\mu_{\lambda_c^{(\text{py})}}$, where the same CV of extrinsic noise for Ω applies to Ω'_{Gg} .

For the case of a Group A carbon source mixed with 21 amino acids (21AA, with saturated concentrations), then $\varphi_{21\text{AA}} = 14.2$. Comparing Eq. S32 with Eq. S112, the parameter Ω should change to $\Omega_{21\text{AA}} \equiv 1/\kappa_t + \eta_{a1}/\kappa_{a1} + \sum_i^{a2,b,c,d} \eta_i/\kappa_i^{(21\text{AA})}$. Obviously, $1/\kappa_t < \Omega_{21\text{AA}} < \Omega$, and we estimate $\Omega_{21\text{AA}} = 1000$ (s) from the growth rate data for *E. coli* measured under the relevant

nutrient conditions (Wallden et al., 2016). Then, we have $\mu_{\lambda_c^{(21AA)}} = 1.13 \text{ (h}^{-1}\text{)}$, and $\sigma_{\lambda_c^{(21AA)}} = 0.12\mu_{\lambda_c^{(21AA)}}$.

For the case of a Group A carbon source mixed with 7 amino acids (7AA: His, Iso, Leu, Lys, Met, Phe, and Val), similar to the roles of φ_{21AA} and Ω_{21AA} , we define φ_{7AA} and Ω_{7AA} . Using the mass fraction of the 7AA combined with Eq. S18, we have $\varphi_{7AA} = 11.6$. For the value of Ω_{7AA} , evidently, $\Omega_{21AA} < \Omega_{7AA} < \Omega$, and we estimate $\Omega_{7AA} = 1215 \text{ (s)}$ from the growth rate data for *E. coli* measured under the relevant culture media (Basan et al., 2015). Then, $\mu_{\lambda_c^{(7AA)}} = 0.98 \text{ (h}^{-1}\text{)}$, and $\sigma_{\lambda_c^{(21AA)}} = 0.12\mu_{\lambda_c^{(21AA)}}$.

For the case of $w_0 = 2.5 \text{ (h}^{-1}\text{)}$, we have $\varphi = 8.3$, and thus $\eta_E = 12.28$, while other parameters such as Ω , μ_{λ_c} and σ_{λ_c} remain the same values as for $w_0 = 0$. Nevertheless, the values for ι upon translation inhibition with Cm are influenced by the choice of w_0 , where the values of ι change into $\iota_{w_0=2.5}^{(2\mu\text{M Cm})} = 1.05$, $\iota_{w_0=2.5}^{(4\mu\text{M Cm})} = 2.00$, $\iota_{w_0=2.5}^{(8\mu\text{M Cm})} = 5.40$.

From Appendix 7.1-7.2, combined with Eq. S114, the distributions of $\lambda_r^{(21AA)}$ and $\lambda_f^{(21AA)}$ can be approximated by Gaussian distributions:

$$\begin{cases} \lambda_r^{(21AA)} \sim \mathcal{N}\left(\mu_{\lambda_r^{(21AA)}}, \sigma_{\lambda_r^{(21AA)}}^2\right), \\ \lambda_f^{(21AA)} \sim \mathcal{N}\left(\mu_{\lambda_f^{(21AA)}}, \sigma_{\lambda_f^{(21AA)}}^2\right), \end{cases} \quad (\text{S163})$$

where $\mu_{\lambda_r^{(21AA)}}$ and $\mu_{\lambda_f^{(21AA)}}$ stand for the mean values, while $\sigma_{\lambda_r^{(21AA)}}$ and $\sigma_{\lambda_f^{(21AA)}}$ represent the standard deviations. For the case of glucose mixed with 21AA (labeled as ‘‘Glucose+21AA’’), the distribution of the growth rate $\lambda_{\text{glucose}}^{(21AA)}$ follows Eq. S157. With $\Omega_{21AA} = 1000 \text{ (s)}$, we have $\mu_{\lambda_{\text{glucose},r}^{(21AA)}} = 1.34 \text{ (h}^{-1}\text{)}$, $\mu_{\lambda_{\text{glucose},f}^{(21AA)}} = 1.46 \text{ (h}^{-1}\text{)}$ (both definitions follow Eq. S163), and $\rho_{rf} \approx 1.0$ (obtained with numerical results).

For the case of succinate mixed with 21AA (labeled as ‘‘Succinate+21AA’’), the respiration pathway is always more efficient since succinate lies within the TCA cycle, then the cell growth rate (defined as $\lambda_{\text{succinate}}^{(21AA)}$) would just take the value of the respiration one and thus follows a Gaussian distribution:

$$\lambda_{\text{succinate}}^{(21AA)} \sim \mathcal{N}\left(\mu_{\lambda_{\text{succinate}}^{(21AA)}}, \sigma_{\lambda_{\text{succinate}}^{(21AA)}}^2\right). \quad (\text{S164})$$

For the case that acetate is the sole carbon source, evidently, the cells only use the respiration pathway, and thus the growth rate (defined as λ_{acetate}) follows a Gaussian distribution:

$$\lambda_{\text{acetate}} \sim \mathcal{N}(\mu_{\lambda_{\text{acetate}}}, \sigma_{\lambda_{\text{acetate}}}^2). \quad (\text{S165})$$

With the measured growth rate data (Wallden et al., 2016), we estimate $\mu_{\lambda_{\text{succinate}}^{(21\text{AA})}} = 0.67 \text{ (h}^{-1}\text{)}$ and $\mu_{\lambda_{\text{acetate}}} = 0.253 \text{ (h}^{-1}\text{)}$. To illustrate the distribution of growth rates $\lambda_{\text{glucose}}^{(21\text{AA})}$, $\lambda_{\text{succinate}}^{(21\text{AA})}$ and λ_{acetate} shown in Appendix-fig. 2B, if there was no other source of noise, extrinsic noise with a CV of 40% would be required for each k_{cat} value. Then, $\sigma_{\lambda_{\text{glucose}, r}^{(21\text{AA})}} \approx 0.21\mu_{\lambda_{\text{glucose}, r}^{(21\text{AA})}}$, $\sigma_{\lambda_{\text{glucose}, f}^{(21\text{AA})}} \approx 0.23\mu_{\lambda_{\text{glucose}, f}^{(21\text{AA})}}$, $\sigma_{\lambda_{\text{succinate}}^{(21\text{AA})}} = 0.22\mu_{\lambda_{\text{succinate}}^{(21\text{AA})}}$, and $\sigma_{\lambda_{\text{acetate}}} = 0.22\mu_{\lambda_{\text{acetate}}}$. Allowing for that intrinsic noise may also play a non-negligible role for the observed single-cell growth rate (which is not a long-term average), we still use extrinsic noise with a CV of 25% other than those shown in Appendix-fig. 2B.

Appendix 8.3 Notes on the application of reference data

Data calibration: Throughout our manuscript, we use experimental data from the original references except for two calibrations. The first calibration is shown in the footnote to Appendix-table 2. With this calibration, the $J_{\text{acetate}}^{(M)}$ - λ data (Basan et al., 2015) in Appendix-table 2 align with the curve shown in Fig. 1C, which includes experimental data from other sources. The second calibration is for the data shown in Figs. 3F and 1C (chemostat data). The unit in the original reference (Holms, 1996) is mmol/(dry mass)g/h. To convert this into the unit mM/OD₆₀₀/h applied in our text, the conversion factor should be 0.18. Here, we deduce that only 60% of the measured dry biomass in centrifuged material is effective to calibrate with other experimental results. Therefore, there is a calibration factor of 0.6, and the conversion factor changes into 0.3.

Data of the inducible strains: We note that part of the experiment data in the original references (Basan et al., 2015; Hui et al., 2015) were obtained using strains with titratable systems (e.g. titratable ptsG, LacY). Basically, the $J_{\text{acetate}}^{(M)}$ - λ relation of these inducible strains align with the same curve as that of the wild-type *E.coli* (Fig. 1C). Given that evolution treatment is not involved for the inducible strain, we regard the titration perturbation as a technique to fool the strains. That is, these inducible strains behave as if they were cultured in a less efficient Group A carbon source.

Experimental data sources: The batch culture data shown in Fig. 1C (labeled with minimum/rich media or inducible strains) and Appendix-fig. 2C were taken from the source data of the reference's figure 1 (Basan et al., 2015). The chemostat data shown in Fig. 1C were taken from the reference's table 7 (Holms, 1996). The data shown in Fig. 1D were taken from the

reference's extended data figure 3a (Basan et al., 2015) with the calibration specified in the footnote to Appendix-table 2.

The data shown in Fig. 2A were adopted from the reference's extended data figure 4a-b (Basan et al., 2015). The data shown in Fig. 2B were taken from the source data of the reference's figure 2a (Basan et al., 2015). The data shown in Fig. 2C were taken from the source data of the reference's figure 3a (Basan et al., 2015). The data shown in Fig. 3A-B were taken from the source data of the reference's figure 3d (Basan et al., 2015).

The data shown in Fig. 3C-D and Appendix-fig. 2D-E were taken from the source data of the reference's figure 3c (Basan et al., 2015). The data shown in Fig. 3F were taken from the reference's table 7 (Holms, 1996), with a calibration factor specified in the above paragraph ("Data calibration").

The data shown in Fig. 4A-B and Appendix-fig. 3A-D were taken from the reference's table S2 with the label "C-lim" (Hui et al., 2015). We excluded the reference's data with $\lambda = 0.45205$ (h^{-1}) as there are other unconsidered factors involved during slow growth (Dai et al., 2016) (for $\lambda < 0.5 \text{ h}^{-1}$), and we suspect that there may be unknown calibration factors. The data shown in Fig. 4C-D and Appendix-fig. 3E-N were adopted from the reference's extended data figure 6-7 (Basan et al., 2015).

The gene names depicted in Appendix-fig. 1B were identified using KEGG database. The data shown in Appendix-fig. 2G were drawn from Appendix-table 1, which includes the original references themselves. The flux data presented in Appendix-table 2 were obtained from the reference's extended data figure 3a (Basan et al., 2015), with the calibration specified in the footnote. The proteome data shown in Appendix-table 2 were taken from the reference's supplementary Table N5 (Basan et al., 2015).

Appendix Tables

Appendix-table 1. Molecular weight (MW) and in vivo/ in vitro k_{cat} data for *E. coli*.

No.*	Reaction	Enzyme	Gene name	EC	MW (kDa)	In vitro k_{cat} (s ⁻¹)	References	In vivo† k_{cat} (s ⁻¹)	Chosen k_{cat} (s ⁻¹)
J_1	Glucose-6P \leftrightarrow Fructose-6P	Glucose-6-phosphate isomerase	pgi	EC:5.3.1.9	1.2 \times 10 ²	2.6 \times 10 ²	PMID: 7004378; DOI:10.1016/j.jms.2004.09.017	8.7 \times 10 ²	8.7 \times 10 ²
	Fructose-6P \rightarrow Fructose-1,6P	Phosphofructokinase	pfkA‡	EC:2.7.1.11	1.4 \times 10 ²	4.4 \times 10 ²	PMID: 6218375; 70226	1.7 \times 10 ³	1.7 \times 10 ³
	Fructose-1,6P \leftrightarrow Glyceraldehyde 3-phosphate+Dihydroxyacetone phosphate	Fructose-bisphosphate aldolase	fbaA‡	EC:4.1.2.13	7.8 \times 10	1.4 \times 10	PMID: 8939754; 15531627	1.6 \times 10 ²	1.6 \times 10 ²
	Dihydroxyacetone phosphate \leftrightarrow Glyceraldehyde 3-phosphate	Triosephosphate Isomerase	tpiA	EC:5.3.1.1	5.4 \times 10	4.3 \times 10 ²	PMID: 3887397; 6092857	2.7 \times 10 ²	2.7 \times 10 ²
	Glyceraldehyde 3-phosphate \rightarrow 1,3-Bisphosphoglycerate	Glyceraldehyde-3-phosphate dehydrogenase	gapA	EC:1.2.1.12	1.4 \times 10 ²	9.5 \times 10	PMID: 4932978; 2200929	1.5 \times 10 ²	1.5 \times 10 ²
	1,3-Bisphosphoglycerate \leftrightarrow 3-Phosphoglycerate	Phosphoglycerate kinase	pgk	EC:2.7.2.3	4.4 \times 10	3.5 \times 10 ²	PMID: 367367; 166274	1.9 \times 10 ²	1.9 \times 10 ²
	3-Phosphoglycerate \leftrightarrow 2-Phosphoglycerate	Phosphoglycerate mutase	gpmA‡	EC:5.4.2.11	4.9 \times 10	3.3 \times 10 ²	PMID: 10437801	4.5 \times 10 ²	4.5 \times 10 ²
	2-Phosphoglycerate \leftrightarrow Phosphoenolpyruvate	Enolase	eno	EC:4.2.1.11	9.0 \times 10	2.2 \times 10 ²	PMID: 1094232; 4942326	1.7 \times 10 ²	1.7 \times 10 ²
J_2	Phosphoenolpyruvate \rightarrow Pyruvate	Pyruvate kinase	pykF‡	EC:2.7.1.40	2.4 \times 10 ²	5.0 \times 10 ²	PMID: 6759852	1.6 \times 10 ³	1.6 \times 10 ³
	Pyruvate \rightarrow Acetyl-CoA	Pyruvate dehydrogenase	aceE‡	EC:1.2.4.1	1.0 \times 10 ²	1.2 \times 10 ²	PMID: 23088422	3.4 \times 10 ²	3.4 \times 10 ²
J_3	Oxaloacetate +Acetyl-CoA \rightarrow Citrate	Citrate synthase	gltA	EC:2.3.3.1	9.7 \times 10	2.4 \times 10 ²	PMID: 4900996; 23954305	7.1 \times 10	7.1 \times 10
	Citrate \leftrightarrow Isocitrate	Aconitate hydratase	acnB‡	EC:4.2.1.3	9.4 \times 10	7.0 \times 10	PMID:15963579; 12473114	6.3 \times 10	6.3 \times 10
	Isocitrate \rightarrow α -Ketoglutarate	Isocitrate dehydrogenase	icd	EC:1.1.1.42	9.5 \times 10	2.0 \times 10 ²	PMID: 8141; 36923; 2200929	3.3 \times 10	3.3 \times 10
J_4	α -Ketoglutarate \rightarrow Succinyl-CoA	α -Ketoglutarate dehydrogenase complex E1 component	suc A suc B‡	EC:1.2.4.2, EC:2.3.1.61	1.9 \times 10 ²	1.5 \times 10 ²	PMID: 6380583; 4588679	1.3 \times 10 ²	1.3 \times 10 ²
	Succinyl-CoA \leftrightarrow Succinate	Succinyl-CoA synthetase	suc C suc D	EC:6.2.1.5	1.6 \times 10 ²	9.1 \times 10	PMID: 5338130	1.0 \times 10 ²	1.0 \times 10 ²
	Succinate \rightarrow Fumarate	Succinate dehydrogenase	sdh A sdh B‡	EC:1.3.5.1	1.0 \times 10 ²	1.1 \times 10 ²	PMID: 4334990; 16484232	1.1 \times 10 ²	1.1 \times 10 ²
	Fumarate \leftrightarrow Malate	Fumarase	fumA‡	EC:4.2.1.2	2.0 \times 10 ²	1.2 \times 10 ³	PMID: 3282546; 12021453	4.9 \times 10 ²	4.9 \times 10 ²
	Malate \leftrightarrow Oxaloacetate	Malate dehydrogenase	mdh	EC:1.1.1.37	6.1 \times 10	5.5 \times 10 ²	doi:10.1016/0076-6879 (69) 13029-3	6.6 \times 10	6.6 \times 10
J_5	Phosphoenolpyruvate \rightarrow Oxaloacetate	Phosphoenolpyruvate carboxylase	ppc	EC:4.1.1.31	4.0 \times 10 ²	1.5 \times 10 ²	PMID: 9927652; 4932977	/	1.5 \times 10 ²
J_6	Acetyl-CoA \leftrightarrow Acetyl phosphate	Phosphate acetyltransferase	pta	EC:2.3.1.8	7.7 \times 10	3.0 \times 10	PMID:20236319	3.7 \times 10 ²	3.7 \times 10 ²
	Acetyl phosphate \leftrightarrow Acetate	Acetate kinase	ackA	EC:2.7.2.1	4.3 \times 10	3.6 \times 10 ³	EcoCyc: EG10027; PMID: 24801996	3.3 \times 10 ²	3.3 \times 10 ²
	Acetate (intracellular) \leftrightarrow Acetate (extracellular)	Acetate transporter	actP	/	2 \times 10	4.7 \times 10 ²	PMID: 31405984 (Estimated)	/	4.7 \times 10 ²
J_7	Pyruvate \rightarrow Phosphoenolpyruvate	Pyruvate, water dikinase	ppsA	EC:2.7.9.2	2.5 \times 10 ²	3.5 \times 10	PMID: 4319237	/	3.5 \times 10

J_A	Glucose-6P (extracellular) → Glucose-6P (intracellular)	Glucose-6- phosphate transporter	UhpT	/	5×10	2×10^2	PMID: 3283129; 2197272; 20018695 (Estimated)	/	2×10^2
	Glucose (extracellular) → Glucose-6P	Glucose-specific PTS enzyme	ptsG	EC: 2.7.1.199	5×10	1×10^2	PMID: 9575173; 20018695; 12146972	/	1×10^2
	Lactose (extracellular) → Lactose (intracellular)	Lactose transporter	lacY	/	4.6×10	6×10	PMID: 6444453; 20018695	/	6×10
	Lactose → Glucose + Galactose	β -galactosidase	lacZ	EC:3.2.1.23	4.6×10^2	6.4×10^2	PMID: 8008071; 23011886 (Estimated)	/	6.4×10^2
J_{py}	Pyruvate (extracellular) → Pyruvate (intracellular)	Pyruvate transporter	btsT CstA	/	8×10	6×10	PMID:20018695; 33260635; EcoCyc: G7942; EG10167 (Estimated)	/	6×10

* The classification of J_i follows the coarse-grained models shown in Figs. 1B and 3E.

† In vivo k_{cat} values were obtained using experimental data shown in Appendix-table 2 combined with Eqs. S134-S135.

‡ See Appendix-fig. 1B for more genes that may play a secondary role.

Appendix-table 2. Proteome and flux data(Basan et al., 2015) used to calculate the in vivo k_{cat} .

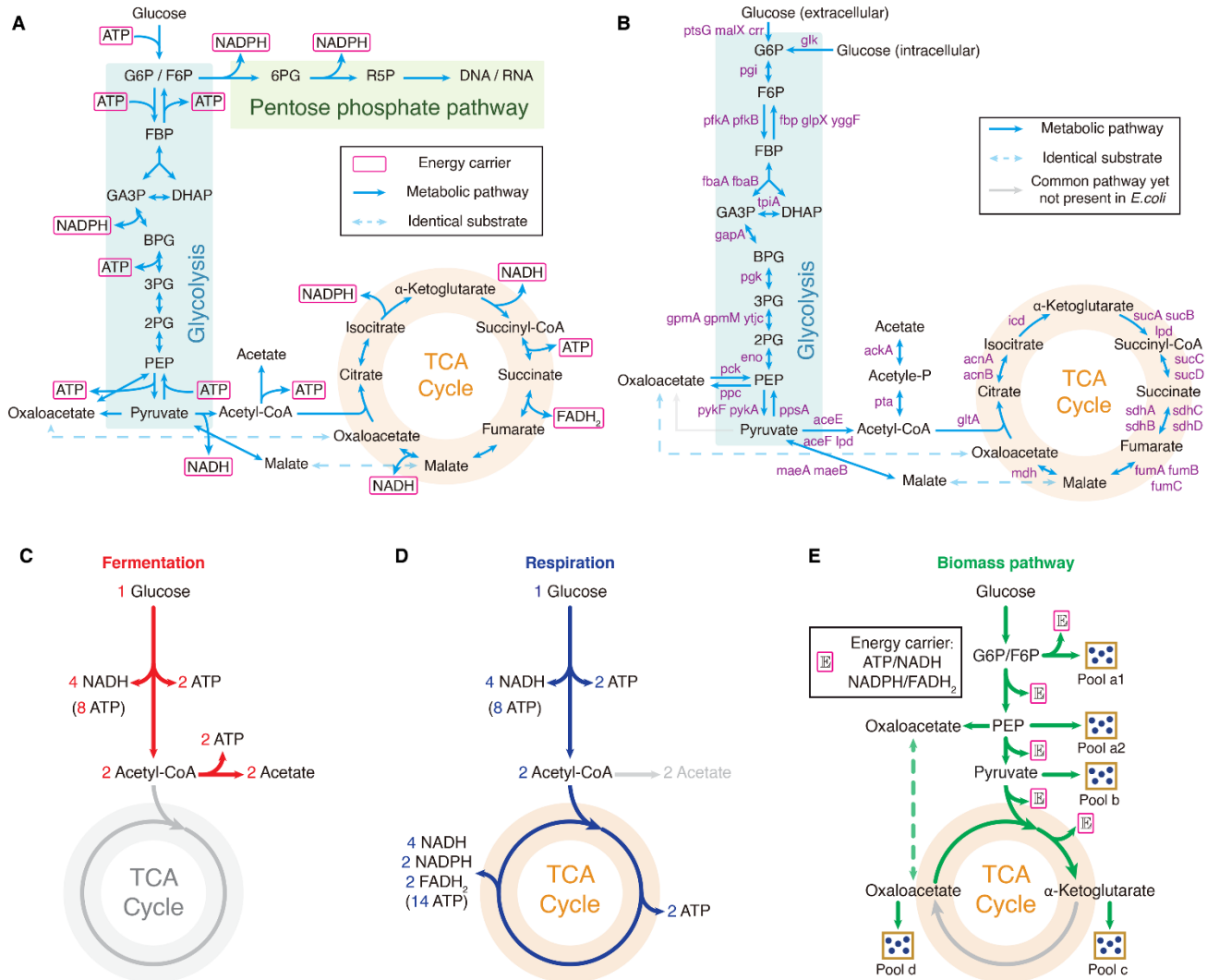
	Culture 1	Culture 2	Culture 3	Culture 4
Growth rate λ (h^{-1}) *	0.82	0.87	0.97	1.03
J_{acetate} ($\text{mM OD}_{600}^{-1} \text{h}^{-1}$) †	0.39	1.18	2.68	2.84
$J_{\text{CO}_2, r}$ ($\text{mM OD}_{600}^{-1} \text{h}^{-1}$) †	7.44	6.05	4.30	3.04
Gene name	Protein fractions obtained using absolute abundance (ϕ_i)			
pgi	0.09%	0.09%	0.10%	0.11%
pfkA	0.06%	0.06%	0.06%	0.06%
fbaA	0.32%	0.35%	0.35%	0.39%
tpiA	0.12%	0.15%	0.13%	0.18%
gapA	1.19%	1.29%	1.33%	1.47%
pgk	0.30%	0.31%	0.32%	0.36%
gpmA	0.15%	0.15%	0.15%	0.16%
eno	0.63%	0.70%	0.75%	0.83%
pykF	0.15%	0.15%	0.18%	0.21%
aceE	0.30%	0.32%	0.34%	0.41%
gltA	0.88%	0.80%	0.61%	0.48%
acnB	0.92%	0.84%	0.66%	0.57%
icd	1.55%	1.55%	1.31%	1.39%
suc A suc B	0.71%	0.75%	0.64%	0.55%
suc C suc D	0.88%	0.84%	0.66%	0.52%
sdh A sdh B	0.49%	0.45%	0.42%	0.35%
fumA	0.24%	0.21%	0.17%	0.13%
mdh	0.45%	0.45%	0.41%	0.39%
pta	0.10%	0.10%	0.10%	0.10%
ackA	0.06%	0.07%	0.06%	0.06%

* For calibration purposes, a factor of 1.03/0.97 was multiplied on the reference data (Basan et al., 2015)‡.

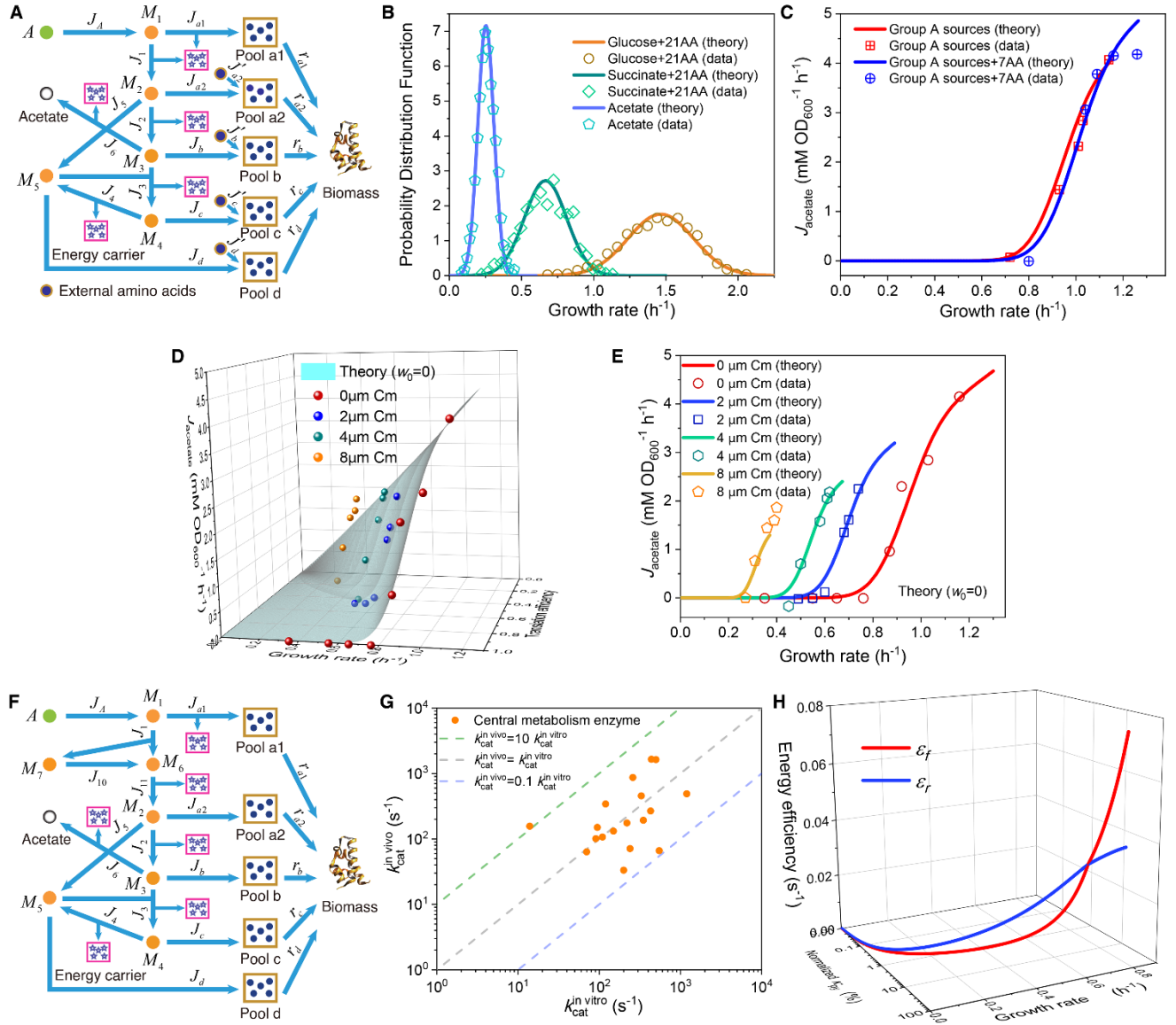
† For calibration purposes, a factor of 2.84/3.24 was multiplied on the reference data (Basan et al., 2015)‡.

‡ Here, (1.03, 2.84) and (0.97, 3.24) are both the data of (λ (h^{-1}), J_{acetate} ($\text{mM OD}_{600}^{-1} \text{h}^{-1}$)) for *E. coli* strain NCM3722 cultured with lactose in the same reference (Basan et al., 2015). The former is specified in the source data of the reference's figure 1 (Basan et al., 2015), while the latter is recorded in the reference's extended data figure 3a (Basan et al., 2015). With the calibrations above, the data for the $J_{\text{acetate}}^{(M)} - \lambda$ relation shown here align with the curve depicted in Fig. 1C.

Appendix Figures

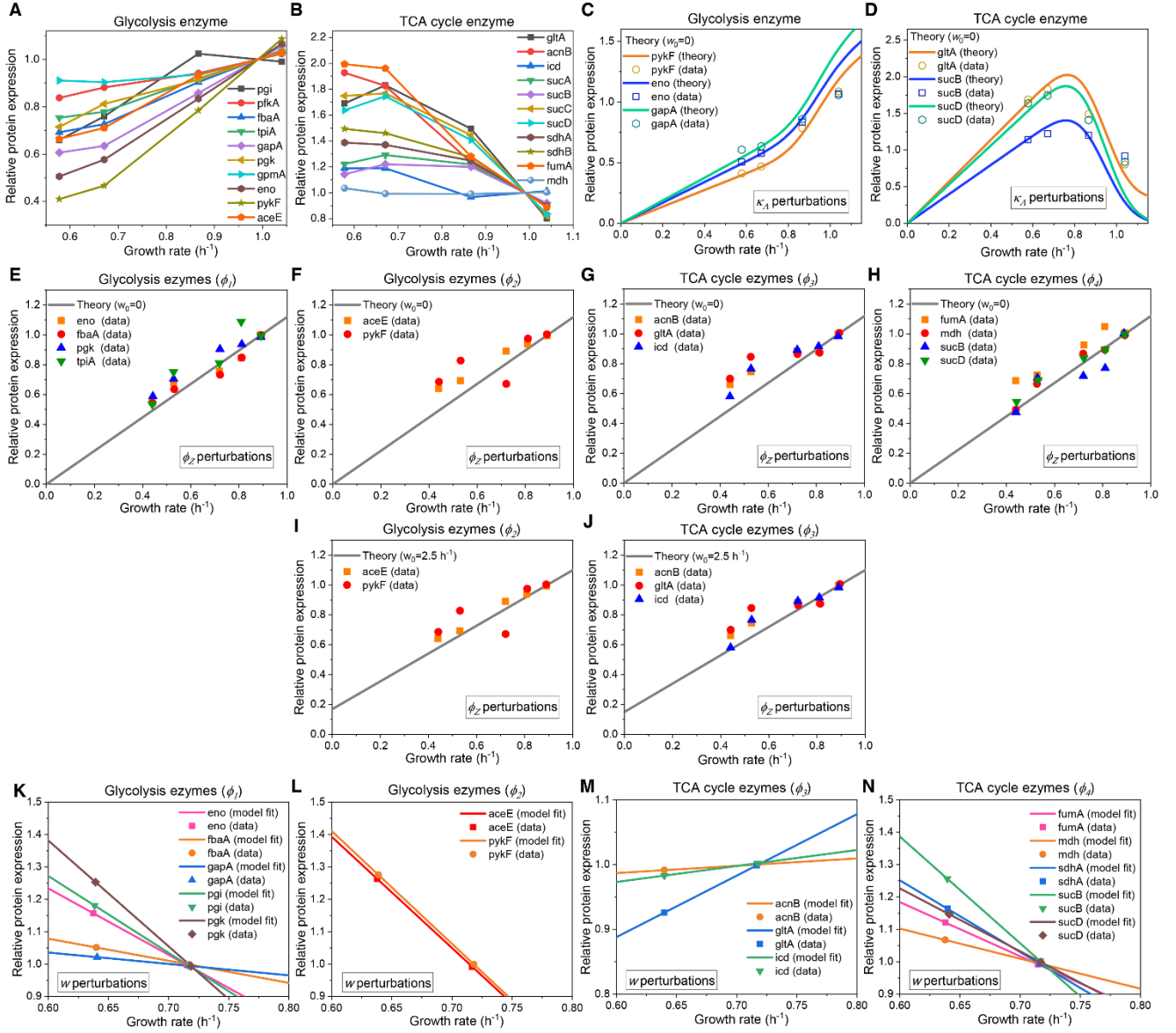


Appendix-figure 1. Central metabolic network and carbon utilization pathways. (A) Energy production details of the central metabolic network. In *E. coli*, NADPH and NADH are interconvertible (Sauer et al., 2004), and all energy carriers can be converted to ATP with ADP. The conversion factors are: NADH = 2ATP, NADPH = 2ATP, FADH₂ = 1ATP (Neidhardt et al., 1990). **(B)** Relevant genes for enzymes in the central metabolic network. **(C-E)** Three destinies of glucose metabolism. **(C)** Fermentation pathway, where a molecule of glucose generates 12 ATPs in *E. coli*. **(D)** Respiration pathway, where a molecule of glucose generates 26 ATPs. **(E)** Biomass pathway, where glucose turns into precursors of biomass. Note that the process of biomass generation is accompanied by ATPs production (see Appendix 2.1).



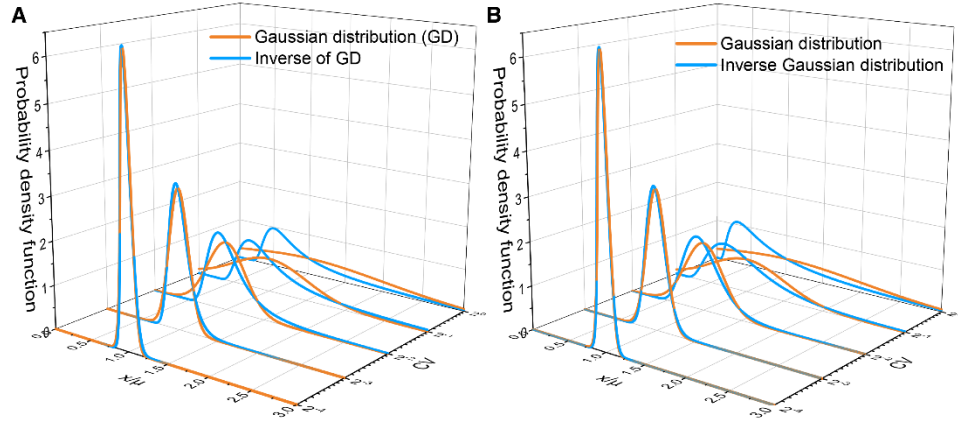
Appendix-figure 2. Model and results for experimental comparison. (A-C) Model analysis for carbon utilization in mixtures with amino acids. (A) Coarse-grained model for the case of a Group A carbon source mixed with extracellular amino acids. (B) Model predictions (Eqs. S157, S164-S165) and single-cell reference experimental results (Wallden et al., 2016) of the growth rate distributions for *E. coli* in three culturing conditions. (C) Comparison of the growth rate-fermentation flux relation for *E. coli* in Group A carbon sources between minimum media and enriched media (those with 7AA). (D-E) Influence of translation inhibition on overflow metabolism. (D) A 3D plot of the relations among the fermentation flux, growth rate, and the translation efficiency (Eqs. 79 and S160). (E) Growth rate dependence of acetate excretion rate as κ_A varies, with each fixed dose of Cm. The translation efficiency is tuned by the dose of Cm, and the maintenance energy coefficient is set to be 0 (i.e., $w_0 = 0$). (F) The coarse-grained model for Group A carbon source utilization. This model includes more details to compare with

experiments. **(G)** Comparison of the in vivo and in vitro catalytic rates for enzymes within glycolysis and the TCA cycle (see Appendix-table 1 for details). **(H)** The energy efficiencies of respiration and fermentation pathways vary with growth rate as functions of the substrate quality of pyruvate (Eqs. S93 and S96).



Appendix-figure 3. Relative protein expression of central metabolic enzymes under various types of perturbations. (A-D) Relative protein expression under κ_A perturbation. (A) Experimental data (Hui et al., 2015) of the catalytic enzymes for each step of glycolysis. (B) Experimental data (Hui et al., 2015) of the catalytic enzymes for each step of the TCA cycle. (C) Model predictions (Eq. S118, with $w_0 = 0$) and experimental data (Hui et al., 2015) of representative genes from glycolysis. (D) Model predictions (Eq. S118, with $w_0 = 0$) and experimental data (Hui et al., 2015) of representative genes from the TCA cycle. (E-J) Relative protein expression under ϕ_Z perturbation. (E, F, I) Model predictions and experimental data (Basan et al., 2015) of representative genes from glycolysis. (G, H, J) Model predictions and experimental data (Basan et al., 2015) of representative genes from the TCA cycle. (E-H) Results of ϕ_Z perturbation with $w_0 = 0$ (Eq. S120). (I-J) Results of ϕ_Z perturbation with

$w_0 = 2.5 \text{ (h}^{-1}\text{)}$ (Eq. S121). **(K-N)** Relative protein expression upon energy dissipation. **(K-L)** Model fits (Eqs. S127 and S123) and experimental data (Basan et al., 2015) of representative genes from glycolysis. **(M-N)** Model fits (Eqs. S127 and S123) and experimental data (Basan et al., 2015) of representative genes from the TCA cycle.



Appendix-figure 4. Asymptotic distributions of inverse Gaussian distribution and the inverse of Gaussian distribution. (A) Comparison between the inverse of Gaussian distribution and the corresponding Gaussian distribution for each value of coefficient of variation (CV) (Eqs. S140 and S145). (B) Comparison between the inverse Gaussian distribution and the corresponding Gaussian distribution for each value of CV (Eqs. S142 and S146). Both inverse Gaussian distribution and the inverse of Gaussian distribution converge to Gaussian distributions when CV is small.

Appendix References

- Basan, M., Honda, T., Christodoulou, D., Hörl, M., Chang, Y.-F., Leoncini, E., Mukherjee, A., Okano, H., Taylor, B.R., Silverman, J.M., et al. (2020). A universal trade-off between growth and lag in fluctuating environments. *Nature* 584, 470-474.
- Basan, M., Hui, S., Okano, H., Zhang, Z., Shen, Y., Williamson, J.R., and Hwa, T. (2015). Overflow metabolism in *Escherichia coli* results from efficient proteome allocation. *Nature* 528, 99-104.
- Bennett, B.D., Kimball, E.H., Gao, M., Osterhout, R., Van Dien, S.J., and Rabinowitz, J.D. (2009). Absolute metabolite concentrations and implied enzyme active site occupancy in *Escherichia coli*. *Nature Chemical Biology* 5, 593-599.
- Chen, Y., and Nielsen, J. (2019). Energy metabolism controls phenotypes by protein efficiency and allocation. *Proceedings of the National Academy of Sciences* 116, 17592-17597.
- Dai, X., Zhu, M., Warren, M., Balakrishnan, R., Patsalo, V., Okano, H., Williamson, J.R., Fredrick, K., Wang, Y.-P., and Hwa, T. (2016). Reduction of translating ribosomes enables *Escherichia coli* to maintain elongation rates during slow growth. *Nature Microbiology* 2, 1-9.
- Davidi, D., Noor, E., Liebermeister, W., Bar-Even, A., Flamholz, A., Tummler, K., Barenholz, U., Goldenfeld, M., Shlomi, T., and Milo, R. (2016). Global characterization of in vivo enzyme catalytic rates and their correspondence to in vitro kcat measurements. *Proceedings of the National Academy of Sciences* 113, 3401-3406.
- Donachie, W.D. (1968). Relationship between cell size and time of initiation of DNA replication. *Nature* 219, 1077-1079.
- Elowitz, M.B., Levine, A.J., Siggia, E.D., and Swain, P.S. (2002). Stochastic gene expression in a single cell. *Science* 297, 1183-1186.
- Folks, J.L., and Chhikara, R.S. (1978). The inverse Gaussian distribution and its statistical application—a review. *Journal of the Royal Statistical Society: Series B* 40, 263-275.
- García-Contreras, R., Vos, P., Westerhoff, H.V., and Boogerd, F.C. (2012). Why in vivo may not equal in vitro—new effectors revealed by measurement of enzymatic activities under the same in vivo-like assay conditions. *The FEBS Journal* 279, 4145-4159.
- Gillespie, D.T. (2000). The chemical Langevin equation. *The Journal of Chemical Physics* 113, 297-306.
- Hanahan, D., and Weinberg, R.A. (2011). Hallmarks of cancer: the next generation. *Cell* 144, 646-674.
- Holms, H. (1996). Flux analysis and control of the central metabolic pathways in *Escherichia coli*. *FEMS Microbiology Reviews* 19, 85-116.
- Hui, S., Silverman, J.M., Chen, S.S., Erickson, D.W., Basan, M., Wang, J., Hwa, T., and Williamson, J.R. (2015). Quantitative proteomic analysis reveals a simple strategy of global resource allocation in bacteria. *Molecular Systems Biology* 11, 784.
- Kussell, E., and Leibler, S. (2005). Phenotypic diversity, population growth, and information in fluctuating environments. *Science* 309, 2075-2078.

Liberti, M.V., and Locasale, J.W. (2016). The Warburg effect: how does it benefit cancer cells? *Trends in Biochemical Sciences* 41, 211-218.

Majewski, R., and Domach, M. (1990). Simple constrained-optimization view of acetate overflow in *E. coli*. *Biotechnology Bioengineering* 35, 732-738.

Meyer, H.-P., Leist, C., and Fiechter, A. (1984). Acetate formation in continuous culture of *Escherichia coli* K12 D1 on defined and complex media. *Journal of Biotechnology* 1, 355-358.

Milo, R., and Phillips, R. (2015). *Cell biology by the numbers*. (Garland Science).

Molenaar, D., Van Berlo, R., De Ridder, D., and Teusink, B. (2009). Shifts in growth strategies reflect tradeoffs in cellular economics. *Molecular Systems Biology* 5, 323.

Mori, M., Schink, S., Erickson, D.W., Gerland, U., and Hwa, T. (2017). Quantifying the benefit of a proteome reserve in fluctuating environments. *Nature Communications* 8, 1225.

Nanchen, A., Schicker, A., and Sauer, U. (2006). Nonlinear dependency of intracellular fluxes on growth rate in miniaturized continuous cultures of *Escherichia coli*. *Applied Environmental Microbiology* 72, 1164-1172.

Neidhardt, F.C. (1996). *Escherichia coli and Salmonella: cellular and molecular biology*. (Washington, DC: ASM Press).

Neidhardt, F.C., Ingraham, J.L., and Schaechter, M. (1990). *Physiology of the bacterial cell*. (Sinauer associates).

Nelson, D.L., Lehninger, A.L., and Cox, M.M. (2008). *Lehninger principles of biochemistry*. (Macmillan).

Niebel, B., Leupold, S., and Heinemann, M. (2019). An upper limit on Gibbs energy dissipation governs cellular metabolism. *Nature Metabolism* 1, 125-132.

Park, J.O., Rubin, S.A., Xu, Y.-F., Amador-Noguez, D., Fan, J., Shlomi, T., and Rabinowitz, J.D. (2016). Metabolite concentrations, fluxes and free energies imply efficient enzyme usage. *Nature Chemical Biology* 12, 482-489.

Sauer, U., Canonaco, F., Heri, S., Perrenoud, A., and Fischer, E. (2004). The soluble and membrane-bound transhydrogenases UdhA and PntAB have divergent functions in NADPH metabolism of *Escherichia coli*. *Journal of Biological Chemistry* 279, 6613-6619.

Scott, M., Gunderson, C.W., Mateescu, E.M., Zhang, Z., and Hwa, T. (2010). Interdependence of cell growth and gene expression: origins and consequences. *Science* 330, 1099-1102.

Shlomi, T., Benyamini, T., Gottlieb, E., Sharan, R., and Ruppin, E. (2011). Genome-scale metabolic modeling elucidates the role of proliferative adaptation in causing the Warburg effect. *PLoS Computational Biology* 7, e1002018.

Stevenson, K., McVey, A.F., Clark, I.B., Swain, P.S., and Pilizota, T. (2016). General calibration of microbial growth in microplate readers. *Scientific Reports* 6, 1-7.

Van Kampen, N.G. (1992). *Stochastic processes in physics and chemistry*. (Elsevier).

Vander Heiden, M.G., Cantley, L.C., and Thompson, C.B. (2009). Understanding the Warburg effect: the metabolic requirements of cell proliferation. *Science* 324, 1029-1033.

- Varma, A., and Palsson, B.O. (1994). Stoichiometric flux balance models quantitatively predict growth and metabolic by-product secretion in wild-type *Escherichia coli* W3110. *Applied Environmental Microbiology* *60*, 3724-3731.
- Vazquez, A., Liu, J., Zhou, Y., and Oltvai, Z.N. (2010). Catabolic efficiency of aerobic glycolysis: the Warburg effect revisited. *BMC Systems Biology* *4*, 1-9.
- Vazquez, A., and Oltvai, Z.N. (2016). Macromolecular crowding explains overflow metabolism in cells. *Scientific Reports* *6*, 31007.
- Wallden, M., Fange, D., Lundius, E.G., Baltekin, Ö., and Elf, J. (2016). The synchronization of replication and division cycles in individual *E. coli* cells. *Cell* *166*, 729-739.
- Wang, X., Xia, K., Yang, X., and Tang, C. (2019). Growth strategy of microbes on mixed carbon sources. *Nature Communications* *10*, 1279.